EFFECT OF Zn SUBSTITUTION ON STRUCTURAL AND MAGNETIC PROPERTIES OF NANOCRYSTALLINE $Li_{0.35-0.5x}Ni_{0.3}Zn_xFe_{2.35-0.5x}O_4$

A Dissertation Submitted to the Department Of Physics,

Bangladesh University of Engineering & Technology, Dhaka, in

Partial Fulfillment of the Requirement for the Degree of Master of Science (M. Sc.)
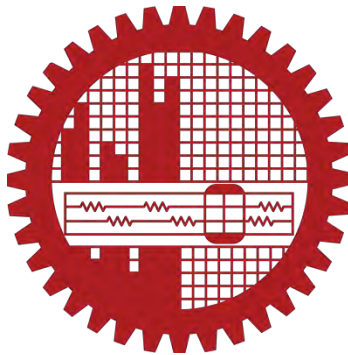
in Physics

SUBMITTED

By

MD. ARIF UL ISLAM

EXAMINATION ROLL NO.   **: 1014142516F**

SESSION   **: October 2014**

DEPARTMENT OF PHYSICS

BANGLADESH UNIVERSITY OF ENGINEERING & TECHNOLOGY

DHAKA 1000, BANGLADESH

BANGLADESH UNIVERSITY OF ENGINEERING & TECHNOLOGY
DEPARTMENT OF PHYSICS, DHAKA 1000, BANGLADESH
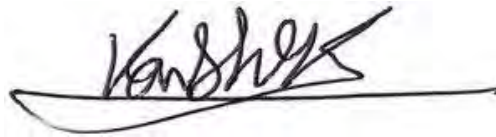
CERTIFICATION OF THESIS

The thesis titled "**EFFECT OF Zn SUBSTITUTION ON STRUCTURAL ANI MAGNETIC PROPERTIES OF NANOCRYSTALLINE** $Li_{0.35-0.5x}Ni_{0.3}Zn_xFe_{2.35-0.5x}O_4$ submitted by, **MD. ARIF UL ISLAM**, Roll No.: 1014142516F, Session: October 2014, ha: been accepted as satisfactory in partial fulfillment of the requirement for the degree of **Master o Science (M. Sc.) in Physics** on **25 June, 2016.**

BOARD OF EXAMINERS

1. (*A. Hossain .*   )
    Dr. A. K. M. Akther Hossain
    Professor, Department of Physics,
    BUET, Dhaka-1000, Bangladesh.

    Chairman
    (Supervisor)

2. (*F.Khanam.*   )
    Mrs. FahimaKhanam
    Head and Professor, Department of Physics,
    BUET, Dhaka-1000, Bangladesh.

    Member
    (Ex-Officio)

3. (   )
    Dr. Md. Feroz Alam Khan
    Professor, Department of Physics,
    BUET, Dhaka-1000, Bangladesh.

    Member

4. (   )
    Dr. Ishtiaque M. Syed
    Professor, Department of Physics,
    University of Dhaka, Dhaka-1000, Bangladesh.

    Member
    (External)

CANDIDATE'S DECLARATION

It is hereby declared that this thesis or any part of it has not been submitted elsewhere for the award of any degree or diploma.

_____

MD. ARIF UL ISLAM

DEDICATED TO
MY
PARENTS

ACKNOWLEDGEMENTS

ABSTRACT

Li-Ni-Zn ferrite nano-powders with nominal composition of $Li_{0.35-0.5x}Ni_{0.3}Zn_xFe_{2.35-0.5x}O_4$ (x = 0.00 - 0.40 in steps of 0.10) were synthesized by the chemical sol-gel auto combustion technique. Disk- and toroid-shaped samples prepared from each composition have been sintered at various temperatures (1100-1300°C) for 5h. The samples was characterized by X-ray diffraction (XRD), which has confirmed the formation of single phase spinel structure. The crystallite size of the as grown powder varied from 23 to 37 nm as measured using Scherrer formula. Surface morphology of the samples have been investigated using FESEM and elemental analysis of the compositions have been performed by EDX. The magnetic properties like complex initial permeability, loss factor, quality factor of these ferrites were measured from 100 Hz-120 MHz. The lattice parameters are calculated using the Nelson Riley function. Lattice constant increases with increase in Zn content, obeying vegard's law. It is observed that the density, are found to increase with increasing sintering temperature up to 1250°C, then decreases. On the other hand, porosity have opposite trend. Average grain sizes of the samples are determined from FESEM micrographs by linear intercept technique. The Zn substitution acts as an accelerator of grain growth and uniform grain distribution in these compositions. The real part of permeability and saturation magnetization increase with increasing Zn content for a fixed sintering temperature. The maximum value of $\mu_i^{/}$ (=254) is observed for $Li_{0.15}Ni_{0.3}Zn_{0.4}Fe_{2.15}O_4$ sintered at 1250°C which is more than 6 times compared to that of parent composition. The loss factor (at 10 kHz) for this composition is also reduced 6 times. As a result high quality factor is observed in these compositions. The complex initial permeability has been explained with the help of microstructure, and the re-distribution of cations in the tetrahedral and

octahedral sites. The weakening of exchange interaction may be confirmed by increasing the lattice parameter and decreasing Néel temperature (665 to 390°C) as the increase of Zn content. Substitution of Zn influences the magnetic properties due to modification of cation distribution.

CONTENTS

CHAPTER 1

INTRODUCTION

CHAPTER 2

LITERATURE REVIEW

CHAPTER 3

SAMPLE FABRICATION,CHARACTERIZATION

AND EXPERIMENTAL TECHNIQUES 57-76

CHAPTER 4

RESULTS AND DISCUSSION

CHAPTER 5

CONCLUSIONS

LIST OF FIGURES

Pages

Chapter 2

XIII

Chapter 3

Chapter 4

LIST OF TABLES

LIST OF SYMBOLS AND ABBREVIATIONS

AC	Alternating current
B	Magnetic induction
CMR	Colossal magnetoresistance
$F(\theta)$	Nelson-Riley function
f_r	Resonance frequency
g	Landé splitting factor
H_{cr}	Critical field
J	Exchange integral
K	Total anisotropy
K_1	Magnetocrystalline anisotropy constant
L_s	Self-inductance of the sample core
L_o	Inductance of the winding coil without sample
M	Magnetization
M_s	Saturation magnetization
N_A	Avogadro's number
P	Porosity
P_{intra}	Intragranular porosity
P_{inter}	Intergranular porosity
P_e	Eddy-current loss
Q	Relative quality factor
T_C	Curie temperature
T_N	Néel temperature
T_S	Sintering temperature
$tan\delta$	Loss factor
Z	Complex impedance
α	Restoring force coefficient
β	Viscous damping factor
γ	Domain wall energy
ω	Angular velocity
δ_w	Domain wall thickness
μ_i	Initial permeability
μ'	Real part of complex permeability
μ''	Imaginary part of complex permeability
μ_B	Bohr magneton
χ_{spin}	Intrinsic rotational susceptibility
χ_w	Domain wall susceptibility
ρ_{th}	Theoretical density
ρ_B	Bulk density

CHAPTER 1

INTRODUCTION

1.1 Background of the study

Ferrites are magnetic ceramics containing iron oxide as a major constituent in it. It is now some 70 years since ferrites debuted as an important new category of magnetc materials. These are now very well established group of magnetic materials. Today ferrites are employed in a truly wide rang of applications, and have contributed materially to the advances in electronics. In the area of new materials, ferrites with permeabilities up to 30,000 and power ferrites for frequencies up to 10 MHz have been made available commercially [1]. In the recent times, there has been a revolution in the development of magnetic ceramics. Among the various magnetic materials, ferrites are a large class of technologically important ceramic oxides with remarkable magnetic and electrical properties. According to their crystal structure spinel type ferrites are natural super lattice and they have tetrahedral A site and octahedral B site in AB_2O_4 crystal structure. Various cations can be placed in A site and B site to tune their magnetic properties and depending on A site and B site cations they can exhibit ferrimagnetic, antiferromagnetic, spin (cluster) glass and paramagnetic behaviors [2, 3]. Although spinel ferrites have been widely used in many electronic devices for more than fifty years, much research and development in this field is still going on, from basic as well as application point of view. Due to their remarkable electrical and magnetic properties, these materials are subjects of intense theoretical and experimental investigation for technological application [4, 5]. Spinel ferrites show better properties by virtue of their unique electronic and crystalline structure which may be used for various applications such as recording heads, inductors, transformers, antennas and power transformer [6-9].

But for high performance, permeability and resistivity of these materials need to be increased. Most other technologically useful magnetic materials such as iron and soft magnetic alloys have low electrical resistivity. This makes them difficult for applications at high frequencies. The low electrical resistivity of these materials allows eddy currents to flow within the materials themselves, thereby producing heat and waste energy [10, 11].

 Range of soft ferrites components:

(i) TV line output transformer;

(ii) Wide band transformer core;

(iii) High Q filter core;

(iv) Precision ferrite antenna for transponder;

Range of hard ferrite components:

(a) Wind screen wiper motor;

(b) Loudspeaker and field magnetsm;

(c) Hard ferrite-polymer composition.

In this thrust area of research on magnetic fine particles, lithium ferrite forms a very important group of materials. Lithium ferrite and mixed lithium ferrites have very high potential for microwave applications, especially as replacements for garnets, due to their low cost. The squareness of the hysteresis loop and superior temperature performance are other prominent advantages that have made them very promising candidates for application in microwave devices [12-14]. Effect of various substitutions in lithium ferrite exhibits very good relaxation and anisotropy properties than other type of ferrites [15, 16].

Studies on substituted *Li-Mg-Fe* spinels show that it can be useful in microwave applications having improved magnetic properties [17, 18]. Various researchers have reported the study of *Ni* substitution which seems to enhance the magnetic properties as well [19, 20]. Besides studying on pure Lithium ferrite [12-14], *Li-Mg* and *Li-Ni* ferrite, many researchers have studied Li-Co [21], Li-Mn [22], Li-Ni [23], Li-Mg-Ni [24, 25] ferrites. To the best of our knowledge, no literature is available on Zn substituted $Li_{0.35-0.5x}Ni_{0.3}Zn_xFe_{2.35-0.5x}O_4$. Therefore, in this proposed research, Zn substituted $Li_{0.35-0.5x}Ni_{0.3}Zn_xFe_{2.35-0.5x}O_4$ will be prepared by sol gel auto combustion technique and the structural and magnetic properties will be investigated.

1.2 Motivation and objectives

➢ Motivation

The choice of composition of soft a ferrite is made to get one or more of following properties:

- Maximum permeability;

- Minimum energy losses;

- Temperature variation of properties between prescribed limits;

- High saturation magnetization;

- Minimum cost;

➢ Objectives

Ferrites are especially convenient for high frequency uses because of their high resistivity. The high frequency response of the complex permeability is therefore very useful in determining the convenient frequency range in which a particular ferrite material can be used. The mechanism of eddy current losses and damping of domain wall

motion can be understood from the relative magnitudes of the real and imaginary part of the complex permeability. The effect of composition and microstructure on the frequency response is therefore very useful.

The main objectives of the present research are as follows:

- Preparation of various nanocrystalline $Li_{0.35-0.5x}Ni_{0.3}Zn_xFe_{2.35-0.5x}O_4$ (for x = 0.00 to 0.40 in steps of 0.10) compositions.

- Perform structural characterizations, density and porosity of the samples.

- Investigation of surface morphology, microstructure and compositional analyses using Field Emission Scanning Electron Microscopy (FESEM) and Energy Dispersive X-ray (EDX) spectroscopy.

- Determination of Néel temperature (T_N) from measurement of temperature dependent initial permeability.

- Complex initial permeability as a function of frequency (100 Hz-120 MHz).

- Measurement of magnetization as a function of field, *M-H*, at room temperature.

1.3 Outline of the thesis

The summary of the thesis is as follows:

Chapter 1 of this thesis deals with the importance of ferrites and objectives of the present work.

Chapter 2 gives a brief overview of the materials, theoretical background as well as crystal structure of the spinel type ferrites.

Chapter 3 gives the details of the sample preparation and description of different measurement techniques that have been used in this research work.

Chapter 4 is devoted to the results of various investigations of the study and explanation of results in the light of existing theories.

The conclusions drawn from the overall experimental results and discussion are presented in **Chapter 5**.

References:

[1]   Goldman, A., *Modern ferrite technology*, Van Nostrand Reinhold, New York, 1990.

[2]   Mahmud, S. T., Hossain, A. K. M. Akther, Hakim, A. K. M. Abdul, Seki, M., Kawai, T. and Tabata, H., "Influence of microstructure on the complex permeability of spinel type Ni-Zn ferrite", *J. Magn. Magn. Mater.*, Vol - 305, No. 1, pp. 269-274, 2006.

[3]   Hossain, A. K. M. Akther., Seki, M., Kawai, T. and Tabata, H., "Colossal magnetoresis in spinel type $Zn_{1-x}Ni_xFe_2O_4$", *J. Appl. Phys.*, Vol. 96, No. 1, pp. 1273, 2004.

[4]   Ahmed, M. A., Okasha, N. and Salah, L., "Influence of yttrium ions on the magnetic properties of Ni-Zn ferrites", *J. Magn. Magn. Mater.,* Vol. 264, pp. 241-250, 2003.

[5]   Verma, A., Goel, T. C., Mendiratta, R. G. and Kishan, P., "Magnetic properties of nickel-zinc ferrites prepared by the citrate precursor method", *J. Magn. Magn. Mater.*, Vol. 208, pp. 13-19, 2000.

[6]   Valenzuela, R., *Magnetic Ceramics*, Cambridge University Press, Cambridge, 1994.

[7]   Schiessl, W., Potzel, W., Karzel, H., Steiner, M. and Kalvius, G. M., "Magnetic properties of the $ZnFe_2O_4$ spinel", *Phys. Rev. B*, Vol. 53, No. 14, pp. 9143-9152, 1996.

[8]   Hossain, A. K. M. Akther, Tabata, H. and Kawai, T., "Magnetoresistive properties of $Zn_{1-x}Co_xFe_2O_4$ ferrites", *J. Magn. Magn. Mater.*, Vol. 320, pp. 1157, 2008.

[9]   Sousa, M. H., Tourinho, F. A., Depeyrot, J., Da silva, G. J. and Lara, M. C. F., "New Electric Double-Layered Magnetic Fluids Based on Copper, Nickel, and Zinc Ferrite Nanostructures", *J. Phys. Chem.,* Vol. 105, pp. 1169, 2001.

[10]   Chukalkin, Yu. G. and Teplykh, A. E., "Magnetic state of nickel-zinc ferrites at high zinc concentrations", *Phys. Solid State*, Vol. 40, No. 8, pp. 1364-1365, 1998.

[11]   Ahmed, M. A., Okasha, N. and Salah, L., "Influence of yttrium ions on the magnetic properties of Ni-Zn ferrites", *J. Magn. Magn. Mater.*, Vol. 264, pp. 241-250, 2003.

[12]   Argentina, G. M., and Baba, P. D., "Microwave Lithium Ferrites: An Overview", *IEEE T MICROW THEORY*, Vol. MTT-22, No. 6, pp. 652-658, 1974.

[13]   White, G. O. and Patton, C.E., "Magnetic Properties of Lithium Ferrite Microwave Materials", *J. Magn. Magn. Mater.*, Vol. 9, pp. 299, 1978.

[14]   Andreev, N. M. and Kojoukharoff, V. I., "On some magnetic characteristics of a system of lithium ferrites for microwave applications", *J. Magn. Magn. Mater.*, Vol. 54-57, No 3, pp. 1605-1606, February 1986.

[15]   Patton, C. E., Blankenbeckler, D. L., Brower, C. J., Dalton, B. B. and Lucero, A. M., "Microwave Relaxation Properties of Substituted Lithium Ferrite", *IEEE Trans. Magn.*, Vol. 17, Issue 6, pp. 2976-2978, 1981.

[16]   Brower, C. J. and Patton, C. E, "Determination of Anisotropy Field in Polycrystalline Lithium Ferrites from FMR linewidths", *J. Appl. Phys.*, Vol. 53, pp. 2104-2106, 1982.

[17]   Kishan, P., Kumar, N., Prakash, C. and Zaidi, Z. H., "Studies on substituted *Li-Mg-Fe* spinels for microwave applications", *Ferroelectrics Letters Section*, Vol. 18, Issue 3 & 4, pp. 91-97, 1994.

[18]   Widatallah, H. M., Johnson, C., Gismelseed, A. M., Al- Omari, I. A., Stewart, S. J., Al- Harthi, S. H., Thomas, S. and Sitepu. H., "Structural and magnetic studies of nanocrystalline Mg-doped $Li_{0.5}Fe_{2.5}O_4$ particles prepared by mechanical milling", *J. Phys. D: Appl. Phys.*, Vol. 41, pp. (165006)1-(165006) 10, 2008.

[19]   Bhatu, S. S., Lakhani, V. K., Tanna, A. R., Vasoya, N. H., Buch, J. U., Sharma, P.U., Trivedi, U. N., Joshi, H. H. and Modi, K. B., "Effect of nickel substitution on structural, infrared and elastic properties of lithium ferrite", *Indian J. Pure & Appl. Phys.*, Vol. 45, pp. 597-608, 2007.

[20]   Maghsoudi, I., Shokrollahi, H., Hadianfard, M. J. and Amighian, J., "Synthesis and characterization of $Ni_1Al_xFe_{2-x}O_4$ magnetic spinel ferrites produced by conventional method", *Powder Tech.*, Vol. 235, pp. 110-114, 2013.

[21]   Watawe, S. C., Sarwade, B. D., Bellad, S. S., Sutar, B. D. and Chaugule, B. K., "Microstructure and magnetic properties of Li-Co ferrites", *Mater. Chem. Phys.*, Vol. 65(2), pp. 173-177, 2000.

[22]   Ramesh, B. and Ravinder, D., "Electrical properties of Li–Mn ferrites", *Mater. Lett.*, Vol. 62, pp. 2043-2046, 2008.

[23]   Trivedi, U. N., Jani, K. H., Modi, K. B. and Joshi, H. H., "Study of cation distribution in lithium doped nickel ferrite", *J. Mater. Sci. Lett.*, Vol. 19, No. 14, pp. 1271-1273, 2000.

[24]   Hossain, A. K. M. Akther, Rahman, M. A., Farhad, S. F. U., Vilquin, B. and Tanaka, Hidekazu, "Effect of Li substitution on the magnetic properties of $Li_xMg_{0.40}Ni_{0.60-2x}Fe_{2+x}O_4$ ferrites", *Physica B*, Vol. 406, pp. 1506-1512, 2011.

[25]   Hossain, A. K. M. Akther, Chowdhury, M. M. A., Vilquin, B. and Takana, Hidekazu, "Influence of Li substitution on structural and magnetic properties of $Li_xNi_{0.2}Mg_{0.8-2x}Fe_{2+x}O_4$", *Mater. Chem. Phys.*, Vol. 133, pp. 941-945, 2012.

CHAPTER 2

LITERATURE REVIEW

2.1 Overview of the materials

Ferrites are electrically non-conductive ferrimagnetic ceramic compound materials which commonly expressed by the general chemical formula $MeO.Fe_2O_3$, where Me represents divalent metals. The study of ferrites is going on over hundred years. For the first times, S. Hilpert (1909) focused on the usefulness of ferrites at high frequency [1]. A systematic investigation was launched by Snoek (1936) at Philips Research Laboratory [2]. At the same time Takai (1937) in Japan was seriously engaged in the research work on the same materials [1]. Snoek's extensive works on ferrites unveiled many mysteries regarding magnetic properties of ferrites. He was particularly looking for high permeability materials of cubic structure. This particular structure for symmetry reasons supports low crystalline anisotropy. He found suitable materials in the form of mixed spinels of the type $MeZnFe_2O_4$, where Me stands for metals like Cu, Mg, Ni, Co or Mn, for which permeability was found to be up to 4000 [1-3]. Here after starts the story of Li-ferrites. Lithium ferrites became commercially important as computer memory core materials in the early 1960˝s. The high Curie temperature, leading to unparalleled thermal stability, the excellent hysteresis loop properties, and the high saturation magnetization all prompted this commercial interest. For many of the same reasons there was considerable development effort aimed at providing micro-wave quality lithium ferrites [4-7]. The principal interest in microwave lithium ferrites is a low-cost replacement for the rare earth-iron garnets, offering competitive or improved temperature performance. Lithium ferrites with magnetizations comparable to the garnets are very refractory due to the high concentration and nature of the substituent

elements, which requires relatively high sintering temperatures. This type of heat treatment causes the volatility of Li_2O [8, 9] which results in some reduction of iron. For this reason lithium ferrites were considered difficult to prepare with low dielectric loss. In addition, these lower magnetization lithium ferrites were characterized by high porosities, and as a result, high coercive forces and broad resonance line-widths were experienced [10].

The structural and elastic properties of *Li-Ni* ferrite was studied by Bhatu *et al.* [11]. The observed increase in magnitude of elastic constants, elastic wave velocities and infrared spectral analysis is found easier, valid and suitable for spinel ferrite. Akhter *et al.* [12] investigated high curie temperature which decreases with increase in Cd content. They reported that the decrease in curie temperature may be due to the decrease in A-B interaction. They also reported the confirmation of the single phase cubic structure. Magnetic studies of cobalt substituted lithium zinc ferrites were also studied by I. Soibam. Magnetization measurement indicated that cobalt shows anomalous behavior when substituted in lithium ferrites in the presence of *Zn* [13].

The structure and magnetic properties of spinel-related *Mg*-doped $Li_{0.5}Fe_{2.5}O_4$ nano-crystalline particles prepared by milling a pristine sample, $Li_{0.41}Fe_{2.41}Mg_{0.17}O_4$ for different times were investigated by Widatallah *et al* [14]. The saturation magnetization and Curie temperature were found to decrease and the material increasingly turned super-paramagnetic as milling proceeded. The coercivity and the magnetization increased initially and later decreased at higher milling times. The sintering process is considered to be one of the most vital steps in ferrite preparation and often plays a dominant role in many magnetic properties. Tasaki *et al.* [15] studied the effect of sintering atmosphere on permeability of sintered ferrite. They found that high density is

one of the factors, which contribute to greater permeability. However, permeability decreased in an atmosphere without O_2 at high sintering temperature where high density was expected. This decrease in permeability is attributed to the variation of chemical composition caused by volatilization of Zn. At low sintering temperature a high permeability is obtained in an atmosphere without O_2 because densification and stoichiometry plays a principal role in increasing permeability. At high sintering temperature the highest permeability is obtained in the presence of O_2 because the effect of decrease of Zn content can then be neglected.

Studying the electromagnetic properties of ferrites, Nakamura [16] suggested that both the sintering density and the average grain size increased with sintering temperature. These changes were responsible for variations in magnetization, initial permeability and electrical resistivity.

High permeability attainment is certainly affected by the microstructure of the ferrites. Roess showed that [17] the very high permeability is restricted to certain temperature ranges and the shapes of permeability versus temperature curves are strongly affected by any inhomogeneity in the ferrite structure. Leung *et al.* [18] performed a Low-temperature Mössbauer study of a nickel-zinc ferrite: $Zn_{1-x}Ni_xFe_2O_4$. They found that for $x \leq 0.5$ the resultant *A-* and *B-* site *Fe*-spin moments have a collinear arrangement, whereas for $x > 0.5$ a non-collinear arrangement of *A-* and *B*-site *Fe*-spin moments exist. An explanation based on the relative strength of the exchange constant J_{AB} and J_{BB} is given to account for this difference. Rezlescu *et al.* [19] reported that the sintering behaviour and microstructure of the ferrites samples largely affected by *PbO* addition. *PbO* significantly reduced the sintering temperatures, thus energy consumption is minimized and material loss by evaporation is minimized [20].

There are two mechanisms in the phenomenon of permeability; spin rotation in the magnetic domains and wall displacements. The uncertainty of contribution from each of the mechanisms makes the interpretation of the experimental results difficult. Globus [21] shows that the intrinsic rotational permeability μ_r and 180^0 wall permeability μ_w may be written as: $\mu_r = 1 + \dfrac{2\pi M_s^2}{K}$ and $\mu_w = 1 + \dfrac{3\pi M_s^2 D}{4\gamma}$, where M_s is the saturation magnetization, K is the total anisotropy, D is the grain diameter and $\gamma \equiv K\delta_w$ is the wall energy.

El-Shabasy [22] studied the DC electrical resistivity of $Zn_xNi_{1-x}Fe_2O_4$ ferrites. He shows that the ferrite samples have semiconductor behaviour where DC electrical resistivity decreases on increasing the temperature. $\rho(T)$ for all samples follows $\rho(T) = \rho_0 \exp(E/k_BT)$, where E is the activation energy for electric conduction and ρ_0 is the pre-exponential constant or resistivity at infinitely high temperature. The DC resistivity, $\rho(T)$, decreases as the Zn ion substitution increases. It is reported that Zn ions prefer the occupation of tetrahedral (A) sites; Ni ions prefer the occupation of octahedral (B) sites while Fe ions partially occupy the A and B sites. On increasing Zn substitution (at A sites), the Ni ion concentration (at B sites) will decrease. This lead to the migration of some Fe ions from A sites to B sites to substitute the reduction in Ni ion concentration at B sites. As a result, the number of ferrous and ferric ions at B sites (which is responsible for electric conduction in ferrites) increases. Consequently ρ decreases on Zn substitution. Another reason for the decrease in ρ on increasing Zn ion substitution is that, zinc is less resistive ($\rho = 5.92 \ \mu\Omega cm$) than nickel ($\rho = 6.99 \ \mu\Omega cm$). The main conductivity mechanism in ferrites is attributed to electron hopping between Fe^{3+} and Fe^{2+} in octahedral sites. Resistivity in spinels is very

sensitive to stoichiometry; a small variation of Fe content in $Zn_{0.7}Ni_{0.3}Fe_{2+x}O_{4-y}$ results in resistivity variations of $\sim 10^7$. Excess Fe can easily dissolve in spinel phase by a partial reduction of Fe from $3Fe_2^{3+}O_3$ to $2Fe^{2+}Fe_2^{3+}O_4$ (and $1/2O_2 \uparrow$) [2].

2.2 Magnetic ordering

The onset of magnetic order in solids has two basic requirements:

(i) Individual atoms should have magnetic moments (spins),

(ii) Exchange interactions should exist that couple them together.

Magnetic moments originate in solids as a consequence of overlapping of the electronic wave function with those of neighbouring atoms. This condition is best fulfilled by some transition metals and rare-earths. The exchange interactions depend sensitively upon the inter-atomic distance and the nature of the chemical bonds, particularly of nearest neighbour atoms. When the positive exchange dominates, which corresponds to parallel coupling of neighbouring atomic moments (spins), the magnetic system becomes ferromagnetic below a certain temperature T_C called the Curie temperature. The common spin directions are determined by the minimum of magneto-crystalline anisotropy energy of the crystal. Therefore, ferromagnetic substances are characterized by spontaneous magnetization. But a ferromagnetic material in the demagnetized state displays no net magnetization in zero field because in the demagnetized state a ferromagnetic of macroscopic size is divided into a number of small regions called domains, spontaneously magnetized to saturation value and the directions of these spontaneous magnetization of the various domains are such that the net magnetization of the specimen is zero. The existence of domains is a consequence of energy minimization. The size and formation of these domains is in a complicated manner

dependent on the shape of the specimen as well as its magnetic and thermal history. When negative exchange dominates, adjacent atomic moments (spins) align antiparallel to each other, and the substance is said to be anti-ferromagnetic below a characteristic temperature, T_N, called the Néel temperature. In the simplest case, the lattice of an anti-ferromagnet is divided into two sub-lattices with the magnetic moments of these in anti-parallel alignment. This result is zero net magnetization. A special case of anti-ferromagnetism is ferrimagnetism. In ferrimagnetism, there are also two sub-lattices with magnetic moments in opposite directions, but the magnetization of the sub-lattices are of unequal strength resulting in a non-zero magnetization and therefore has net spontaneous magnetization. At the macroscopic level of domain structures, ferromagnetic and ferrimagnetic materials are therefore similar.
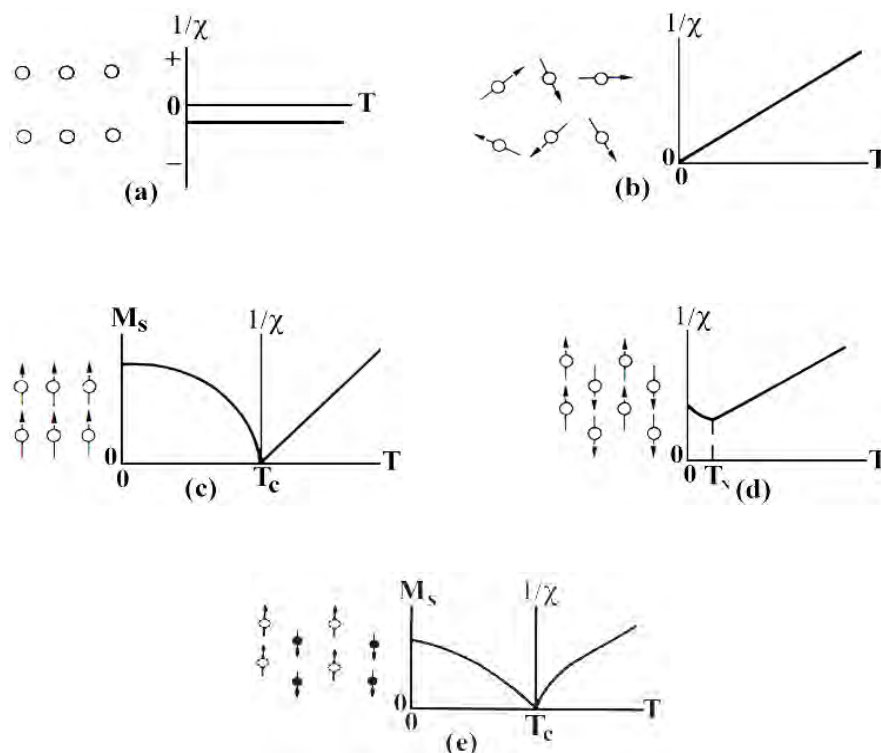
Fig. 2.1 Temperature dependence of the inverse susceptibility for: (a) a diamagnetic material; (b) a paramagnetic material, showing Curie's law behaviour; (c) a ferromagnetic material, showing a spontaneous magnetization for $T<T_C$ and Curie-Weiss behaviour for $T>T_C$; (d) an antiferromagnetic

material; (e) a ferrimagnetic material, showing a net spontaneous magnetization for $T<T_C$ and non linear behaviour for $T>T_C$.

The Curie and Néel temperatures characterize a phase transition between the magnetically ordered and disordered (paramagnetic) states. From these simple cases of magnetic ordering various types of magnetic order exists, particularly in metallic substances. Because of long-range order and oscillatory nature of the exchange interaction, mediated by the conduction electrons, structures like helical, conical and modulated patterns might occur. A useful property for characterizing the magnetic materials is the magnetic susceptibility (χ), defined as the magnetization, M, divided by the applied magnetic field, H i.e. $\chi = \dfrac{M}{H}$. The temperature dependence of susceptibility or, more accurately, inverse of susceptibility is a good characterization parameter for magnetic materials, Fig. 2.1. Fig. 2.1(e) shows that in the paramagnetic region, the variation of the inverse susceptibility with temperature of a ferrite material is decidedly non-linear. Thus the ferrite materials do not obey the Curie-Weiss law, $\chi = \dfrac{C}{(T - T_C)}$ [2, 27].

2.3 Crystal structure of spinel ferrites

2.3.1 Ionic charge balance and crystal structure of cubic spinel ferrite

The spinel lattice is composed of a close-packed oxygen arrangement in which 32 oxygen ions form a unit cell that is the smallest repeating unit in the crystal network. Between the layers of oxygen ions, if we simply visualize them as spheres, there are interstices that may accommodate the metal ions. Now, the interstices are not all the same; some which are called A sites are surrounded by or coordinated with 4 nearest

neighbouring oxygen ions whose lines connecting their centers form a tetrahedron. Thus, A sites are called tetrahedral sites (Fig. 2.2 (a)). The other type of site (B sites) is coordinated by 6 nearest neighbor oxygen ions whose center connecting lines describe an octahedron. The B sites are called octahedral sites (Fig. 2.2(b)). In the unit cell of 32 oxygen ions, there are 64 tetrahedral sites and 32 octahedral sites. If all of these were filled with metal ions, of either $+2$ or $+3$ valence, the positive charge would be very much greater than the negative charge and so the structure would not be electrically neutral. It turns out that of the 64 tetrahedral sites, only 8 are occupied and out of 32 octahedral sites, only 16 are occupied. If, as in the mineral, spinel, the tetrahedral sites are occupied by divalent ions and the octahedral sites are occupied by the trivalent ions, the total positive charge would be 8× (+2) = +16 plus the 16x (+3) =+48 or a total of +64 which is needed to balance the 32× (-2) = -64 for the oxygen ions. There would then be eight formula units of $MO.Fe_2O_3$ or MFe_2O_4 in a unit cell. A spinel unit cell contains two types of sub-cells. The two types of sub-cells alternate in a three-dimensional array so that each fully repeating unit cell requires eight sub-cells.

The crystallographic environments of the A and B sites are distinctly different. The unit cell contains so many ions that a two-dimensional drawing of the complete cell would not be very informative. Instead we can consider a unit cell of edge a, to be divided into eight octants, each of edge $a/2$, as shown in Fig. 2.2(c). The four shaded octants have identical contents, and so do the four unshaded octants. The contents of the two lower-left octants in Fig. 2.2(c) are shown in Fig. 2.2(d). One tetrahedral site occurs at the center of the right octant of Fig. 2.2(d), and other tetrahedral sites are at some but not all octant corners. Four octahedral sites occur in the left octant; one is connected by dashed lines to six oxygen ions, two of which, shown dotted, are in adjacent octants

15

behind and below. The oxygen ions are arranged in the same way, in tetrahedra, in all octants. Not all of the available sites are actually occupied by metal ions. Only one-eighth of the *A* sites and one-half of the *B* sites are occupied, as shown in Table 2.1 [2]. In the mineral spinel, $MgO.Al_2O_3$, the Mg^{2+} ions are in *A* sites and the Al^{3+} ions are in *B* sites.

Some ferrites $MO.Fe_2O_3$ have exactly this structure, with M^{2+} in *A* sites and Fe^{3+} in *B* sites. This is called the normal spinel structure. If 8 divalent (*M*) ions occupy the *A*-site i.e., tetrahedral site and 16 tetravalent ions (Fe^{3+}) occupy the *B*-site i.e., octahedral site, the structure is said to be Normal spinel.

If *B*-site i.e., octahedral site is occupied half by divalent metal ion and half by trivalent iron ions, generally distributed in random and *A*-site i.e., tetrahedral site by trivalent iron ions, the structure is said to be Inverse spinel. Both zinc and cadmium ferrite have this structure and they are both nonmagnetic, i.e., paramagnetic. Many other ferrites, however, have the inverse spinel structure, in which the divalent ions are on *B* sites, and the trivalent ions are equally divided between *A* and B sites. The divalent and trivalent ions normally occupy the B sites in a random fashion, i.e., they are disordered. Iron, cobalt, and nickel ferrites have the inverse structure, and they are all ferrimagnetic.

The normal and inverse structures are to be regarded as extreme cases, because X-ray and neutron diffraction show that intermediate structures can exist. Thus manganese ferrite is almost, but not perfectly, normal; instead of all the Mn^{2+} ions being on *A* sites, a fraction 0.8 is on A sites and 0.2 on B sites. Similarly, magnesium ferrite is not quite inverse; a fraction 0.9 of the Mg^{2+} ions is on B sites and 0.1 on A sites. The distribution of the divalent ions on A and B sites in some ferrites can be altered by heat

treatment; it may depend, for example, on whether the material is quenched from a high

temperature or slowly cooled.

(a) Tetrahedral *A* site   (b) Octahedral *B* site

● Metal ion in
   tetrahedral site

○ Metal ion in
   octahedral site

◯ Oxygen ion

(c)

(d)
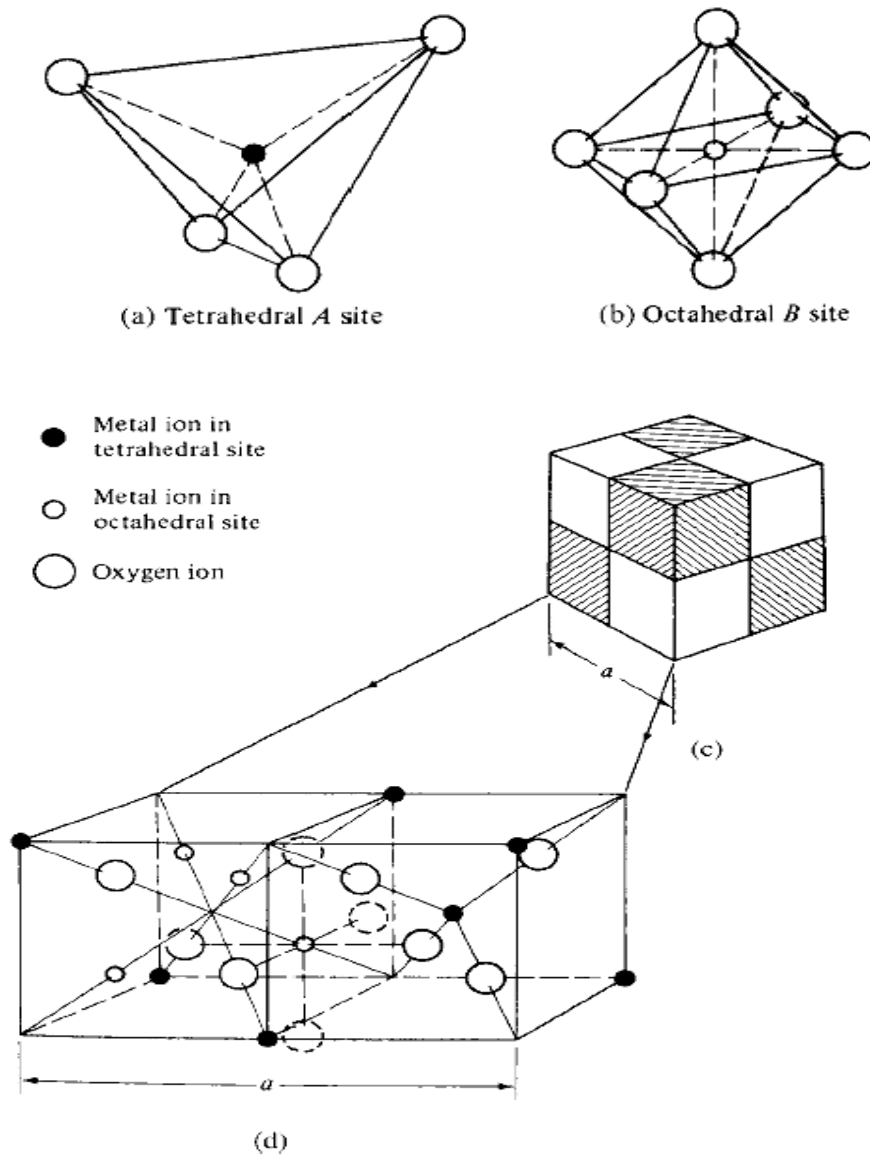
Fig.2.2 Crystal structure of a cubic ferrite [27].

Table 2.1 Arrangements of metal ions in the unit cell of a ferrite $MO.Fe_2O_3$ [27].

Kind of Site	Number Available	Number Occupied	Occupants	
			Normal Spinel	Inverse Spinel
Tetrahedral (A)	64	8	$8M^{2+}$	$8\ Fe^{3+}$
Octahedral (B)	32	16	$16\ Fe^{3+}$	$8\ Fe^{3+}$ $8\ M^{2+}$

The positions of the ions in the spinel lattice are not perfectly regular (as the packing of hard spheres) and some distortion does occur. The tetrahedral sites are often too small for the metal ions so that the oxygen ions move slightly to accommodate them. The oxygen ions connected with the octahedral sites move in such a way as to shrink the size the octahedral cell by the same amount as the tetrahedral site expands. The movement of the tetrahedral oxygen is reflected in a quantity called the oxygen parameter, which is the distance between the oxygen ion and the face of the cube edge along the cube diagonal of the spinel sub-cell. This distance is theoretically equal to $3/8a_o$ where a_o is the lattice constant [1].

2.3.2 Site Preferences of the ions

The preference of the individual ions for the two types of lattice sites is determined by;

1. The ionic radii of the specific ions

2. The size of the interstices

3. Temperature

4. The orbital preference for specific coordination

The most important consideration would appear to be the relative size of the ion compared to the size of the lattice site. The divalent ions are generally larger than the trivalent (because the larger charge produces greater electrostatic attraction and so pulls the outer orbits inward). The octahedral sites are also larger than the tetrahedral [28]. Therefore, it is reasonable that the trivalent ions such as Fe^{3+} would go into the tetrahedral sites and the divalent ions would go into the octahedral. Two exceptions are found in Zn^{2+} and Cd^{2+} which prefer tetrahedral sites because the electronic configuration is favorable for tetrahedral bonding to the oxygen ions. Thus Zn takes preference for tetrahedral sites over the Fe^{3+} ions. Zn^{2+} and Co^{2+} have the same ionic radius but Zn prefers tetrahedral sites and Co^{2+} prefers octahedral sites because of the configurationally exception. Ni^{2+} and Cr^{3+} have strong preferences for octahedral sites, while other ions have weaker preferences [28].

2.3.3 Unit cell dimensions

The dimensions of the unit cell are given in Angstrom Units which are equivalent to 10^{-8} cm. If we assume that the ions are perfect spheres and we pack them into a unit cell of measured (X-ray diffraction) dimensions we find certain discrepancies that show that the packing is not ideal. The positions of the ions in the spinel lattice are not perfectly regular (as the packing of hard spheres) and some distortion does occur. The tetrahedral sites are often too small for the metal ions so that the oxygen ions move slightly to accommodate them. The oxygen ions connected with the octahedral sites move in such a way as to shrink the size of the octahedral cell by the same amount as the tetrahedral site expands .The movement of the tetrahedral oxygen is reflected in a quantity called the oxygen parameter which is the distance between the oxygen ion and

the face of the cube edge along the cube diagonal of the spinel sub-cell. This distance is theoretically equal to $3/8a_o$. The unit cell length of *Li*-Ferrite, *Ni* ferrite and *Zn* Ferrite are observed to be 8.33 Å, 8.34 Å and 8.44 Å respectively [2].

2.4 Cation distribution of spinel ferrites

In spinel structure the distribution of cations over the tetrahedral or *A* sites and octahedral or *B* sites can be present in a variety of ways. If all the Me^{2+} ions in $Me^{2+}Me_2^{3+}O_4$ are in tetrahedral and all Me^{3+} ions in octahedral positions, the spinel is then called normal spinel. Another cation distribution in spinel exists, where one half of the cations Me^{3+} are in the *A* positions and the rest, together with the Me^{2+} ions are randomly distributed among the *B* positions. The spinel having the latter kind of cation distribution is known as inverse spinel. The distribution of these spinels can be summarized as [2, 25-26]

1) Normal spinels, i.e. the divalent metal ions are on *A*-sites: $Me^{2+}[Me_2^{3+}]O_4$,

2) Inverse spinels, i.e. the divalent metal ions are on *B*-sites: $Me^{3+}[Me^{2+}Me_2^{3+}]O_4$.

A completely normal or inverse spinel represents the extreme cases. There are many spinel oxides which have cation distributions intermediate between these two extreme cases and are called mixed spinels.

The general cation distribution for the spinel can be indicated as:

$$(Me_x^{2+}Me_{1-x}^{3+})[Me_{1-x}^{2+}Me_{1+x}^{3+}]O_4$$
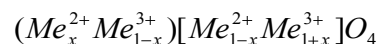
where the first and third brackets represent the A and B sites respectively. For normal spinel $x = 1$, for inverse spinel $x = 0$. The quantity x is a measure of the degree of inversion. In the case of some spinel oxides x depends upon the method of preparation.

The cation distributions of *Li*-Ferrite, *Ni*-Ferrite and *Ni-Zn* Ferrite are shown below:

Li Ferrite: $(Fe^{3+}) [Li_{0.5}^{1+} Fe_{1.5}^{3+}] O_4$ [2, 10]

Ni Ferrite: $(Fe^{3+}) [Ni^{2+} Fe^{3+}] O_4$ [2, 42]

Ni-Zn Ferrite: $(Zn_x^{2+} Fe_{1-x}^{3+}) [Ni_{1-x}^{2+} Fe_{1+x}^{3+}] O_4$ [2, 43]
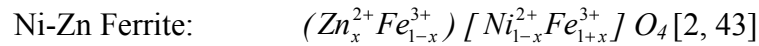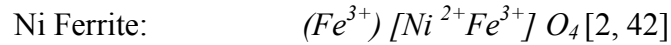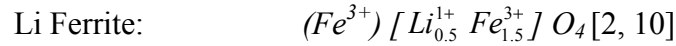
where x is the degree of inversion.

Both Li ferrite and Ni-Ferrite is an inverse spinel and Ni-Zn Ferrite is a mixed ferrite.

The cation distribution of various $Li_{0.35-0.5x}Ni_{0.3}Zn_xFe_{2.35-0.5x}O_4$ ferrite assumed as

$$(Zn_x^{2+}Fe_{1-x}^{3+})[Li_{0.35-0.5x}^{1+}Ni_{0.3}^{2+}Fe_{1.35+0.5x}^{3+}]O_4^{2-}$$ [31]
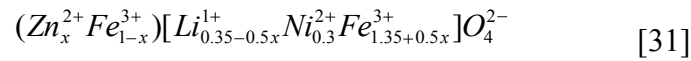
The basic magnetic properties of the ferrites are very sensitive functions of their cation distributions. Mixed ferrites having interesting and useful magnetic properties are prepared by mixing two or more different types of metal ions

Spinel oxides are ionic compounds and hence the chemical bonding occurring in them can be taken as purely ionic to a good approximation. The total energy involved, however, consists of the Coulomb energy, the Bohr repulsive energy, the polarization and the magnetic interaction energy. The energy terms are all dependent on lattice constant, oxygen position parameter and the ionic distribution. In principle the equilibrium cation distribution can be calculated by minimizing the total energy with respect to these variables. But the only energy that can be written with any accuracy is the Coulomb energy. The individual preference of some ions for certain sites resulting from their electronic configuration also play an important role. The divalent ions are generally larger than the trivalent (because the larger charge produces greater electrostatic attraction and so pulls the outer orbits inward). The octahedral sites are also

larger than the tetrahedral. Therefore, it would be reasonable that the trivalent ions Fe^{3+} (0.67Å) would go into the tetrahedral sites and the divalent ions Fe^{2+} (0.83Å) go into the octahedral. Two exceptions are found in Zn^{2+} (0.82) and Cd^{2+} which prefer tetrahedral sites because the electronic configuration is favourable for tetrahedral bonding to the oxygen ions. It is known that Li^{1+}(0.70Å), Ni^{2+}(0.78Å) and Mg^{2+}(0.80Å) ions occupy B sites [6]. Hence the factors influencing the distribution the cations among the two possible lattice sites are mainly their ionic radii of the specific ions, the size of the interstices, temperature, the matching of their electronic configuration to the surrounding anions and the electrostatic energy of the lattice, the so-called Madelung energy, which has the predominant contribution to the lattice energy under the constrain of overall energy minimization and charge neutrality.

2.5 Interaction between magnetic moments on lattice sites

Spontaneous magnetization of spinels (at 0K) can be estimated on the basis of their composition, cation distribution, and the relative strength of the possible interaction. Since cation-cation distances are generally large, direct (ferromagnetic) interactions are negligible. Because of the geometry of orbital involved, the strongest super-exchange interaction is expected to occur between octahedral and tetrahedral cations. The strength of interaction or exchange force between the moments of the two metal ions on different sites depends on the distances between these ions and the oxygen ion that links them and also on the angle between the three ions. The nearest neighbours of a tetrahedral, an octahedral and an anion site are shown in Fig. 2.3. The interaction is greatest for an angle of 180^0 and also where the interionic distances are the shortest.
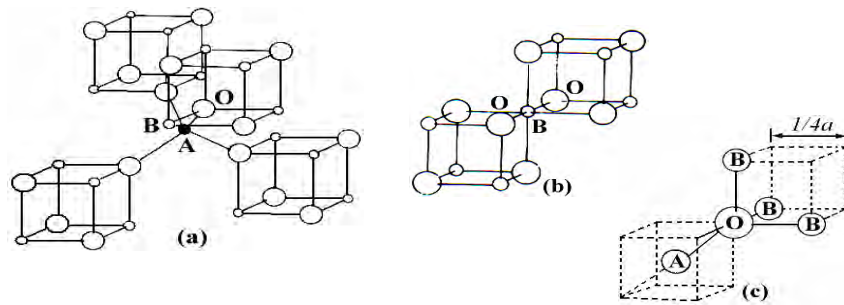
Fig. 2.3 Nearest neighbours of (a) a tetrahedral site, (b) an octahedral site and (c) an anion site.
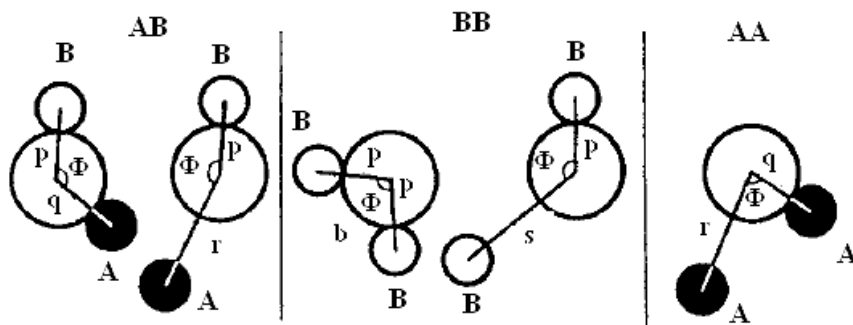
Fig. 2.4 Interionic distances and angles in the spinel structure for the different type of lattice site interactions [28, 29].

Distances M-O	Distances M-M
$p = a(\frac{1}{2} - u)$	$b = (a/4)\sqrt{2}$
$q = a(u - \frac{1}{4})\sqrt{3}$	$c = (a/8)\sqrt{11}$
$r = a(1+u)\sqrt{11}$	$d = (a/4)\sqrt{3}$
$s = a(\frac{1}{3}u + 8)\sqrt{3}$	$e = (3a/8)\sqrt{3}$
	$f = (a/4)\sqrt{6}$

Fig. 2.4 shows the inter-atomic distances and the angles between the ions for the different types of interactions. In the A-A and B-B cases, the angles are too small or the distances between the metal ions and the oxygen ions are too large. The best combinations of distances and angles are found in the A-B interactions. For an undistorted spinel, the A-O-B angles are about 125˚ and 154˚ [1-2, 24]. The B-O-B

angles are 90˚ and 125˚ but in the latter, one of the B-O distances is large. In the A-A case the angle is about 80˚. Therefore, the interaction between moments on the A and B sites is strongest. The B-B interaction is much weaker and the most unfavorable situation occurs in the A-A interaction. By examining the interactions involving the major contributor, or the A-B interaction which orients the unpaired spins of these ions antiparallel, Néel was able to explain the ferrimagnetism of ferrites. The interaction between the tetrahedral and octahedral sites is shown in Fig. 2.4. An individual A site is interacted with a single B site, but each A site is linked to four such units and each B site is linked to six such units. Thus, to be consistent throughout the crystal, all A sites and all B sites act as unified blocks and are coupled antiparallel as blocks [28].

2.6 Magnetism in spinel ferrite

The magnetic moment of a free atom is associated with the orbital and spin motions of electrons in an incomplete sub-shell of the electronic structure of the atom. In crystals the orbital motions are quenched, that is the orbital planes may be considered to be fixed in space relative to the crystal lattice, and in such a way that in bulk the crystal has no resultant moment from this source. Moreover this orbital-lattice coupling is so strong that the application of a magnetic field has little effect upon it. The spin axes are not tightly bound to the lattice as are the orbital axes. The anions surrounding a magnetic cation subject it to a strong inhomogeneous electric field and influence the orbital angular momentum. However, the spin angular momentum remains unaffected. For the first transition group elements this crystal field effect is intense partly due to the large radius of the 3d shell and partly due to the lack of any outer electronic shell to screen the 3d shell whose unpaired electrons only contribute to the magnetic moment.

We have originally defined the magnetic moment in connection with permanent magnets. The electron itself may well be called the smallest permanent magnet [1]. For an atom with a resultant spin quantum number *S,* the spin magnetic moment will be

$$\mu = g\sqrt{S(S+1)}\mu_B$$

where *g* is the Landé splitting factor and μ_B, known as the Bohr magneton, is the fundamental unit of magnetic moment. The value of *g* for pure spin moment is 2 and the quantum number associated with each electron spin is $\pm 1/2$. The direction of the moment is comparable to the direction of the magnetization (from South to North poles) of a permanent magnet to which the electron is equivalent.
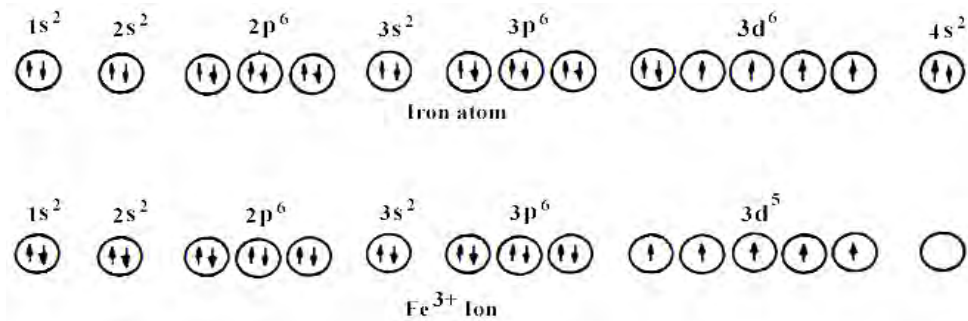
Fig. 2.5 Electronic configuration of atoms and ions [28].

Fig. 2.5 illustrates the electronic configuration of *Fe* atoms and Fe^{3+} ions. *Fe* atom has four unpaired electrons and Fe^{3+} ion has five unpaired electrons. Each unpaired electron spin produced 1 Bohr magneton. In compounds, ions and molecules, account must be taken of the electrons used for bonding or transferred in ionization. It is the number of unpaired electrons remaining after these processes occur that gives the net magnetic moment [1]. According to the Hund's rules the moment of *Fe* atom and Fe^{3+} ion are $4\mu_B$ and $5\mu_B$ respectively. Similarly the moment of Fe^{2+} and Ni^{2+} ion are $4\mu_B$ and $2\mu_B$ respectively.

2.6.1 Magnetic moments of some spinels ferrites

2.6.1.1 Inverse spinels

In the nickel ferrite it was observed that the moments of the eight Ni^{2+} ions on the octahedral sites. The value of moment per Ni^{2+}ion is $2\mu_B$ or $16\mu_B$ for a unit cell containing eight formula units. The magnetic moments of the other inverse spinels can be predicted in a similar manner. These predicted values are listed in Table 2.2 along with the measured values [28]. Because the effect of thermal agitation on the magnetic moments will lower the magnetic moment, the correlation of the moment to Bohr magnetons is always referred to the value at absolute zero or 0˚K. This is usually done by extrapolation of the values at very low temperatures. The deviations from the theoretical values can be attributed to several factors, namely:

- The ion distribution on the various sites may not be as perfect as predicted.

- The orbital magnetic contribution may not be zero as assumed.

- The directions of the spins may not be antiparallel in the interactions. In other words, they may be canted.

2.6.1.2 Normal versus inverse spinels

Although some spinels are either normal or inverse, it is possible to get different mixtures of the two. Often, the ratio of the two will depend on the method of preparation. Some of the first ferrites studied by Néel (1948) were ones that contained *Mg* and *Cu* which by thermal treatment reduced the Fe^{3+} on the tetrahedral A sites of the inverse spinel. As a result, there was an imbalance of the Fe^{3+} ions on the two sites and

thus a magnetic moment. Even *Zn* ferrite, *Zn [Fe₂] O₄* with a higher than 50 mole percentage of Fe_2O_3 and a special firing can have a small moment [28].

From the Table 2.2, it is observed that experimental magnetic moment of $Li_{0.5}Fe_{2.5}O_4$, and $NiFe_2O_4$ are 2.6, and 2.3 respectively.

Table 2.2 Magnetic moment of some simple ferrite [28].

Ferrite	Magnetic Moment (μ_B)	
	Experimental	Theoretical
$MnFe_2O_4$	4.6	5
$FeFe_2O_4$	4.1	4
$CoFe_2O_4$	3.7	3
$NiFe_2O_4$	2.3	2
$CuFe_2O_4$(Quenched)	2.3	1
$MgFe_2O_4$	1.1	0
$Li_{0.5}Fe_{2.5}O_4$	2.6	2.5
γ-Fe_2O_3	2.3	2.5

2.6.2 Exchange interactions in spinel

The intense short-range electrostatic field, which is responsible for the magnetic ordering, is the exchange force that is quantum mechanical in origin and is related to the overlapping of total wave functions of the neighbouring atoms. The total wave function consists of the orbital and spin motions. Usually the net quantum number is written as *S*, because the magnetic moments arise mostly due to the spin motion as described above.

The exchange interactions coupling the spins of a pair of electrons are proportional to the scalar product of their spin vectors [23, 26, 30].

$$V_{ij} = -2J_{ij} \vec{S}_{i.} . \vec{S}_j \qquad (2.1)$$

where J_{ij} is the exchange integral given in a self explanatory notation by

$$J_{ij} = \int \psi_i^*(1)\psi_j^*(2)\left[\frac{1}{r_{12}} + \frac{1}{r_{ij}} - \frac{1}{r_{i1}} - \frac{1}{r_{j2}}\right]\psi_i(2)\psi_j(2)dv_1 dv_2 \qquad (2.2)$$

In this expression r 's are the distances, subscripts i and j refer to the atoms, 1 and 2 refers to the two electrons. If the J in equation (2.1) is positive, we achieve ferromagnetism. A negative J may give rise to anti-ferromagnetism or ferrimagnetism.

Magnetic interactions in spinel ferrites as well as in some ionic compounds are different from the one considered above because the cations are mutually separated by bigger anions (oxygen ions). These anions obscure the direct overlapping of the cation charge distributions, sometimes partially and sometimes completely making the direct exchange interaction very weak. Cations are too far apart in most oxides for a direct cation-cation interaction. Instead, super-exchange interactions appear, i.e., indirect exchange via anion *p*-orbitals that may be strong enough to order the magnetic moments. Apart from the electronic structure of cations this type of interactions strongly depends on the geometry of arrangement of the two interacting cations and the intervening anion. Both the distance and the angles are relevant. Usually only the interactions with in first coordination sphere (when both the cations are in contact with the anion) are important. In the Néel theory of ferrimagnetism the interactions taken as effective are inter- and intra-sub-lattice interactions *A-B*, *A-A* and *B-B*. The type of magnetic order depends on their relative strength. The super-exchange mechanism between cations that operate via the intermediate anions was proposed by Kramer for

such cases and was developed by Anderson and Van Vleck [23, 26]. A simple example

of super-exchange is provided by *MnO* which was chosen by Anderson. From the

crystal structure of *MnO* it will be seen that the anti-parallel manganese ions are

collinear with their neighbouring oxygen ions. The O^{2-} ions each have six *2p* electrons

in three anti-parallel pairs. The outer electrons of the Mn^{2+} ions are in *3d* sub-shells

which are half filled with five electrons in each. The phenomenon of super-exchange is

considered to be due to an overlap between the manganese 3d orbits and the oxygen *2p*

orbits with a continuous interchange of electrons between them. It appears that, for the

overall energy of the system to be a minimum, the moments of the manganese ions on

either side of the oxygen ion must be anti-parallel. The manganese magnetic moments

are thus, in effect, coupled through the intervening oxygen ion. The idea is illustrated in

Fig. 2.6.
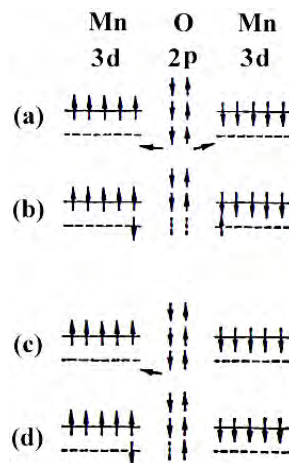
Fig. 2.6 Illustrating super-exchange in *MnO*.

In Fig. 2.6 (a) and Fig. 2.6 (c) the outer electrons in a pair of Mn^{2+} ions, and in

an intervening O^{2-} ion in the unexcited state, are shown by the arrows. One suggested

mode of coupling is indicated in Fig. 2.6 (b). The two electrons of a pair in the oxygen

ion are simultaneously transferred, one to the left and the other to the right. If their

directions of spin are unchanged then, by Hund''s rules, the moments of the two manganese ions must be anti-parallel as shown. Another possibility is represented in Fig. 2.6(d). One electron only has been transferred to the manganese ion on the left. The oxygen ion now has a moment of $1\mu_B$ and if there is negative interaction between the oxygen ion and the right-hand manganese ion then again the moments of the manganese ions will be anti-parallel. If these ideas are accepted then the oxygen ions play an essential part in producing anti-ferromagnetism in the oxide. Moreover, because of the dumbbell shape of the *2p* orbits, the coupling mechanism should be most effective when the metal ions and the oxygen ions lie in one straight line, that is, the angle between the bonds is 180˚, and this is the case with *MnO*.

In the case of spinel ferrites the coupling is of the indirect type which involves overlapping of oxygen wave functions with those of the neighbouring cations. Consider two transition metal cations separated by an *O,* Fig. 2.7.

Cation   **Oxygen**   **Cation**
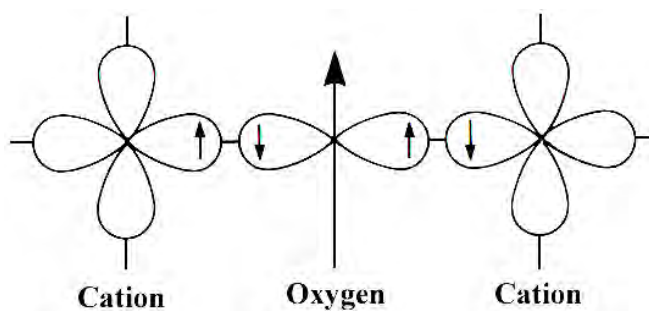
Fig. 2.7 Schematic representation of the super-exchange interaction in the magnetic oxides. The *p* orbital of an anion (center) interact with the *d* orbitals of the transitional metal cations.

The O^{2-} has no net magnetic moment since it has completely filled shells, with *p*-type outermost orbitals. Orbital p_x has two electrons: one with spin up, and the other with spin down, consistent with pauli''s exclusion principle. The essential point is that when an oxygen *p* orbital overlaps with a cation *d* orbital, one of the *p* electrons can be

accepted by the cations. When one of the transition-metal cations is brought close the O^{2-}, partial electron overlap (between a *3d* electron from the cation and a *2p* electron form the O^{2-}) can occur only for anti-parallel spins, because electrons with the same spin are repelled. Empty *3d* states in the cation are available for partial occupation by the O^{2-} electron, with an anti-parallel orientation. Electron overlap between the other cation and the O^{2-} then occurs resulting in anti-parallel spins and therefore anti-parallel order between the cations. Since the *p* orbitals are linear, the strongest interaction is expected to take place for cation–O^{2-}–cation angles close to 180° [2].

2.6.3 Néel theory of ferrimagnetism

If we consider the simplest case of a two sub-lattice system having antiparallel and non-equal magnetic moments, the inequality may be due to:

1) different elements in different sites,

2) same element in different ionic states, and

3) different crystalline fields leading to different effective moments for ions having the same spin.

The spins on one sub-lattice are under the influence of exchange forces due to the spins on the second sub-lattice as well as due to other spins on the same sub-lattice. The molecular fields acting on the two sub-lattices A and B can be written as [2, 23-27]

$$\vec{H}_A = \lambda_{AA}\vec{M}_A + \lambda_{AB}\vec{M}_B,$$

$$\vec{H}_B = \lambda_{AB}\vec{M}_A + \lambda_{BB}\vec{M}_B$$

Where $\vec{M}_A$ and $\vec{M}_B$ are the magnetizations of the two sub-lattices and λ "s are the Weiss constants. Since the interaction between the sub-lattices is anti-ferromagnetic, λ_{AB} must be negative, but λ_{AA} and λ_{BB} may be negative or positive depending on the

crystal structure and the nature of the interacting atoms. Probably, these interactions are also negative, though they are in general quite small.

Assuming all the exchange interactions to be negative the molecular fields will be then given by

$$\vec{H}_A = -\lambda_{AA}\vec{M}_A - \lambda_{AB}\vec{M}_B,$$

$$\vec{H}_B = -\lambda_{AB}\vec{M}_A - \lambda_{BB}\vec{M}_B$$

Since in general, λ_{AA} and λ_{BB} are small compared to λ_{AB}, it is convenient to express the strengths of these interactions relative to the dominant λ_{AB} interaction.

Let $\lambda_{AA} = \alpha\lambda_{AB}$

And $\lambda_{BB} = \beta\lambda_{AB}$

In an external applied field $\vec{H}$, the fields acting on A and B sites are

$$\vec{H}_A = \vec{H} - \lambda_{AB}(\alpha\vec{M}_A - \vec{M}_B),$$

$$\vec{H}_B = \vec{H} - \lambda_{AB}(\vec{M}_A - \beta\vec{M}_B)$$

At temperatures higher than the transition temperature, T_N, $\vec{H}_A$, $\vec{M}_A$ and $\vec{M}_B$ are all parallel and we can write

$$\vec{M}_A = \frac{C_A}{T}[\vec{H} - \lambda_{AB}(\alpha\vec{M}_A - \vec{M}_B)], \tag{2.3}$$

$$\vec{M}_B = \frac{C_B}{T}[\vec{H} - \lambda_{AB}(\vec{M}_A - \beta\vec{M}_B)] \tag{2.4}$$

where C_A and C_B are the Curie constants for the two sub-lattices.

Here, $C_A = N_A g\mu_B^2 S_A(S_A + 1)/3K$ and $C_B = N_B g\mu_B^2 S_B(S_B + 1)/3K$

N_A and N_B denote the number of magnetic ions on A and B sites respectively and S_A and S_B are their spin quantum numbers. Solving for the susceptibility, χ, one gets [2,27]

$$\frac{1}{\chi} = \frac{T}{C} - \frac{1}{\chi_0} - \frac{b}{T - \theta}$$

$$\frac{1}{\chi} = \frac{T + (C/\chi_0)}{C} - \frac{b}{T - \theta} \qquad\qquad (2.5)$$

where C, χ_0, b and θ are constants for particular substance and are given by

$$C = C_A + C_B$$

$$\frac{1}{\chi_0} = -\frac{1}{C^2}[C_A^2 \lambda_{AA} + C_B^2 \lambda_{BB} + 2 C_A C_B \lambda_{AB}]$$

$$b = \frac{C_A C_B}{C^3}[C_A^2 (\lambda_{AA} - \lambda_{BB})^2 + C_B^2 (\lambda_{BB} - \lambda_{AB})^2$$

$$- 2 C_A C_B \{\lambda_{AB}^2 - (\lambda_{AA} + \lambda_{BB})\lambda_{AB} + \lambda_{AA}\lambda_{BB}\}]$$

$$\theta = -\frac{C_A C_B}{C}(\lambda_{AB} + \lambda_{BB}) - 2\lambda_{AB}$$

Equation (2.5) represents a hyperbola, and the physically meaning part of it is plotted in Fig. 2.9. This curvature of the plot of $1/\chi$ versus T is a characteristics feature of a ferrimagnet. It cuts the temperature axis at T_C, called the Ferrimagnetic Curie point. At high temperatures the last term of equation (2.5) become negligible, and reduces to a Curie-Weiss law:

$$\chi = \frac{C}{T + (C/\chi_0)}$$

This is the equation of straight line, shown dashed in Fig. 2.9, to which the $1/\chi$ versus T curve becomes asymptotic at high temperatures.
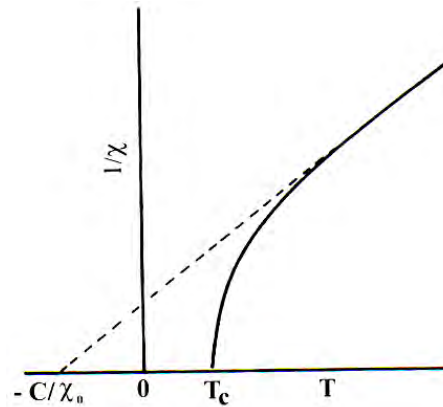
Fig. 2.8 The temperature dependence of the inverse susceptibility for ferrimagnets.

The ferrimagnetic Curie temperature T_C is obtained from equations (2.3) and (2.4) with $H = 0$ and setting the determinant of the coefficients of M_i equal to zero. This gives

$$T_C = \frac{1}{2}[C_A\lambda_{AA} + C_B\lambda_{BB} + \{(C_A\lambda_{AA} - C_B\lambda_{BB})^2 + 4C_AC_B\lambda_{AB}^2\}^2] \tag{2.6}$$

Equation (2.5) is in good agreement with the experiment, except near the Curie point. The experimental Curie temperature, the temperature at which the susceptibility becomes infinite and spontaneous magnetization appears, is lower than the theoretical Curie temperature [27]. This disagreement between theory and experiment in the region of Curie point is presumably due to the short-range spin order (spin clusters) at temperatures above experimental T_C [2, 27]. The sub-lattice magnetizations will in general have different temperature dependences because the effective molecular fields acting on them are different. This suggests the possibility of having anomaly in the net magnetization versus temperature curves, Fig. 2.9. For most ferrimagnets the curve is similar to that of ferromagnets, but in a few cases there be a compensation point in the curve, Fig. 2.9(c) [1, 27]. At a point below the Curie temperature point, the two sub-lattice magnetizations are equal and thus appear to have no moment. This temperature is called the compensation point. Below this temperature one sub-lattice magnetization is

larger and provides the net moment. Above this temperature the other magnetization does dominates and the net magnetization reverses direction.

The essential requisite for Néel configuration is a strong negative exchange interaction between *A* and *B* sub-lattices which results in their being magnetized in opposite directions below the transition point. But there may be cases where intra-sublattice interactions are comparable with inter-sublattice interaction. Néel's theory predicts paramagnetism for such substances at all temperatures. This is unreasonable since strong *AA* or *BB* interaction may lead to some kind of ordering especially at low temperature. In the cases of no *AB* interaction, antiferromagnetic ordering may be expected either in the *A* or in the *B* sub-lattice. Under certain conditions there may be non-collinear spin arrays of still lower energy.
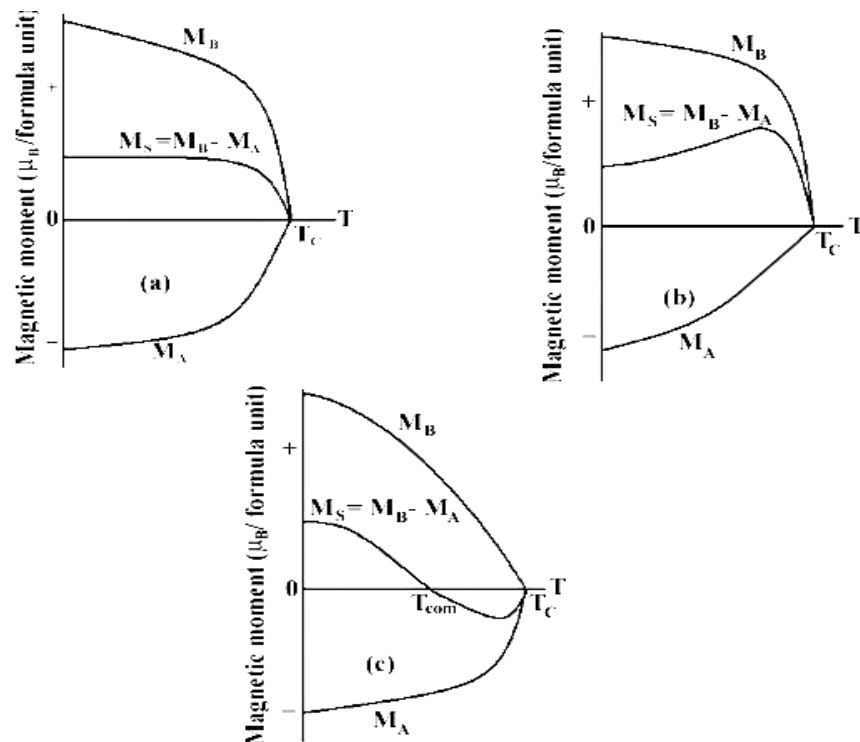
Fig. 2.9 Superposition of various combinations of two opposing sub-lattice magnetizations producing differing resultants including one with a compensation point (schematic).

2.7 Microstructure

A polycrystal is much more than many tiny crystals bonded together. The interfaces between the crystals, or the grain boundaries which separate and bond the grains, are complex and interactive interfaces. The whole set of a given material"s properties (mechanical, chemical and especially electrical and magnetic) depend strongly on the nature of the microstructure. In the simplest case, the grain boundary is the region, which accommodates the difference in crystallographic orientation between the neighbouring grains. For certain simple arrangements, the grain boundary is made of an array of dislocations whose number and spacing depends on the angular deviation between the grains. The ionic nature of ferrites leads to dislocation patterns considerably more complex than in metals, since electrostatic energy accounts for a significant fraction of the total boundary energy [2].

For low-loss ferrite, Ghate [1] states that the grain boundaries influence properties by

1) creating a high ressistivity intergranular layer,

2) acting as a sink for impurities which may act as a sintering aid and grain growth modifiers,

3) providing a path for oxygen diffusion, which may modify the oxidation state of cations near the boundaries.

In addition to grain boundaries, ceramic imperfections can impede domain wall motion and thus reduce the magnetic property. Among these are pores, cracks, inclusions, second phases, as well as residual strains. Imperfections also act as energy wells that pin the domain walls and require higher activation energy to detach. Stresses are microstructural imperfections that can result from impurities or processing problems

such as too rapid a cool. They affect the domain dynamics and are responsible for a much greater share of the degradation of properties than would expect [1].

Grain growth kinetics depends strongly on the impurity content. A minor dopant can drastically change the nature and concentration of defects in the matrix, affecting grain boundary motion, pore mobility and pore removal [2, 41]. The effect of a given dopant depends on its valence and solubility with respect to host material. If it is not soluble at the sintering temperature, the dopant becomes a second phase which usually segregates to the grain boundary.
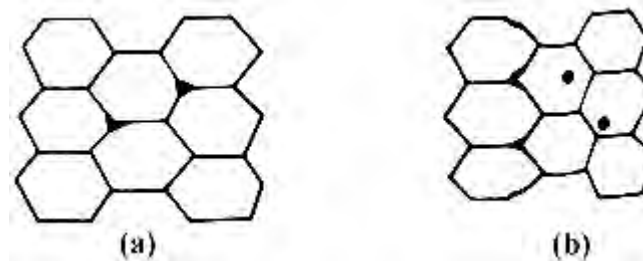
Fig. 2.10 Porosity character: (a) intergranular, (b) intragranular.

The porosity of ceramic samples results from two sources, intragranular porosity and intergranular porosity, Fig. 2.12. An undesirable effect in ceramic samples is the formation of exaggerated or discontinuous grain growth which is characterized by the excessive growth of some grains at the expense of small, neighbouring ones (Fig. 2.13). When this occurs, the large grain has a high defect concentration. Discontinuous growth is believed to result from one or several of the following: powder mixtures with impurities; a very large distribution of initial particle size; sintering at excessively high temperatures; in ferrites containing *Zn* and /or *Mn*, a low O_2 partial pressure in the sintering atmosphere. When a very large grain is surrounded by smaller ones, it is called „duplex" microstructure.
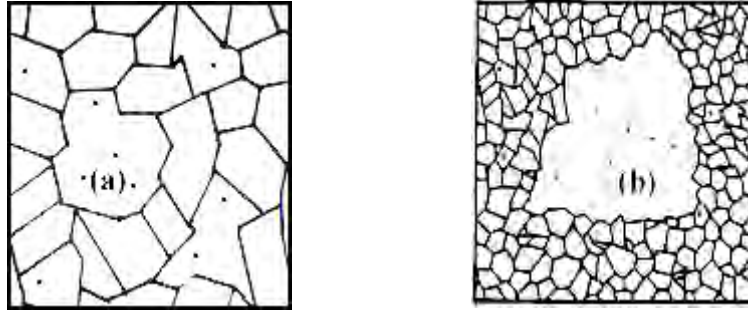
Fig. 2.11 Grain growth (a) discontinuous, (b) duplex (schematic).

2.8 Theories of permeability

Permeability is defined as the proportionality constant between the magnetic field induction B and applied field intensity H [2, 24, 34]:

$$B = \mu H \tag{2.7}$$

If the applied field is very low, approaching zero, the ratio will be called the initial permeability, Fig. 2.15 and is given by

$$\mu_i = \frac{\Delta B}{\Delta H}_{(\Delta H \to 0)}$$

This simple definition needs further sophistications. A magnetic material subjected to an ac magnetic field can be written as

$$H = H_0 e^{i\omega t} \tag{2.8}$$

It is observed that the magnetic flux density B lag behind H. This is caused due to the presence of various losses and is thus expressed as

$$B = B_0 e^{i(\omega t - \delta)} \tag{2.9}$$

Here δ is the phase angle that marks the delay of B with respect to H. The permeability is then given by

$$\mu = \frac{B}{H} = \frac{B_0 e^{i(\omega t - \delta)}}{H_0 e^{i\omega t}} = \frac{B_0 e^{-i\delta}}{H_0} = \frac{B_0}{H_0}\cos\delta - i\frac{B_0}{H_0}\sin\delta = \mu' - i\mu'' \tag{2.10}$$

where $\qquad \mu^{/} = \dfrac{B_0}{H_0} \cos\delta$ (2.11)

and $\qquad \mu^{//} = \dfrac{B_0}{H_0} \sin\delta$ (2.12)
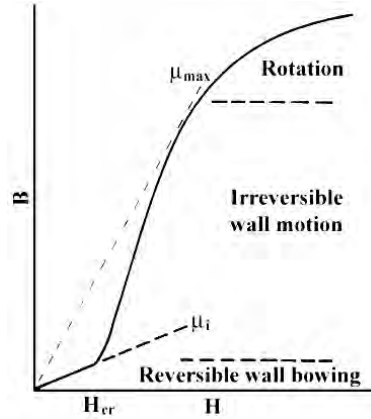
Fig. 2.12 Schematic magnetization curve showing the important parameter: initial permeability, μ_i (the slope of the curve at low fields) and the main magnetization mechanism in each magnetization range [2].

The real part ($\mu^{/}$) of complex permeability (μ), as expressed in equation (2.10) represents the component of *B* which is in phase with *H*, so it corresponds to the normal permeability. If there are no losses, we should have $\mu = \mu^{/}$. The imaginary part $\mu^{//}$ corresponds to that of *B*, which is delayed by phase angle 90° from *H* [23, 30]. The presence of such a component requires a supply of energy to maintain the alternating magnetization, regardless of the origin of delay. The ratio of $\mu^{//}$ to $\mu^{/}$, as is evident from equation (2.12) and (2.11) gives

$$\frac{\mu^{//}}{\mu^{/}} = \frac{\dfrac{B_0}{H_0}\sin\delta}{\dfrac{B_0}{H_0}\cos\delta} = \tan\delta \qquad (2.13)$$

This $\tan\delta$ is called loss factor.

The quality factor is defined as the reciprocal of this loss factor, i.e.

$$\text{Quality factor} = \frac{1}{\tan \delta} \tag{2.14}$$

$$\text{And the relative quality factor, } Q = \frac{\mu^{/}}{\tan \delta} \tag{2.15}$$

The curves that show the variation of both $\mu^{/}$ and $\mu^{//}$ with frequency are called the magnetic spectrum or permeability spectrum of the material [27]. The variation of permeability with frequency is referred to as dispersion. The measurement of complex permeability gives us valuable information about the nature of domain wall and their movements. In dynamic measurements the eddy current loss is very important. This occurs due to the irreversible domain wall movements. The permeability of a ferrimagnetic substance is the combined effect of the wall permeability and rotational permeability mechanisms.

2.8.1 Mechanisms of permeability

The mechanisms can be explained as follows: A demagnetized magnetic material is divided into number of Weiss domains separated by Bloch walls. In each domain all the magnetic moments are oriented in parallel and the magnetization has its saturation value M_s. In the walls the magnetization direction changes gradually from the direction of magnetization in one domain to that in the next. The equilibrium positions of the walls result from the interactions with the magnetization in neighbouring domains and from the influence of pores; crystal boundaries and chemical inhomogeneities which tend to favour certain wall positions.

2.8.1.1 Wall permeability

The mechanism of wall permeability arises from the displacement of the domain walls in small fields. Lets us consider a piece of material in the demagnetized state, divided into Weiss domains with equal thickness L by means of 180° Bloch walls (as in the Fig. 2.15). The walls are parallel to the YZ plane. The magnetization M_s in the domains is oriented alternately in the $+Z$ or $-Z$ direction.
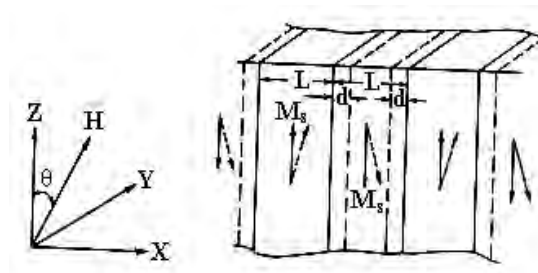
Fig 2.13 Magnetization by wall motion and spin rotation.

When a field H with a component in the $+Z$ direction is applied, the magnetization in this direction will be favoured. A displacement dx of the walls in the direction shown by the dotted lines will decrease the energy density by an amount [35, 36]:

$$\frac{2M_s H_z dx}{L}$$

This can be described as a pressure $M_s H_z$ exerted on each wall. The pressure will be counteracted by restoring forces which for small deviations may assume to be kdx per unit wall surface. The new equilibrium position is then given by

$$d = \frac{M_s H_z dx}{L}$$

From the change in the magnetization

$$\Delta M = \frac{2M_s d}{L},$$

41

the wall susceptibility χ_w may be calculated. Let H makes the angle θ with Z direction. The magnetization in the θ direction becomes

$$(\Delta M)_\theta = \frac{2M_s d}{L}\cos\theta , \text{ And with } H_z = H\cos\theta \text{ and } d = \frac{2M_s H_z}{K}$$

we obtain

$$\chi_w = \frac{(\Delta M)_\theta}{H} = \frac{4M_s^2 \cos^2\theta}{KL} \tag{2.16}$$

2.8.1.2 Rotational permeability

The rotational permeability mechanism arises from rotation of the magnetization in each domain. The direction of M can be found by minimizing the magnetic energy E as a function of the orientation. Major contribution to E comes from the crystal anisotropy energy. Other contributions may be due to the stress and shape anisotropy. The stress may influence the magnetic energy via the magnetostriction. The shape anisotropy is caused by the boundaries of the sample as well as by pores, nonmagnetic inclusions and inhomogeneities. For small angular deviations, α_x and α_y may be written as

$$\alpha_x = \frac{M_x}{M_s} \text{ and } \alpha_y = \frac{M_y}{M_s} .$$

For equilibrium Z-direction, E may be expressed as [36]

$$E = E_0 + \frac{1}{2}\alpha_x^2 E_{xx} + \frac{1}{2}\alpha_y^2 E_{yy}$$

where it is assumed that x and y are the principal axes of the energy minimum. Instead of E_{xx} & E_{yy}, the anisotropy field H_x^A and H_y^A are often introduced. Their magnitude is given by

$$H_x^A = \frac{E_{xx}}{2M_s} \text{ and } H_y^A = \frac{E_{yy}}{2M_s},$$

H_x^A & H_y^A represent the stiffness with which the magnetization is bound to the equilibrium direction for deviations in x and y direction, respectively. The rotational susceptibilities $\chi_{r,x}$ and $\chi_{r,y}$ for fields applied along x and y directions, respectively are

$$\chi_{r,x} = \frac{M_s}{H_x^A} \text{ and } \chi_{r,y} = \frac{M_s}{H_y^A}.$$

For cubic materials it is often found that H_x^A and H_y^A are equal. For $H_x^A = H_y^A = H^A$ and a field H which makes an angle θ with the Z direction (as shown in Fig. 2.15) the rotational susceptibility, $\chi_{r,c}$ in one crystallite becomes

$$\chi_{r,c} = \frac{M_s}{H^A} \sin^2 \theta \qquad\qquad (2.17)$$

A polycrystalline material consisting of a large number of randomly oriented grains of different shapes, with each grain divided into domains in a certain way. The rotational susceptibility χ_r of the material has to be obtained as a weighted average of $\chi_{r,c}$ of each crystallite, where the mutual influence of neighbouring crystallites has to be taken into account. If the crystal anisotropy dominates other anisotropies, then H^A will be constant throughout the material, so only the factor $\sin^2 \theta$ (equation 2.17) has to be averaged. Snoek [36] assuming a linear averaging of $\chi_{r,c}$ and found

$$\chi_r = \frac{2M_s}{3H^A}$$

The total internal susceptibility

$$\chi = \chi_w + \chi_r = \frac{4M_s^2 \cos^2 \theta}{KL} + \frac{2M_s}{3H^A} \tag{2.18}$$

If the shape and stress anisotropies cannot be neglected, H^A will be larger. Any estimate of χ_r will then be rather uncertain as long as the domain structure, and the pore distribution in the material are not known. A similar estimate of χ_w would require knowledge of the stiffness parameter k and the domain width L. These parameters are influenced by such factors as imperfection, porosity and crystallite shape and distribution which are essentially unknown.

2.8.2 Frequency dependent permeability curve

The techniques of impedance spectroscopy, widely used in dielectrics have been applied to magnetic materials [28]. In this method, impedance measurements as a function of frequency are modified by means of an equivalent circuit and its elements are associated with the physical parameters of the material. The complex permeability, μ^*, is determined from the complex impedance, Z^*, by:

$\mu^* = (jk/\omega) Z^*$ (2.19)

where k is the geometric constant relating to inductance , l, to the permeability. The equivalent circuit for domain wall bowing (applied field lower than critical field) is a parallel *RL* arrangement; for wall displacement, additional Warbarg-type impedance element is required (Irvine *et al.*) [37].
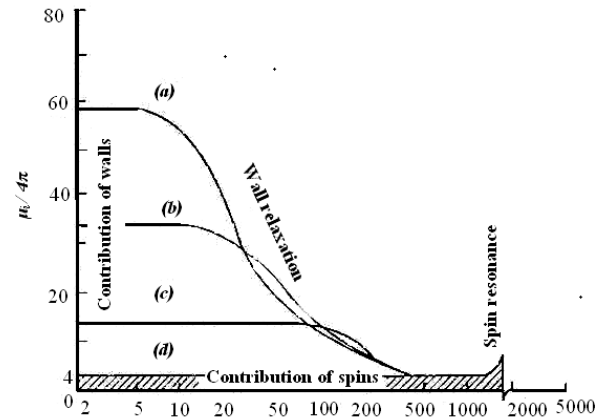
Fig. 2.14 Permeability spectra of *NiFe₂O₄* samples with different grain size: (a) 11µm;(b) 5µm;(c) 2 µm (d)size <0.2 µm(single domain behaviour) [2]
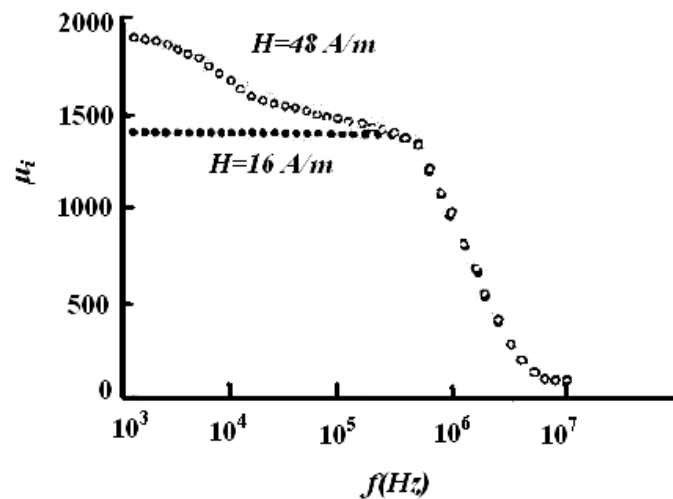
Fig. 2.15 Permeability spectrum of a *Ni-Zn* sample at fields above (open circles) and below (filled circles) the critical field [38].

Many of the specific applications of ferrites depend on their behaviour at high frequencies. When subjected to an ac field, ferrite permeability shows several dispersions; as the field frequency increases, the various magnetization mechanisms become unable to follow the field. The dispersion frequency for each mechanism is different time constants, Fig. 2.16. The low frequency dispersions are associated with

45

domain wall dynamics and the high frequency dispersion, with spin resonance. The spin resonance phenomena occur usually in the GHz range. The two main magnetization mechanisms are wall bowing and wall displacement as discussed before in section 2.8. Any field results in a bowing of pinned walls, and if this field has higher value than the corresponding critical field, walls are unpinned and displaced. Otherwise, bowed walls remain pinned to material defects. Measurements at low fields therefore show only one wall dispersion. Measurements at high fields, several, complex dispersions are observed, such as those in Fig. 2.17. Wall displacement dispersion occurs at lower frequencies than wall bowing, since hysteresis is a more complex phenomenon of wall bowing, unpinning, displacement and pinning steps.
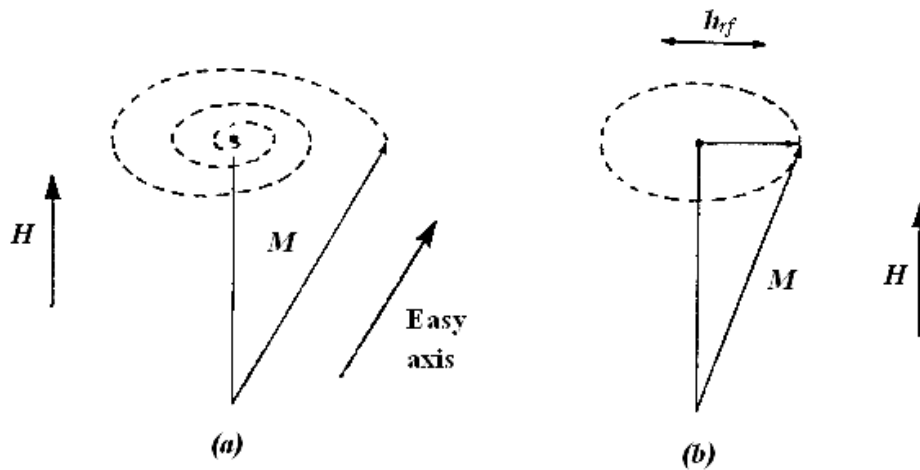
Fig. 2. 16 (a) Schematic representation of the spin deviation from an easy axis by precessional spiralling into the field direction, (b) Precession is maintained by a perpendicular rf field, h_{rf} [2].

At very high frequencies, domain walls are unable to follow the field and the only remaining megnetisation mechanism is spin rotation within domains. This mechanism eventually also shows a dispersion, which always takes the form of a resonance. Spins are subjected to the anisotropy field, representing spin-lattice coupling;

as an external field is applied (out of the spins" easy direction), spins experience a torque. However, the response of spins is not instantaneous; spins precess around the field direction for a certain time (the relaxation time, τ) before adopting the new orientation, Fig. 2.18.

The frequency of this precession is given by the Larmor frequency:

$$\omega_L = \gamma\, \mu_o\, H_T \qquad\qquad (2.20)$$

where H_T is the total field acting on the spin.

$H_T = H_K + H + H_d + \ldots\ldots$, where H_K, H, H_d are the anisotropy and the external and demagnetization fields, respectively. If an ac field of angular frequency ω_L is applied to the sample, a resonant absorption (ferromagnetic resonance) occurs. The Larmour frequency is independent of the precession amplitude.

2.9 Magnetization mechanism

2.9.1 Concept of magnetic domain and domain wall (Weiss domain Structure)

In 1907 Pierre Weiss in his paper "Hypothesis of the molecular field" [29, 39] postulated that a ferromagnetic material rather than be uniformly magnetized, is divided into a number of regions of domains, each of which is magnetized to saturation level but the direction of magnetization from domain to domain need not be parallel. The magnetization vectors are parallel to preferred direction such that the demagnetization field, and hence the demagnetization energy ($W_{dem.} = 1/8\pi\, H^2_D$) is as small as possible. The total magnetization is then given by the vector summation of individual magnetization over all domains. The demagnetized state of the magnet is from the view point of an observer outside the material. In ferromagnetic materials, the atomic magnetic moments aligned in parallel fashion, while in ferrite domain, the net moments

of the anti ferromagnetic interaction are spontaneously oriented parallel to each other (even without applied magnetic field) [40]. The applied field serves as a control in changing the balance of potential energy within the, magnetic material. These uniformly magnetized domains are separated by a thin layer in which the magnetization gradually changes from one orientation to another. This transition boundary is called domain wall or Bloch wall. The domain structure are found basically to reduce the magnetostatic energy i.e., the magnetic potential energy contained in the field lines (or flux lines) connecting north and south poles outside of the material. This concept can be understood by considering a simple case, as shown in Fig. 2.19, in which (a) to (e) represents a cross section of a ferromagnetic single crystal. In Fig. 2.19 (a) a single domain crystal is shown, the value of magnetostatic energy is high. The arrow indicates the direction of magnetization and hence the direction of spin alignment in the domain. If the crystal is divided into two domains (Fig. 2.19 (b), the magnetic energy will be reduced by roughly one half of the single domain case. This splitting process continues to lower the energy of the system until more energy is required to form the domain boundary. When a large domain is split into *n* domains, as shown in Fig. 2.19 (c) the magnetic energy will be reduced to approximately *1/n* of the magnetic energy of that of type (a). For the domain structure configuration in Fig. 2.19 (d) and (e), the magnetic energy is zero as the flux circuit is completed within a crystal, (i.e., flux path never leaves the boundary of the material). These triangular domains are callled closure domains. Therefore the magnetostatic energy is reduced. This type of structure may also be found at the surface of the material.
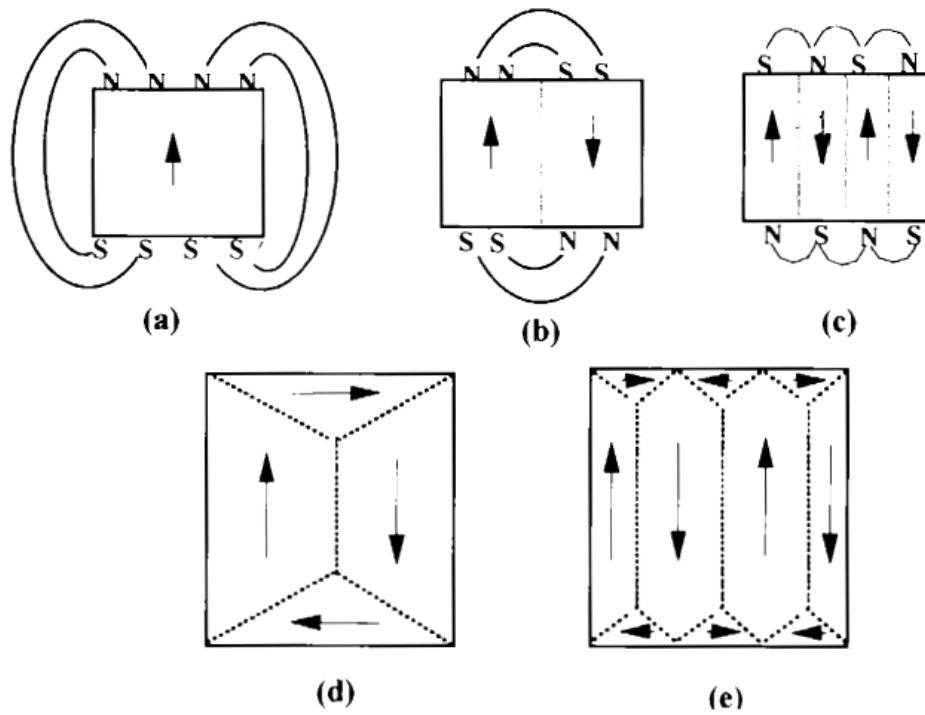
Fig. 2.17 Possible domain structures showing progressively low energy. Each part is representing a cross-section of a ferromagnetic single crystal [2, 28].

The boundaries between the domains, are not sharp on atomic scale but are spread over a finite thickness within which the direction of the spin changes gradually from one domain to the next [39]. The spin within a domain wall as shown in Fig. 2.20, are pointing in necessary directions, so that the crystal anisotropy energy within the wall is higher than it is in the adjacent domains. The exchange energy tries to align the spin in a direction parallel to the direction in the domain while the anisotropy energy tries to make the wall thin to minimize misalignment within the easy directions. The actual thickness of the domain wall is determined by the counterbalance of the exchange energy and anisotropy energy.
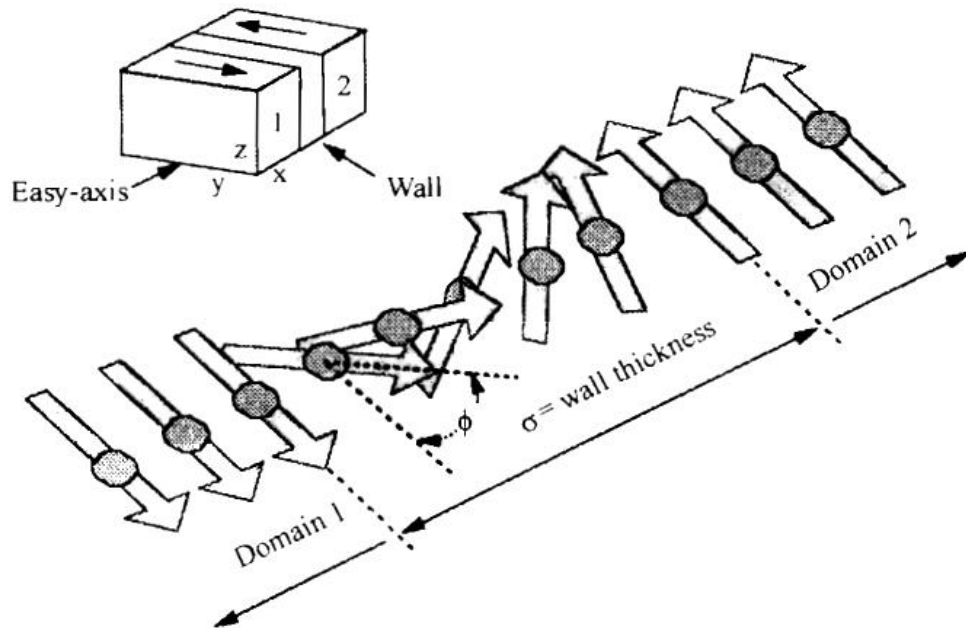
Fig. 2.18 Schematic representation of a domain wall. All spins, within the wall thickness are in non-easy direction [27].

2.9.2 The dynamic behaviour of domains

Two general mechanisms are involved in changing the magnetization in a domain and, therefore, changing the magnetization in a sample. The first mechanism acts by rotating the magnetization towards the direction of the field. Since this may involve rotating the magnetization from an axis of easy magnetization in a crystal to one of more difficult magnetization, a certain amount of anisotropy energy is required. The rotations can be small as indicated in Figure 2.21(a) or they can be almost the equivalent of a complete 180˚ reversal or flip if the crystal structure is uniaxial and if the magnetizing field is opposite to the original magnetization direction of the domain. The other mechanism for changing the domain magnetization is one in which the direction of magnetization remains the same, but the volumes occupied by the different domains may change. In this process, the domains whose magnetizations are in a direction closest

to the field direction grow larger while those that are more unfavorably oriented shrink in size. Fig. 2.21(b) shows this process which is called domain wall motion.

The mechanism for domain wall motion starts in the domain wall. Present in the wall is a force (greatest with the moments in the walls that are at an angle of 90˚ to the applied field) that will tend to rotate those moments in line with the field. As a result, the center of the domain wall will move towards the domain opposed to the field. Thus, the area of the domain with favorable orientation will grow at the expense of its neighbour.
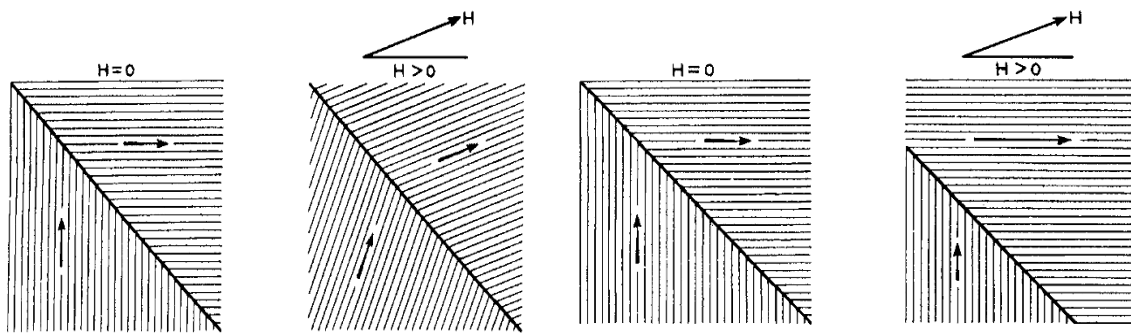
(a) Volume constant, directions changed   b) Volume changed, directions constant

Fig. 2.19 (a) Change of domain magnetization by domain wall movement and (b) Change of domain magnetization by domain rotation [28].

2.9.3 Bulk material magnetization

Although domains are not physical entities such as atoms or crystal lattices and can only be visualized by special means, for the purpose of magnetic structure they are important in explaining the process of magnetization. A material that has strongly oriented moments in a domain often has no resultant bulk material magnetization. Non-magnetic material can be transformed into a strongly magnetic body by domain dynamics discussed above. If the material has been demagnetized, the domains point in all random directions so that there is complete cancellation and the resultant

magnetization is zero (Fig. 2.22). The possible steps to complete orientation of the domains or magnetization of the material are also shown in Fig. 2.22 [28].
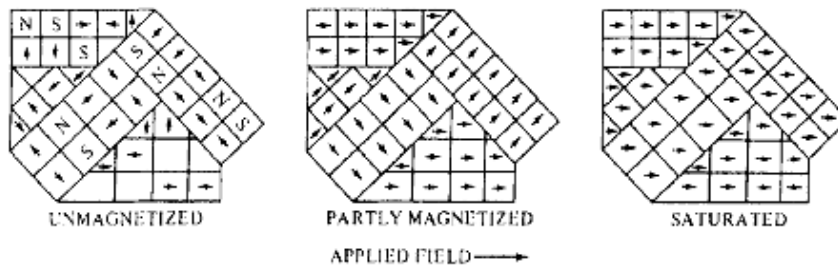
Fig. 2.20 Stages in magnetization of a sample containing several crystals [28].

2.9.4 The magnetization curve

For unmagnetized bulk material, there is a zero net magnetic moment. It can be predicted that there will be an infinite number of degree of magnetization between the unmagnetized and saturation condition, when the material is subjected to an external magnetic field. These extreme situation correspond respectively, to random orientation of domains complete alignment in one direction with elimination of domain walls. It can be started with the demagnetized specimen and increase the applied magnetic field and then the bulk material will be progressively magnetized by the domain dynamics. The magnetization of the sample will follow the course as shown in Fig. 2.23 (a) [28]. The slope from the origin to a point on the curve or the ratio *M/H* is defined as magnetic susceptibility. This curve is called Magnetization Curve. This curve is generally perceived as being made of three major portions. The first, the lower section, is the initial susceptibility region and is characterized by reversible domain wall movements and rotations. By reversible means that after the magnetization slightly with an increase in field the original magnetization conditions can be reversed if the field is reduced to

initial value. The contribution of the displacement walls to an initial permeability is entirely dependent on the sort of material studied.

In the second stage magnetization curve, if the field is increased, the intensity of the magnetization increases more drastically, is called the irreversible magnetization range. This range is obtained mainly by the irreversible domain wall motion from one stable state to another. If the field is increased further, the magnetization curve become less steep and its process become reversible once more.

(a)   (b)
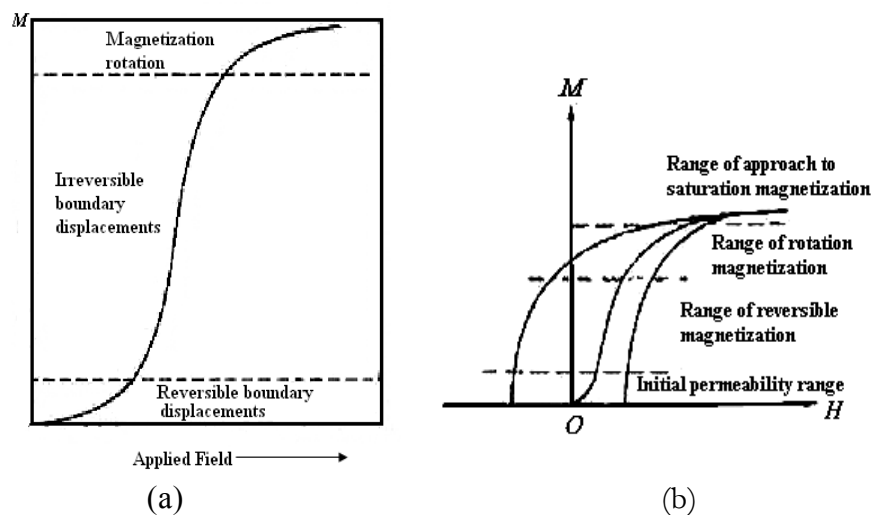
Fig. 2.21 Domain dynamics during various parts of the magnetization curve [28].

In the third section of magnetization curve, the displacement of domain walls has already been completed and the magnetization taken place by rotation magnetization. This range is called rotation magnetization range. Beyond this range the magnetization gradually approaches to saturation magnetization. (Fig. 2.21 (b))

References

[1]   Goldman, A., *Handbook of Modern Ferromagnetic Materials*, Kluwer Acad. Pub., Boston U.S.A, 1999.

[2]   Valenzuela, R., *Magnetic Ceramics*, Cambridge University Press, Cambridge, 1994.

[3]   Haque, M. M., "Influence of additives on the magnetic and electrical properties of iron-excess Mn-Zn ferrites", M. Phil. Thesis, BUET, Bangladesh, 2000.

[4]   Jefferson, C. F. and West, R. G., "Ferrite system for application at lower microwave frequencies", *J. Appl. Phys.*, Vol. 32, pp. 3905-3915, 1961.

[5]   West, R. G. and Blankenship, A. C., "Magnetic properties of dense lithium ferrites", *J. Am. Ceram. Soc.*, Vol. 50, pp. 343-349, 1967.

[6]   Baba, P. D. and Banerjee, S. K., "Microwave ferrite program", Summary Technical Report, ESD-TR-68-251, 1968.

[7]   Collins, T. and Brown, A. E., "Low-loss lithium ferrites for microwave latching applications", *J. Appl. Phys.,* Vol. 42, pp. 3451-3454, 1971.

[8]   Pointon, A. J. and Saull, R. C., "Solid-state reactions in lithium ferrites", *J. Am. Ceram. Soc.*, Vol. 52, pp. 157-160, 1969.

[9]   Ridgley, D. H., Lessoff, H., and Childress, J. D., "Effects of lithium and oxygen losses on magnetic and crystallographic properties of spinel lithium ferrite", *J. Am. Ceram. Soc.*, Vol. 53, pp. 304 - 311, 1970.

[10]   Argentina, G. M., and Baba, P. D., "Microwave Lithium Ferrites: An Overview", *IEEE T MICROW THEORY*, Vol. MTT-22, No. 6, pp. 652-658, 1974.

[11]   Bhatu, S. S., Lakhani, V. K., Tanna, A. R., Vasoya, N. H., Buch, J. U., Sharma, P. U., Trivedi, U. N., Joshi, H. H. and Modi, K. B., "Effect of nickel substitution on structural, infrared and elastic properties of lithium ferrite", *Indian J. Pure & Appl. Phys.*, Vol. 45, pp. 597-608, 2007.

[12]   S. Akther and M. A. Hakim, "Magnetic properties of cadmium substituted lithium ferrites", *Mater. Chem. Phys*. Vol. 120, pp. 399-403, 2010.

[13]   Soibam, Ibetombi, Phanjoubam, Sumitra, Prakash, Chandra, "Mössbauer and magnetic studies of cobalt substituted lithium zinc ferrites prepared by citrate precursor method", *J. Alloys Compd.*, Vol. 475, pp. 328–331, 2009.

[14]   Widatallah, H. M., Johnson, C., Gismelseed, A. M., Al-Omari, I. A., Stewart, S. J., Al-Harthi, S. H., Thomas, S. and Sitepu, H., "Structural and magnetic studies of nanocrystalline Mg-doped

$Li_{0.5}Fe_{2.5}O_4$ particles prepared by mechanical milling", *J. Phys. D: Appl. Phys.*, Vol. 41, pp. 165006(1) -165006(10), 2008.

[15]   Tasaki, J. and Ito, T., "Effect of Sintering Atmosphere on the permeability of Sintered Ferrites", Ferrites: proceedings of the International. Conference on Ferrites, Japan, pp.84-86, 1970.

[16]   Nakamura, T., "Low-temperature sintering of Ni-Zn-Cu ferrite and its permeability spectra", *J. Magn. Magn. Mater.*, Vol. 168, pp. 285-291, 1997.

[17]   Roess, E., *Ferrites*, University of Tokyo Press, Tokyo, pp.187, 1971.

[18]   Leung, L. K., Evans, B. J. and Morrish, A. H., "Low-temperature Mössbauer study of a nickel-zinc ferrite: $Zn_{1-x}Ni_xFe_2O_4$", *Phys. Rev. B.*, Vol. 8, pp. 29-43, 1973.

[19]   Rezlescu, N., Rezlescu, E., Pasnicu, C. and Craus, M. L., "Effects of the rare-earth ions on some properties of a Nickel-Zinc ferrite", *J. Phys: Condens. Matter*, Vol. **6**, pp. 5707- 5716, 1994.

[20]   E. Rezlescu, L. Sachelarie, P. D. Popa and N. Rezlescu, "Effect of substitution of diavalent ions on the electrical and magnetic properties of Ni-Zn-Me ferrites", *IEEE Trans. Magn.*, Vol. 36, pp. 3962-3967, 2000.

[21]   Globus, A., "2nd EFS Conf. on Soft Magnetic Material", Wolfson Center for Magnetic Technology, Cardiff, Wales, 1975.

[22]   El-Shabasy, M., "DC electrical properties of Ni-Zn ferrites", *J. Magn. Magn. Mater.*, Vol. 172, pp. 188-192, 1997.

[23]   Wahab, M. A., *Solid State Physics-Structure and properties of materials*, Narosa publishing house, New Delhi, 1999.

[24]   Chikazumi, S., *Physics of Magnetism*, John Wiley & Sons, Inc., New York, 1966.

[25]   Brailsford, F., *Physical Principles of Magnetism*, D. Van Nostrand Company Ltd., London, 1966.

[26]   Dekker, A. J., *Solid State Physics*, Macmillan India Ltd., New Delhi, 1998.

[27]   Cullity, B. D., *Introduction to Magnetic Materials*, Addison-Wiley Publishing Company, Inc., California, 1972.

[28]   Goldman, Alex, *Modern Ferrite Technology*, 2nd Ed, Springer Science-Business Media, Inc, Pittsburgh, PA, USA, 2006.

[29]   Smit, J. and Wijn, H. P. J., *Ferrites*, John Wiley and Sons, New York, pp. l49, 1959.

[30] Kittel, C., *Introduction to Solid State Physics*, 7th edition, John Wiley & Sons, Inc., Singapore, 1996.

[31] Jadhav, S. A., "Magnetic properties of Zn-substituted Li-Cu ferrites", *J. Magn. Magn. Mater.*, Vol. 224, pp. 167- 172, 2001.

[32] Hossain, A. K. M. A., Seki, M., Kawai, T. and Tabata, H., "Colossal magnetoresistance in spinel type $Zn_{1-x}Ni_xFe_2O_4$", *J. Appl. Phys.*, Vol. 96, pp. 1273-1275, 2004.

[33] Yafet, Y. and Kittel, C., "Antiferromagnetic arrangements in ferrites", *Phys. Rev.*, Vol. 87, pp. 290-294, 1952.

[34] Hadfield, D., *Permanent Magnets and Magnetism*, John Wiley & Sons, Inc., New York, 1962.

[35] Sikder, S. S., "Temperature dependence of magnetization and induced magnetic anisotropy of some Fe, Co and Ni-based amorphous ribbons", Ph. D. Thesis, BUET, Bangladesh, 1999.

[36] Snoek, J. L., "Dispersion and absorption in magnetic ferrites at frequencies above one Mc/s", *Physica*, Vol. 14, pp. 207-217, 1948.

[37] Irvine, J. T. S., West, A. R., Amano, E., Huanosta, A. & Valenzuela, R., "Characterization of magnetic materials by impedance spectroscopy", *Solid State Ionics*, Vol. 40-41, pp. 220-223, 1990.

[38] Globus, A. & Duplex, P., "Separation of susceptibility mechanisms for ferrites of low anisotropy", *IEEE Trans. Magn.*, Vol. 2, pp. 441-445, 1966.

[39] Chickazumi, S. and Charap, S. H., *Physics of Magnetism*, Krieger Pub. Co., p. 248, 1978.

[40] Alan, H., Morrish, *The Physical Properties of Magnetism*, John Wiley and Sons, 1966.

[41] Yan, M. F. and Johnson, D. W., "Impurity induced exaggerated grain growth in Mn-Zn ferrites", *J. Am. Ceram. Soc.*, Vol. 61, pp. 342-349, 1978.

[42] Hastings, J. M. and Corliss, L. M., "Neutron Diffraction Studies of Zinc Ferrite and Nickel Ferrite", *Rev. Mod. Phys.*, Vol. 25, pp. 114-119, 1953.

[43] Chen, Qi, Rondinone, Adam J., Chakoumakos, Bryan C., and Zhang, Z. John, "Synthesis of superparamagnetic $MgFe_2O_4$ nanoparticles by coprecipitationa", *J. Magn. Magn. Mater.,* Vol. 194, pp. 1-7, 1999.

CHAPTER 3

SAMPLE FABRICATION, CHARACTERIZATION AND

EXPERIMENTAL TECHNIQUES

3.1 Composition of the studied ferrites

In the present research Li-Ni-Zn based soft ferrites are synthesized and thoroughly investigated. The ferrites under investigation are:

$Li_{0.35-0.5x}Ni_{0.3}Zn_xFe_{2.35-0.5x}O_4$ (x = 0.00, 0.10, 0.20, 0.30 and 0.40)
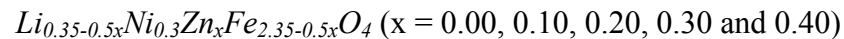
3.2 Sample preparation

The preparation of polycrystalline ferrites with optimum desired properties is still complex and sophisticated task. Knowledge and control of the chemical position, homogeneity and microstructure are very crux. As the most of the properties needed for ferrites applications are not intrinsic but extrinsic, preparation of samples has to encounter added complexity. Many processing methods have been proposed but are mainly divided into two groups;

1. Conventional ceramic method, i.e., solid state reaction technique, involves milling of the reactants followed by heating at elevated temperatures range.

2. Non conventional method also called wet method. Among these methods, some are [1, 2]:

   ➢ Sol-gel synthesis

   ➢ Co-precipitation

   ➢ Combustion synthesis

In this chapter, we prepared our sample by sol gel auto combustion synthesis method.

3.3 Sol-gel auto combustion synthesis

Sol-gel auto Combustion synthesis, also called self-propagating synthesis, was initially developed in Russia by Merhanov [3]. Sol-gel auto Combustion method a novel method for preparation of fine particles of ferrites makes use of the strong exothermic reaction between metal nitrate and fuel.

The advantages of sol gel auto combustion method include:

❖ Good chemical homogeneity;

❖ High product purity and crystallinity;

❖ Low processing time;

❖ Multiple steps are not involved;

❖ Simple equipment and preparation process;

3.3.1 Percentage measurement of materials

At first we calculate the molecular weight of $Li_{0.35-0.5x}Ni_{0.3}Zn_xFe_{2.35-0.5x}O_4$

Table 3.1 List of the molecular weight samples.

Specimen	Weight % of $Zn(NO_3)_2.6H_2O$ (g)	Weight % of $LiNO_3$ (g)	Weight % of $Ni(NO_3)_2.6H_2O$ (g)	Weight % of $Fe(NO_3)_3.9H_2O$ (g)	Weight% of citric acid (g)
$Li_{0.35}Ni_{0.3}Fe_{2.35}O_4$	0.00	1.6814	6.0787	66.1534	31.6219
$Li_{0.3}Ni_{0.3}Zn_{0.1}Fe_{2.3}O_4$	2.0406	1.4188	5.9842	63.7396	31.8299
$Li_{0.25}Ni_{0.3}Zn_{0.2}Fe_{2.25}O_4$	4.0187	1.1642	5.8926	61.3996	32.0314
$Li_{0.2}Ni_{0.3}Zn_{0.3}Fe_{2.2}O_4$	5.9373	0.9173	5.8038	59.1302	32.2269
$Li_{0.15}Ni_{0.3}Zn_{0.4}Fe_{2.15}O_4$	7.7988	0.6778	5.7176	56.9282	32.4166

3.3.2 Synthesis of nanocrystalline powder

The nominal compositions were prepared by sol gel auto combustion technique. In this processes, Stoichiometric amounts of $LiNO_3$, $Zn(NO_3)_2.6H_2O$, $Ni(NO_3)_2.6H_2O$, $Fe(NO_3)_3.9H_2O$ and citric acid were used as raw materials. The appropriate amount of nitrates and citric acid were first dissolved into distilled water to form a solution. The molar ratio of metals to citric acid was 1:3. The P^H value of solution was adjusted to about 7 by using ammonia solution. Then, the mixed solution was poured into a beaker and heated at 90ºC for several hours. During the procedure, the solution was continuously stirred using a magnetic stirrer. After stirring, firstly the solution was converted into gel form and then gradually was become dense gel form. Finally, the gel form was converted into fluffy nano-sized loose powder ensuring the automatic combustion. Then the fine powders are granulated using polyvinyl alcohol (PVA) as a binder and pressed into disk- and toroid-shaped samples. The samples are sintered at various temperatures (1100, 1150, 1200, 1250 and 1300ºC) for 5 hour. The temperature ramps for sintering are 10ºC/min for heating, and 5ºC/min for cooling. [4-7].

Lithium Nitrate	Nickel Nitrate	Zinc Nitrate	Ferric Nitrate	Citric acid

Citric Nitrate solution

P^H maintained at 7 by using Ammonia solution

Sol

Gel

Dry Gel

Auto-Combustion

Burnt Ash

Grinding

Li-Ni-Zn Ferrite powder

Sintering

Finish product

Characterization:

- Structural
- Magnetic
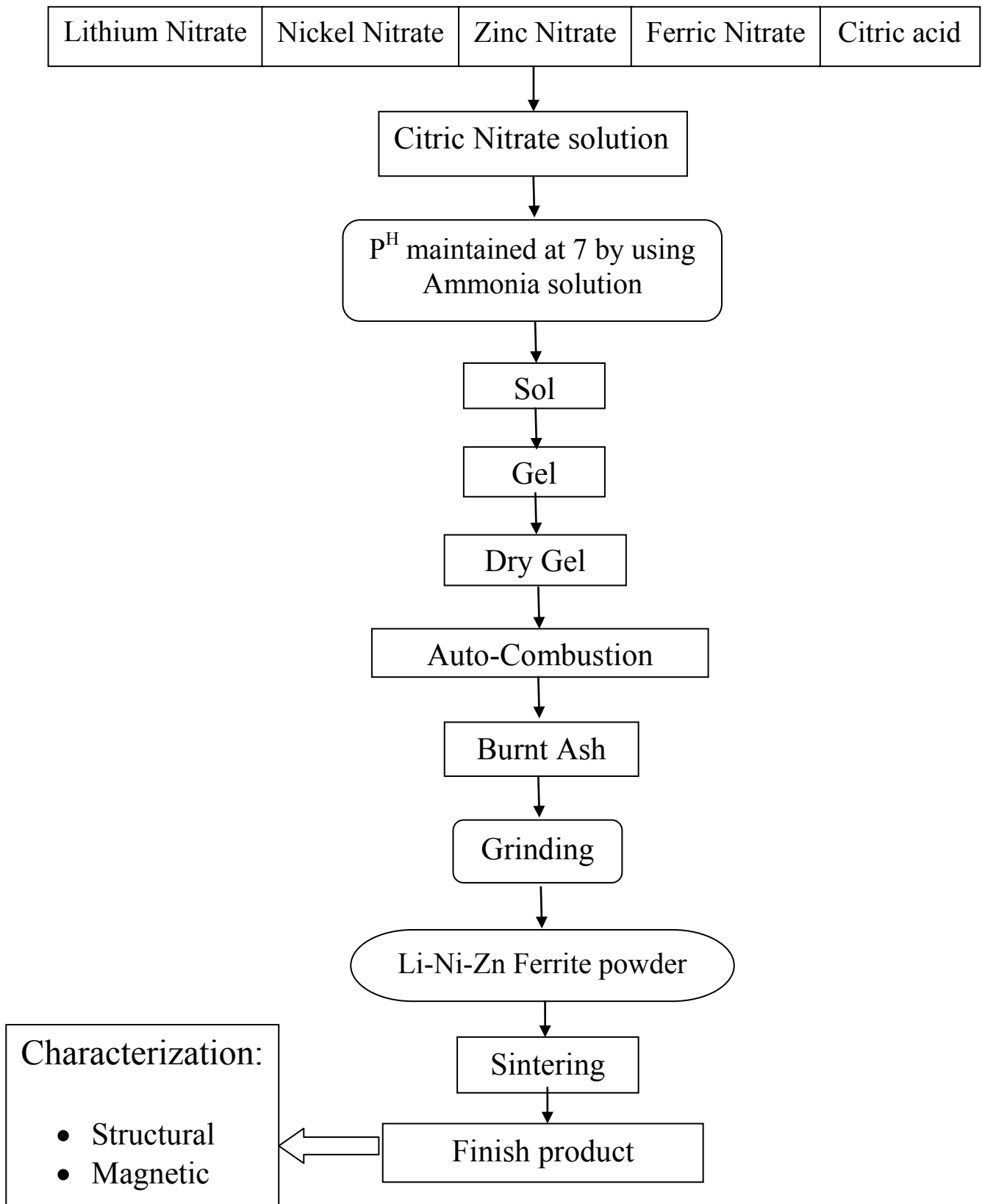
Fig. 3.1 Flow diagram for sol-gel auto combustion synthesis of Li-Ni-Zn ferrite powder.

Fig. 3.2 Sample (a) disk shaped, (b) toroid shaped.

3.3.3 Sample image

Samples, weight, diameter, pressure and purpose of ferrites.

Table 3.2 List of the purpose for various shape samples.

Name	Weight (g)	Shape	Image	Pressure (psi)	Purpose
Toroid	0.70	Ring		8000 psi	Néel Temperature, Permeability
Tablet	0.90	Pellet		8000 psi	SEM EDX
Tablet	1.5	Powder		-	XRD
Tablet	0.013	Powder		-	VSM

3.4 Details of pressing and sintering

Pressing or extrusion and sintering are the mechanisms used to form solid parts from powders. Pressing occurs first, then sintering. Before pressing, the powder is fully prepared as explained in the powder metallurgy section. In addition to the powder constituents, binders, deflocculates and lubricants may also be present in the mixture. A

61

binder is usually added prior to compaction, at a concentration lower than 5wt % [2]. Binders are polymers or waxes; the most commonly used binder in ferrite is polyvinyl alcohol. The binder facilitates the particles flow during compacting and increases the bonding between the particles, presumably by forming bonds of the type particle-binder-particle. During sintering, binders decompose and are eliminated from the ferrite. Pressures are used for compacting very widely but are commonly several tons per square inch (i. e., up to $10^8 \, N \, m^{-2}$).

Sintering is defined as the process of obtaining a dense, tough body by heating a compacted powder for a certain time at a temperature high enough to significantly promote diffusion, but clearly lower than the melting point of the main component. The driving force for sintering is the reduction in surface free energy of the powder. Part of this energy is transferred into interfacial energy (grain boundaries) in the resulting polycrystalline body [2, 9]. The sintering time, temperature and the furnace atmosphere play very important role on the magnetic property of ferrite materials. The purposes of sintering process are:

1) to bind the particles together so as to impart sufficient strength to the product,

2) to densify the material by eliminating the pores and

3) to homogenize the materials by completing the reactions left unfinished in the calcining step.

Sintering of crystalline solids is dealt by Coble and Burke [10] who found the following empirical relationship regarding rate of grain growth:

$$\bar{d} = kt^n$$

where $\bar{d}$ is the mean grain diameter, n is about 1/3, t is sintering time and k is a temperature dependent parameter. Sintering is divided into three stages, Fig. 3.3 [2, 11].

Stage 1. Contact area between particles increases,

Stage 2. Porosity changes from open to closed porosity,

Stage 3. Pore volume decreases; grains grow.
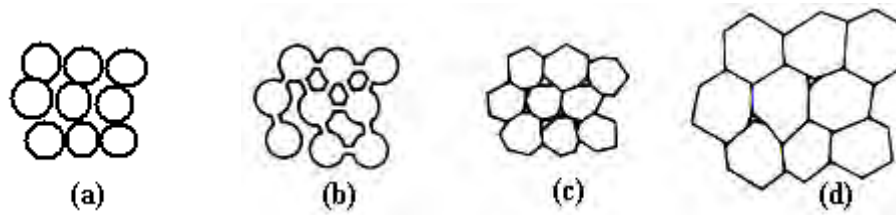
Fig. 3.3 Schematic representation of sintering stages: (a) greenbody, (b) initial stage, (c) intermediate stage, and (d) final stage.

In the initial stage, neighbouring particles form a neck by surface diffusion and presumably also at high temperatures by an evaporation-condensation mechanism. Grain growth begins during the intermediate stage of sintering. Since grain boundaries are the sinks for vacancies, grain growth tends to decrease the pore elimination rate due to the increase in distance between pores and grain boundaries, and by decreasing the total grain boundary surface area. In the final stage, the grain growth is considerably enhanced and the remaining pores may become isolated.

In *Li-Ni-Zn* ferrites, the presence of *Li* complicates the sintering process because high temperature coupled with low oxygen firing will cause *Li* loss. High density is important for high permeability, but so is *Li* conservation. Tasaki [1] described two alternative firings to achieve high density:

1) Low sintering temperature excluding O_2 (Vacuum, argon, nitrogen),

2) High temperature in pure oxygen to reduce *Li* loss.

Accordingly, other properties correlated along with density:

1) Lattice constant is greater for O_2, smaller for vacuum

2) Curie temperature is greater for vacuum, smaller for O_2

3) Resistivity is greater for O_2, smaller for vacuum.

3.5 X-ray diffraction

X-ray like other electromagnetic waves interact with the electron cloud of the atoms. Because of their shorter wavelengths, X-ray are scattered by adjacent atoms in crystal which can interfere and gives rise to diffraction effects. Bragg reflection is a coherent elastic scattering in which the energy of the X-ray is not changed on reflection. Let a beam of monochromatic radiation of wavelength λ is incident on a periodic crystal plane at an angle θ and is diffracted at the same angle as shown in Fig. 3.4. When constructive interference occurs, from Fig 3.4 (a) it can be written as,

$$n\lambda = AB + BC$$

As, $AB=BC$, $n\lambda = 2AB$

Again from Fig 3.4(b), $sin\theta=AB/d$

So, $AB=d\ sin\theta$

i.e. $2d\ Sin\theta=n\lambda$ (3.1)

where d is the distance between crystal planes and n is the positive integer which represents the order of reflection. Equation (3.1) is known as Bragg law. This Bragg law suggests that the diffraction is only possible when $\lambda \leq 2d$. For this reason we cannot use the visible light to determine the crystal structure of a material. The X-ray diffraction (XRD) provides substantial information on the crystal structure.
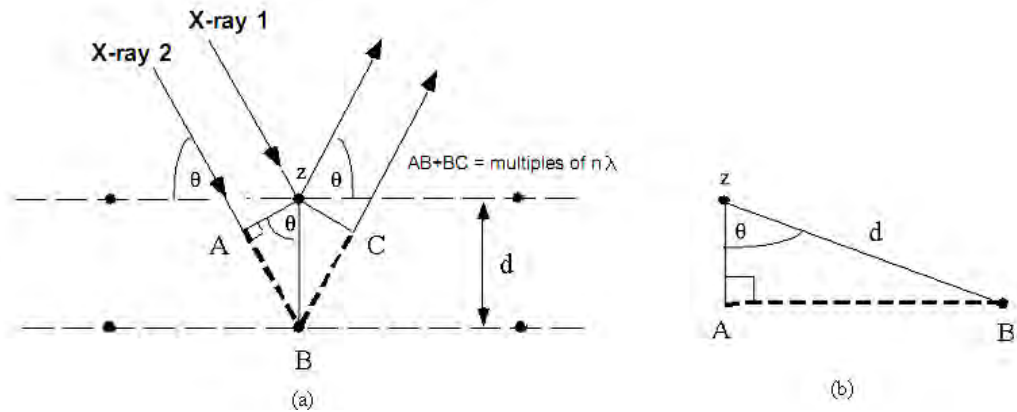
Fig. 3.4 Bragg law of diffraction.

X-ray diffraction was carried out using an advanced X-ray diffractometer model- Philips PANalytical X'PERT-PRO (Cu-K$_\alpha$ as a target and incident wavelength λ= 1.540598 Å radiation). Basic features of a XRD experiments is shown in Fig. 3.5 respectively.
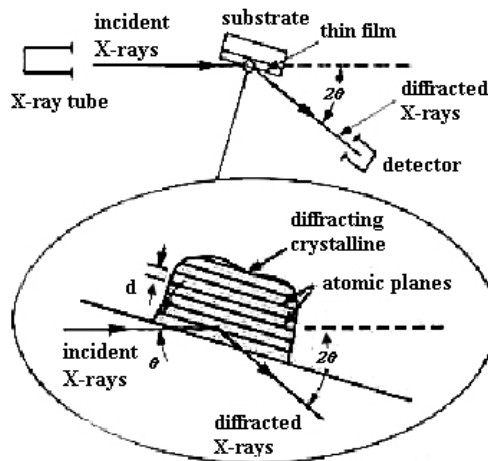
Fig. 3.5 Basic features of typical XRD experiment.

The lattice parameter for each peak of each sample was calculated by using the formula

$$a=d\sqrt{h^2+k^2+l^2} \tag{3.2}$$

where *h*, *k* and *l* are the indices of the crystal planes. To determine the precise lattice constant for each sample, Nelson-Riley method was used. The Nelson-Riley function *F(θ)* is given as

$$F(\theta) = \frac{1}{2}\left[\left(\frac{Cos^2\theta}{Sin\theta}\right) + \left(\frac{Cos^2\theta}{\theta}\right)\right]$$ (3.3)

The values of lattice parameter '*a*' of all the peaks for a sample are plotted against $F(\theta)$. Then using a least square fit method exact lattice constant 'a_o' is determined. The point where the least square fit straight line cut the y-axis (i.e. at $F(\theta) =$ 0) is the actual lattice constant of the sample. The theoretical density ρ_{th} was calculated using following expression:

$$\rho_{th} = \frac{8M}{N_A\, a_o^3}\, g/cm^3$$ (3.4)

where N_A is Avogadro's number (6.02×10^{23} mol^{-1}), M is the molecular weight. The porosity was calculated from the relation {$100(\rho_{th} - \rho_B)/\ \rho_{th}$} %, where ρ_B is the bulk density measured by the formula $\rho_B = M/V$.

3.6 Microstructural investigation

The microstructural study was performed in order to have an insight of the grain structures. The samples of different compositions and sintered at different temperatures were chosen for this purpose. The scanning electron microscope (SEM) is a type of electron microscope that images the sample surface by scanning it with a high energy beam of electrons in a raster scan pattern. The electrons interact with the atoms that make up the sample producing signals that contain information about the sample's topography. Average grain sizes (grain diameter) of the samples were determined from SEM by linear intercept technique [4]. To do this, several random horizontal and vertical lines were drawn on the micrographs. Therefore, we counted the number of

grains intersected and measured the length of the grains along the line traversed. Finally the average grain size was calculated.

3.7 Energy dispersive X-ray spectroscopy

Energy dispersive X-ray spectroscopy (EDX) is an analytical technique used for the elemental analysis or chemical characterization of a sample. It is one of the variants of X-ray fluorescence spectroscopy, which relies on the investigation of a sample through interactions between electromagnetic radiation and matter, analyzing X-rays that are characteristics of an element's atomic structure to be identified uniquely from one another. An EDX system is comprised of three basic components, the X-ray detector, the pulse processor, and the analyzer, that must be designed to work together to achieve optimum results. In practice, the X-ray detector first detects and converts X-rays into electronic signals. Then, the pulse processor measures the electronic signals to determine the energy of each X-ray detected. Finally, the analyzer displays and interprets the X-ray data. In the present work, compositional analyses are performed by using the EDX system supplied with the JEOL JSM 7600F.

3.8 Complex permeability measurement

For high frequency application, the desirable property of a ferrite is high permeability with low loss. One of the most important goals of ferrite research is to fulfill this requirement. The techniques of permeability measurement and frequency characteristics of the present samples are described in sections 3.8.1 and 3.8.2.

3.8.1 Techniques for the permeability measurement

Measurements of permeability normally involve the measurements of the change in self-inductance of a coil in presence of the magnetic core. The behaviour of a self-inductance can now be described as follows. We assume an ideal loss less air coil of inductance L_0. On insertion of a magnetic core with permeability μ, the inductance will be μL_0. The complex impedance Z of this coil [1] can be expressed as follows:

$$Z = R + jX = j\omega L_0 \mu = j\omega L_0 (\mu^/ - j\mu^{//}) \tag{3.5}$$

where the resistive part is $\qquad\qquad R = \omega L_0 \mu^{//} \tag{3.6}$

and the reactive part is $\qquad\qquad X = \omega L_0 \mu^/ \tag{3.7}$

The RF permeability can be derived from the complex impedance of a coil, Z, given by equation (3.5). The core is taken as toroidal to avoid demagnetizing effects. The quantity L_o is derived geometrically as shown in section 3.8.2.

3.8.2 Frequency characteristics of the present samples

The frequency characteristics of the ferrite samples i.e. the initial permeability spectra were investigated using Wayne Kerr Impedance Analyzer (model no. 6500B). The complex permeability measurements on toroid shaped specimens were carried out at room temperature on all the samples in the frequency range 100 *Hz* - 120 *MHz*. The real part $(\mu_i^/)$ and imaginary part $(\mu_i^{//})$ of the complex permeability were calculated using the following relations [5]: $\mu_i^/ = \dfrac{L_s}{L_0}$ and $\mu_i^{//} = \mu_i^/ \tan\delta$, where L_s is the self-inductance of the sample core and $L_0 = \dfrac{\mu_o N^2 S}{\pi \bar{d}}$ is derived geometrically. Here L_o is the

inductance of the winding coil without the sample core, N is the number of turns of the coil ($N = 4$), S is the area of cross section of the toroidal sample as given below:

$$S = d \times h,$$

where $\qquad d = \dfrac{d_2 - d_1}{2},$

$\qquad\qquad d_1 = $ Inner diameter,

$\qquad\qquad d_2 = $ Outer diameter,

$\qquad\qquad h = $ Height

and $\bar{d}$ is the mean diameter of the toroidal sample as given below:

$$\bar{d} = \dfrac{d_1 + d_2}{2}$$

The relative quality factor is determined from the ratio $\dfrac{\mu_i^/}{\tan \delta}$.

3.9 Néel Temperature measurements

Néel temperature measurement is one of the most important measurements for magnetic materials. Néel temperature provides substantial information on magnetic status of the material with respect to the strength of exchange interaction. So the determination of Néel temperature accurately is of great importance. Our Néel temperature measurements involved the measurement of permeability with varying the temperature. The temperature dependent permeability was measured by using an impedance analyzer and a tubular furnace. The specimen formed the core of a coil. By varying temperature, permeability of the substance as a function of temperature was measured. When the magnetic state of the sample changes from antiferromagnetic to paramagnetic, the permeability falls sharply. This is the basic principle used in our

experimental setup. The real part of permeability was measured by using impedance analyzer. The permeability is calculated using the following formula:

$$\mu' = L_s/L_0 \qquad (3.8)$$

where L_s is the self-inductance of the sample core and

$$L_0 = \frac{\mu_0 N^2 m}{\pi^2 \rho \bar{d}^2} \qquad (3.9)$$

Where L_0 is the inductance of the winding coil without the sample core and N is the number of turns of coil (here N=4), m is the mass of the sample and $\bar{d}$ is the mean diameter of the toroid as follows:

$$\bar{d} = \frac{d_1 + d_2}{2} \qquad (3.10)$$

where d_1 and d_2 are the inner and outer diameter of the toroidal sample.

At first we wind wires in the toroidal sample and then the sample is kept close to thermocouple. The thermocouple measures the temperature inside over and also the sample. The sample is kept just in the middle part of the cylindrical over so that the temperature gradient is minimized. The temperature of the oven is then raised slowly. If the heating rate is very fast then temperature of the sample may not follow the temperature inside the oven and there can be misleading information on the temperature of sample. The thermocouple showing the temperature in that case will be erroneous. Due to the closed winding of wires the sample may not receive the heat at once. So, a slow heating rate is used to eliminate this problem. Also a slow heating ensures accuracy in the determination of Néel temperature. The oven is kept thermally insulated from the surroundings.

3.10 DC magnetization measurement at room temperature

The DC magnetization (M) was measured at room temperature using the vibrating sample magnetometer (Model-EV9) in the presence magnetic field ranges from 0.0 to 1T. Diameter of the sample was made as it fit to the sample rod finely. In VSM the sample is vibrated at 82 Hz frequency and magnetization strength is found from the magnitude of the emf induce in the sense coils placed in proximity with sample. The block diagram of the VSM is shown in Fig. 3.6
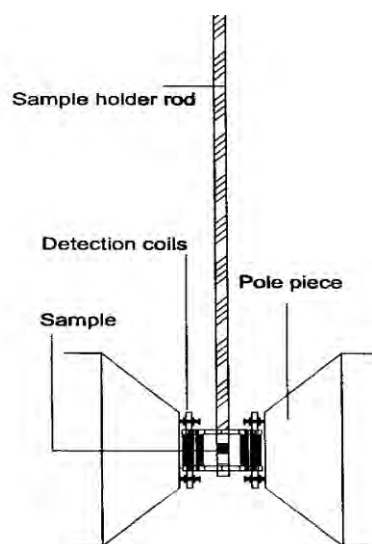
Fig. 3.6 Block diagram of vibrating sample magnetometer (VSM).

The pickup coils are mounted with axis perpendicular to magnetization field so as to minimize error signals arising from field fluctuations. Magnetization values of all samples were recorded by setting up the magnet at a maximum applied field. For the calculation of saturation magnetization, the values are obtained in milivolts (mV), these values are then calibrated in emu using nickel standard of value $1mV = 2.7 \times 10^{-4}$ emu. The calculated values are then divided by mass of the respective sample to obtain the values in emu/g for each sample.

71

3.11 Equipment needed for sample preparation and characterization

The equipment needed to prepare $Li_{0.35-0.5x}Ni_{0.3}Zn_xFe_{2.35-0.5x}O_4$ are balance, beakers, P^H meter, magnetic stirrer, mortar and pestle, crucibles, furnace, dies, hydraulic press, Wayne Kerr Impedance Analyzer (model no. 6500B). All these instruments are available at solid state physics lab, dept. of physics, BUET, Dhaka-1000, Bangladesh. The SEM and EDX measurement are taken on dept. of Glass and Ceramic Engineering, BUET, Dhaka-1000, Bangladesh. The DC magnetization measurement are taken on Atomic Energy Center, Dhaka.

Fig. 3.7 Balance, morter and pastle.

Fig. 3.8 Beakers, P^H meter and magnetic stirrer.

Fig. 3.9 Hydraulic press and nabertherm furnace maximum temperature 30°C ~ 3000.

Fig. 3.10 Wayne Kerr impedance analyzer (model no. 6500B).

Fig. 3.11 FESEM and EDX system.
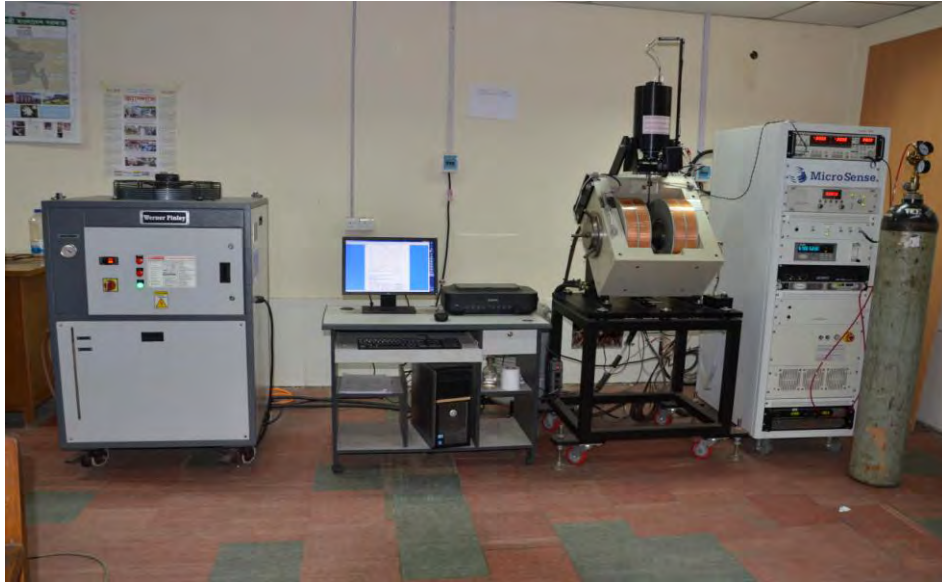
Fig. 3.12 EV9 vibrating sample magnetometer (VSM).

References

[1]   Goldman, A., *Handbook of Modern Ferromagnetic Materials*, Kulwer Acad. Pub, Boston, U.S.A, 1999.

[2]   Valenzuela, R., *Magnetic Ceramics*, Cambridge University Press, Cambridge, 1994.

[3]   Merzhanov, A. G., Shkiro, V. M. and Borovinskaya, I. P., "Synthesis of refractory inorganic compounds", *Izvest. Bull*., Vol. 10, pp. 1-11, 1971.

[4]   Hossain, A. K. M. A., "Investigation of colossal magnetoresistance in bulk and thick film magnetites", Ph. D. Thesis, Imperial College, London, 1998.

[5]   Cullity, B. D., *Introduction to Magnetic Materials*, Addison-Wisley Publishing Company, Inc., California, 1972.

[6]   Brook, R. J., *Sintering: An Overview*, *Concise Encyclopedia of Advanced Ceramic Materials*, Pergamon Press, Oxford, 1991.

[7]   Reijnen, P., *Science of Ceramics*, Academic Press, London, 1967.

[8]   Slick, P. I., *Ferrites for Non-microwave Applications*, North Holland Pub. Co., 1980.

[9]   Kingery, W. D., Bowen, H. K. and Uhlman, D. R., *Introduction to Ceramics*, 2nd edition, Wiley Interscience, New York, 1976.

[10]   Coble, R. L. and Burke, J. E., "On the Reactivity of Solids", 4th Int. Symp., 30 May-4 June, Amsterdam, pp. 38-51, 1960.

[11]   McColm, I. J. and Clark, N. J., *Forming, Shaping and Working of high Performance Ceramics*, Blackie, Glasgow, pp. 1-345, 1988.

CHAPTER 4

RESULTS AND DISCUSSION

The structural and magnetic properties of $Li_{0.35-0.5x}Ni_{0.3}Zn_xFe_{2.35-0.5x}O_4$ (x = 0.00, 0.10, 0.20, 0.30 and 0.40) are studied. All ferrite samples are sintered at temperatures 1100, 1150, 1200, 1250 and 1300ºC for five hours. Structural and surface morphology are studied by X-ray diffraction (XRD) and Field Emission Scanning Electron Microscope (FESEM), respectively. From the energy-dispersive X-ray spectroscopy study it is observed that the percentage of the elements in the component phases is well consistent with the nominal composition. The magnetic properties of the ferrites are characterized by high frequency (100 Hz-120 MHz) complex permeability. The frequency dependent initial permeability at room temperature of the samples is also studied. The effects of varying Zn substitution and sintering temperature on the complex permeability of these ferrites are discussed. The temperature-dependent permeability and Néel temperature of the samples sintered at 1250ºC are also studied. DC magnetization of the various $Li_{0.35-0.5x}Ni_{0.3}Zn_xFe_{2.35-0.5x}O_4$ are also studied.

4.1 XRD analysis of various $Li_{0.35-0.5x}Ni_{0.3}Zn_xFe_{2.35-0.5x}O_4$

Fig. 4.1 shows the XRD patterns of various as grown powders. A slightly broader peak indicating nano-sized particles are formed for all compositions. The crystallite size for all compositions is evaluated using the (311) diffraction peak by the Scherer formula [2], as shown in Fig, 4.2. The calculated value of crystallite size is in the range 23 to 37 nm. The FESEM images of various as grown powders (as shown in Fig. 4.3) indicates that the nano-sized powders are spherical in shape and are uniformly distributed.
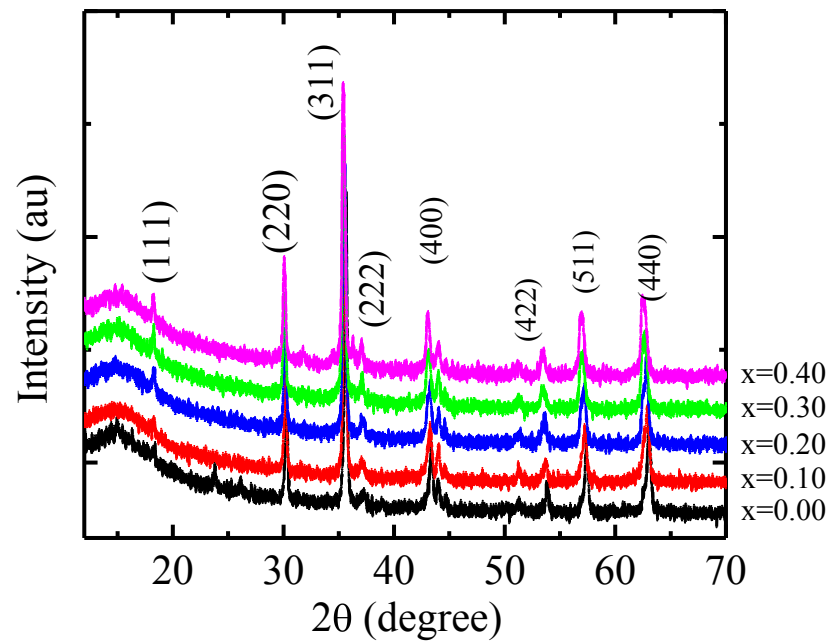
Fig. 4.1 The XRD patterns for various powder of $Li_{0.35-0.5x}Ni_{0.3}Zn_xFe_{2.35-0.5x}O_4$.
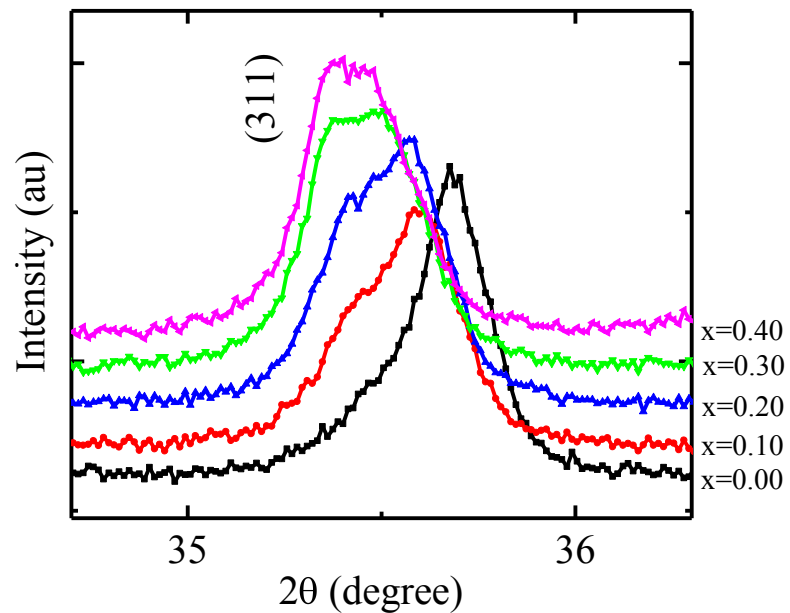
Fig. 4.2 The XRD patterns for various powder of $Li_{0.35-0.5x}Ni_{0.3}Zn_xFe_{2.35-0.5x}O_4$ with the (311) peak for crystallite size.
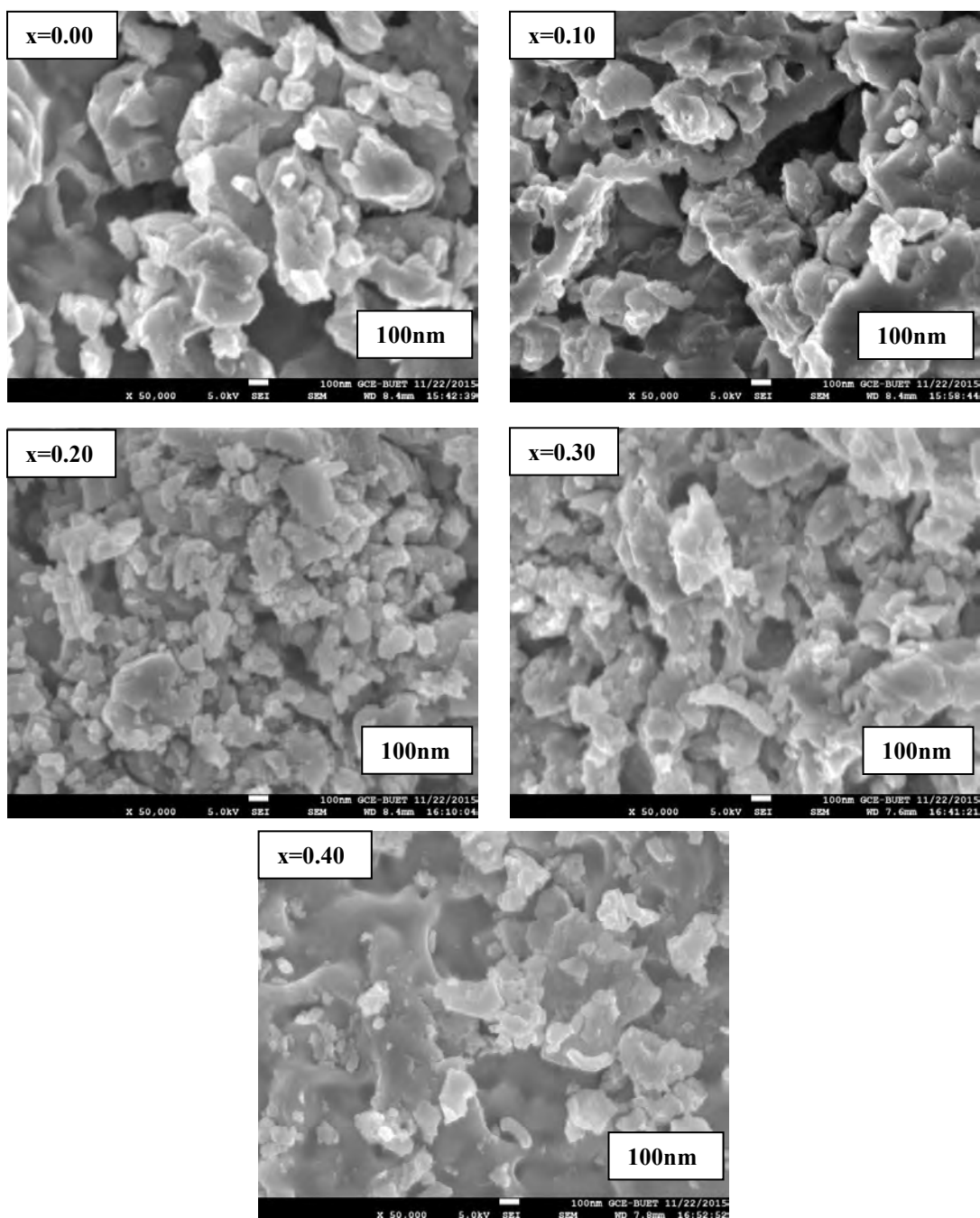
Fig. 4.3 The FESEM micrographs for various nanocrystalline powder of $Li_{0.35-0.5x}Ni_{0.3}Zn_xFe_{2.35-0.5x}O_4$.

Fig. 4.4 illustrates the XRD patterns of various $Li_{0.35-0.5x}Ni_{0.3}Zn_xFe_{2.35-0.5x}O_4$ sintered at 1250ºC. Sharp and well defined intense peaks observed, indexed as (111), (220), (311), (222), (400), (422), (511) and (440). The XRD pattern confirms that all compositions are

single phase cubic spinel structure having no impurity peak as all the peaks in pattern

matched well with characteristic reflections of earlier reported spinel ferrites [1].
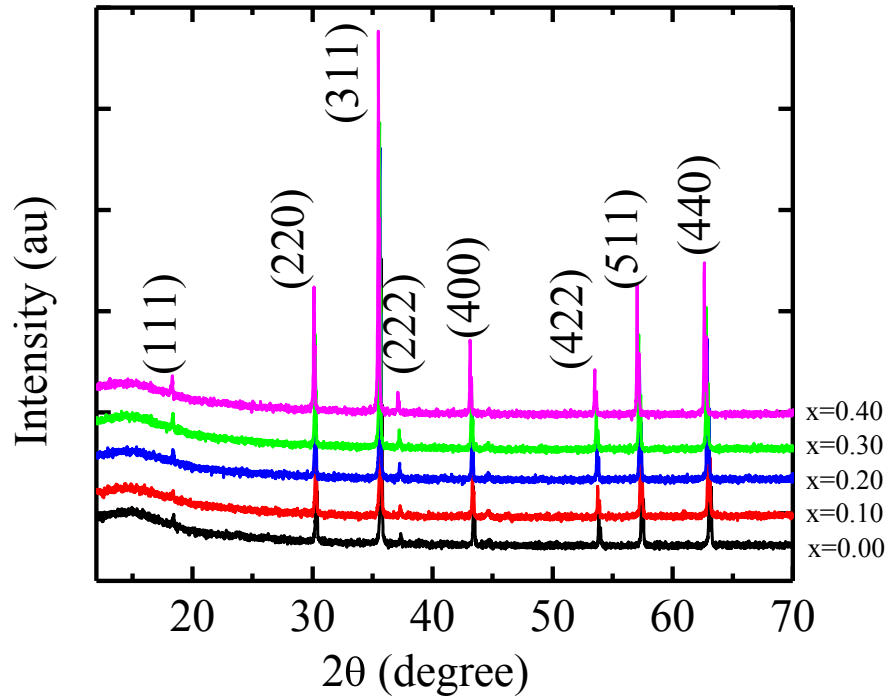
Fig. 4.4 The XRD patterns for various $Li_{0.35-0.5x}Ni_{0.3}Zn_xFe_{2.35-0.5x}O_4$ sintered at 1250ºC.

4.2 Lattice constant of various $Li_{0.35-0.5x}Ni_{0.3}Zn_xFe_{2.35-0.5x}O_4$

The lattice parameter is determined using the Nelson-Riley extrapolation

technique. The values of lattice parameter, obtained from each crystal plane are plotted

against Nelson-Riley (N-R) function [3] $F(\theta) = \frac{1}{2}\left[\frac{\cos^2\theta}{\sin\theta} + \frac{\cos^2\theta}{\theta}\right]$, where θ is the

Bragg's angle and a straight line is obtained. The accurate values of a_o are estimated

from the extrapolation of these lines to F(θ) = 0 or θ = 90ºC. The well matching fitting

of N-R function shows the good crystallinity of spinel phase as shown in Fig. 4.5(a).

The variation of a_o as a function of Zn content is shown in Fig. 4.5(b). It is noticed that

the a_o is found to increase from 8.3363 to 8.3840 Å with increasing Zn content in the

lattice. The lattice constant, density, porosity and average grain size for different compositions sintered at different sintering temperatures (T_s) are given in Table 4.1.
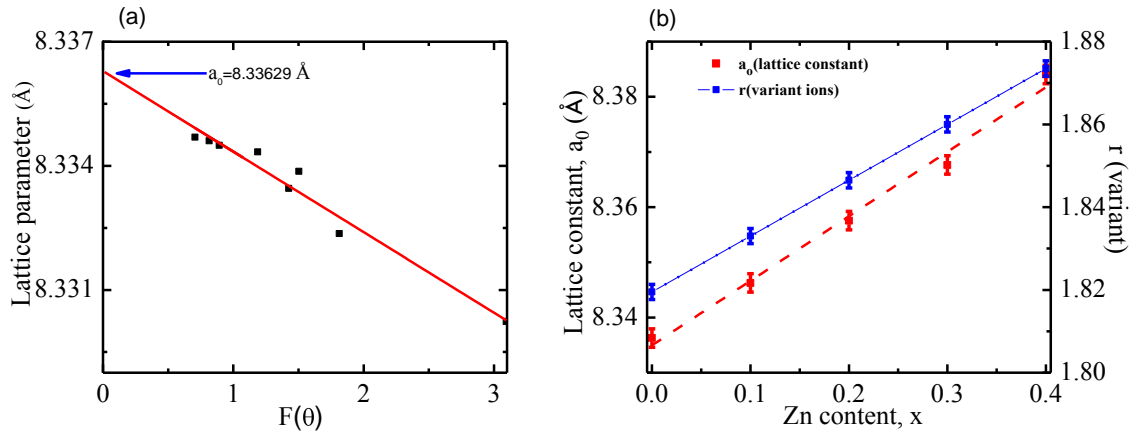
Fig. 4.5 (a) Variation of lattice parameter a with F(θ) and (b) Variation of the lattice constant a_o, and the mean ionic radius of the variant ion as a function of Zn content for $Li_{0.35-0.5x}Ni_{0.3}Zn_xFe_{2.35-0.5x}O_4$ sintered at 1250ºC.

It is clear from Fig. 4.5(b) that the lattice constant of all compositions follows Vegard's law, as shown by solid line. This increase of lattice constant with *Zn* contents can be explained on the basis of the ionic radii. The ionic radii of the cations used in various $Li_{0.35-0.5x}Ni_{0.3}Zn_xFe_{2.35-0.5x}O_4$ are 0.82 Å (Zn^{2+}), 0.70Å (Li^{1+}) and 0.67 Å (Fe^{3+}) [4]. Where 0.82 Å (Zn^{2+}) is replacing both 0.70Å (Li^{1+}) and 0.67 Å (Fe^{3+}) with their average radii 0.69 Å. Here Zn^{2+} is substituting by the both Li^{1+} and Fe^{3+} ion. So a small increase in lattice constant is expected, increasing *Zn* content. The compositions under investigation have the nominal chemical composition $Li_{0.35-0.5x}Ni_{0.3}Zn_xFe_{2.35-0.5x}O_4$.

Table 4.1 The lattice constant, density, porosity, average grain size, natural resonance frequency, maximum quality factor and initial permeability of the various $Li_{0.35-0.5x}Ni_{0.3}Zn_xFe_{2.35-0.5x}O_4$ sintered at various T_s with fixed dwell time 5h.

x	T_s (^oC)	a_o $(\AA)$	P_{th} (g/cm^3)	ρ_B (g/cm^3)	P $(\%)$	Average grain size (μm)	f_r (MHz)	Q_{max}	$\mu_i^/$ (at 1MHz)
0.00	1100	8.3362	4.94	3.73	24	-	-	3826	30
	1150			4.23	14	-	-	1838	34
	1200			4.29	13	-	-	2468	39
	1250			4.33	12	4.06	-	2415	40
	1300			4.32	12	-	-	1469	36
0.10	1100	8.3462	5.00	3.95	20	-	-	4386	35
	1150			4.25	14	-	-	2748	44
	1200			4.36	12	-	-	4388	57
	1250			4.39	12	4.23	120	5617	70
	1300			4.37	12	-	60	2836	65
0.20	1100	8.3575	5.10	4.09	18	-	-	4212	63
	1150			4.43	12	-	-	5068	78
	1200			4.61	8	-	60	6096	93
	1250			4.74	6	5.23	37	6994	116
	1300			4.51	10	-	34	6355	114
0.30	1100	8.3676	5.11	4.42	13	-	113	5297	87
	1150			4.53	11	-	81	7349	114
	1200			4.70	8	-	34	8680	144
	1250			4.85	5	5.95	25	9334	170
	1300			4.67	8	-	22	9888	167
0.40	1100	8.3840	5.16	4.57	11	1.77	90	7281	123
	1150			4.62	10	2.04	79	7238	126
	1200			4.76	7	2.90	22	11999	219
	1250			4.90	5	6.39	17	12395	250
	1300			4.79	7	10.52	15	11737	232

Therefore, the mean ionic radius of the variant ions for composition ($Li_{0.35-0.5x}Ni_{0.3}Zn_xFe_{2.35-0.5x}O_4$) can be written as

$$r_{(variant)} = x\, r_{Zn} + (0.35\text{-}0.5x)\, r_{Li} + (2.35\text{-}0.5x) r_{Fe} \tag{1}$$

Where, r_{Zn} is the ionic radius of Zn^{2+} ion (0.82 Å), r_{Li} is the radius of Li^{1+} ion (0.70 Å), and r_{Fe} is the ionic radius of Fe^{3+} ion (0.67 Å) [4]. The variation of $r_{(variant)}$ with Zn content is shown in Fig. 4.5(b), where it increases with increasing Zn content.

4.3 Density and porosity of various $Li_{0.35-0.5x}Ni_{0.3}Zn_xFe_{2.35-0.5x}O_4$

Theoretical density (ρ_{th}), bulk density (ρ_B) and porosity (P) of the various $Li_{0.35-0.5x}Ni_{0.3}Zn_xFe_{2.35-0.5x}O_4$ are tabulated in the Table 4.1. The ρ_{th}, increases with increasing a_o in the Zn substituted various $Li_{0.35-0.5x}Ni_{0.3}Zn_xFe_{2.35-0.5x}O_4$. It increases because the molecular weight of the each sample increases significantly with the addition Zn content. Both theoretical and bulk density increases in a similar fashion with the increase of Zn content in $Li_{0.35-0.5x}Ni_{0.3}Zn_xFe_{2.35-0.5x}O_4$ for a fixed sintering temperature, as shown in Fig. 4.6. The ρ_B of each composition reflects the same general behavior as that of the $\rho_{th.}$ The ρ_{th} is higher than the ρ_B. This may be due to the existence of pores in the sample, which depend upon the sintering conditions. Similar result were reported by Ajmal and Maqsood for Ni-Zn ferrite [5].

Fig. 4.7 indicates that as Zn content increases in $Li_{0.35-0.5x}Ni_{0.3}Zn_xFe_{2.35-0.5x}O_4$, density increases and P decreases. It is possible to explain this phenomenon in terms of the atomic weight. The atomic weight of Zn (65.38 amu) is greater than atomic weight of the Li (6.941 amu) and Fe (55.845 amu) [6].
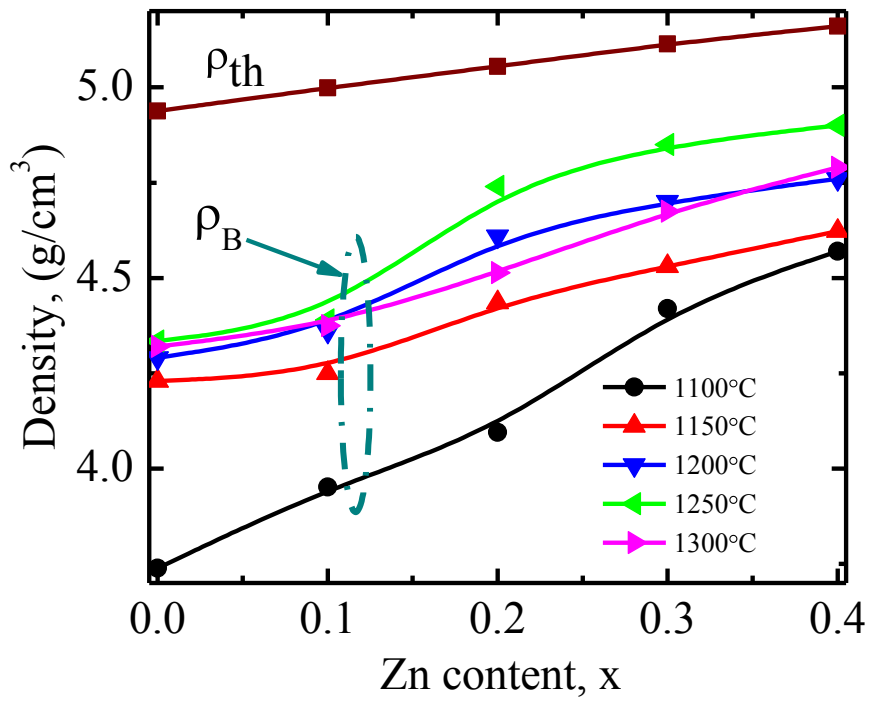
Fig. 4.6 The variation of theoretical density, ρ_{th}, and bulk density, ρ_B, for variation of *Zn* content in *$Li_{0.35-0.5x}Ni_{0.3}Zn_xFe_{2.35-0.5x}O_4$* sintered at various T_S.
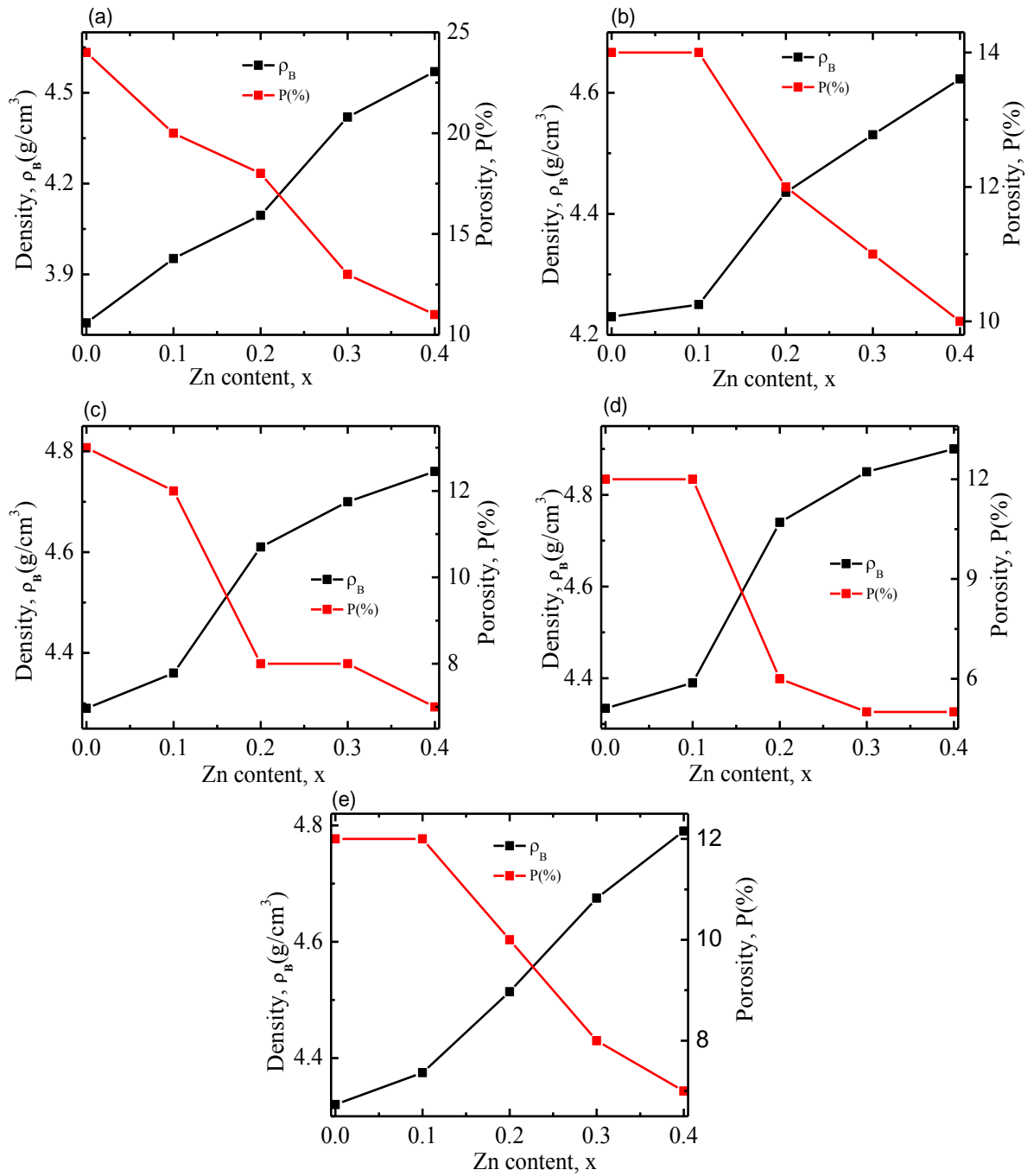
Fig. 4.7 The variation of density and porosity with *Zn* content for $Li_{0.35-0.5x}Ni_{0.3}Zn_xFe_{2.35-0.5x}O_4$ sintered at (a) 1100, (b) 1150, (c) 1200, (d) 1250 and (e) 1300ºC respectively.
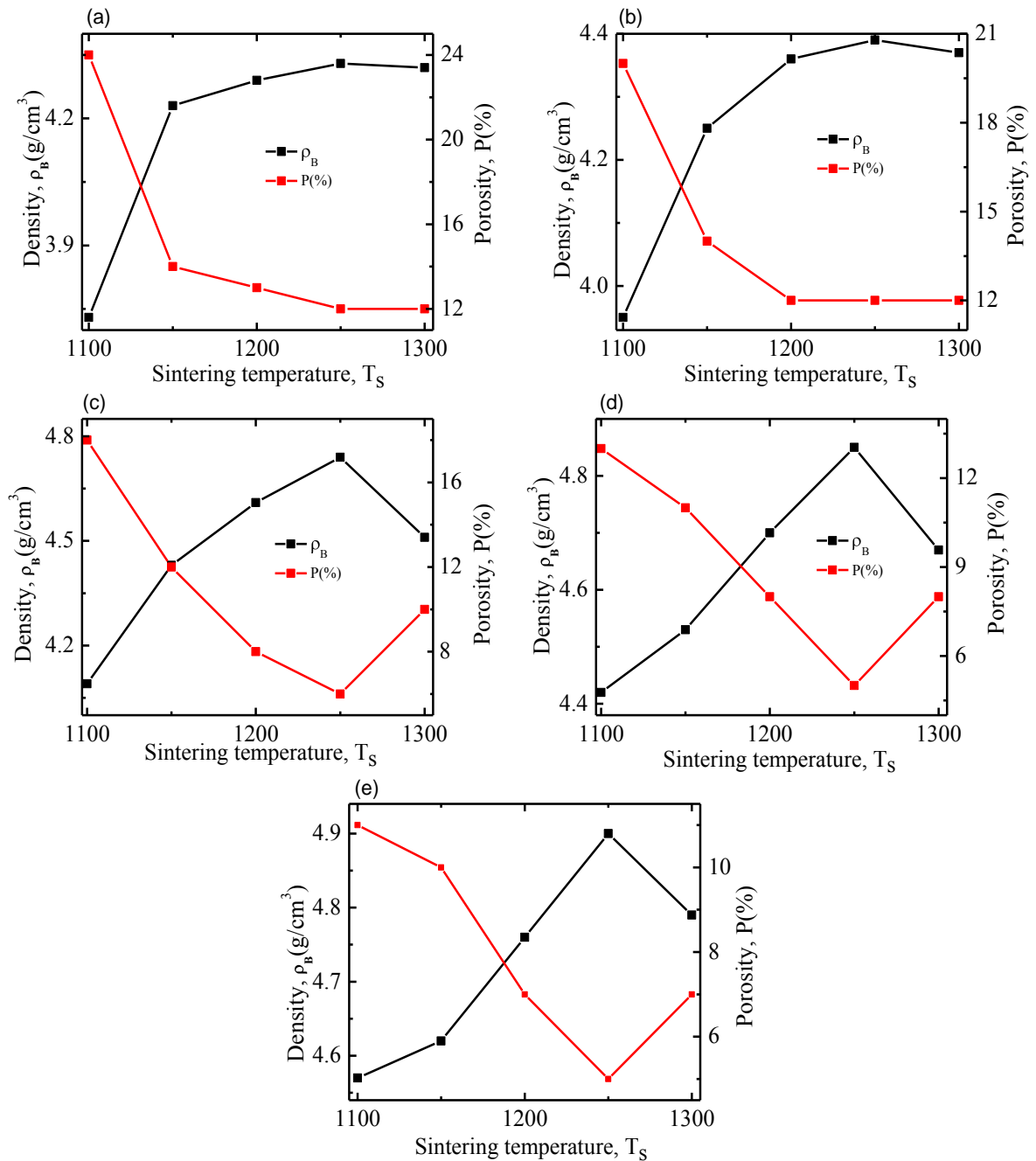
Fig. 4.8 The variation of density and porosity of $Li_{0.35-0.5x}Ni_{0.3}Zn_xFe_{2.35-0.5x}O_4$ with sintering temperature for (a) x=0.00, (b) x=0.10, (c) x=0.20, (d) x=0.30, (e) x=0.40.

The variation of ρ_B and P for various $Li_{0.35-0.5x}Ni_{0.3}Zn_xFe_{2.35-0.5x}O_4$ sintered at different T_s is shown in Fig. 4.8. The density of various $Li_{0.35-0.5x}Ni_{0.3}Zn_xFe_{2.35-0.5x}O_4$ increases as T_s increases from 1100 to 1250°C and above

1250ºC then density decreases slightly. On the other hand, *P* shows opposite trend. The values of ρ_B, ρ_{th} and *P* of various samples sintered at 1250ºC are presented in Table 4.1. During the sintering process, the thermal energy generates a force that drives the grain boundary to grow over pores, thereby decreasing the pore volume and increasing the density of the material. But beyond the sintering temperature up to 1250ºC for various $Li_{0.35-0.5x}Ni_{0.3}Zn_xFe_{2.35-0.5x}O_4$, it is found that density decreases with increasing sintering temperature. On the other hand, *P* of the samples was increasing with increasing sintering temperature. At higher sintering temperature density is decreased because the intragranular porosity is increased because of discontinuous grain growth. It is known that the porosity of the ceramic samples results from two sources, intragranular porosity and intergranular porosity. When the grain growth rate is very high, pores may be left behind by rapidly moving grain boundaries, resulting in pores that are trapped inside the grains. This intragranular porosity leads to poor magnetic and mechanical properties. Thus the total porosity could be written as $P = P_{intra} + P_{inter}$. The intergranular porosity mainly depends on the grain size [7].

4.4 Microstructures analysis of various $Li_{0.35-0.5x}Ni_{0.3}Zn_xFe_{2.35-0.5x}O_4$

The morphology of the various $Li_{0.35-0.5x}Ni_{0.3}Zn_xFe_{2.35-0.5x}O_4$ (x = 0.00 to 0.40, in steps of 0.10) is observed using FESEM. The FESEM micrographs revealed that the grain size influenced by the Zn substitution, where the average grain size increases with increasing Zn content sintered at 1250ºC as shown in Fig. 4.9. It is seen from figure that the grain are homogeneous distributed. The grain size is increasing with increasing Zn content. It is also known that Zn promotes grain growth [8], bringing about an increase in grain size. The values of average grain size of the samples are presented in Table 4.1.

It is found that the average grain size of $Li_{0.15}Ni_{0.3}Zn_{0.4}Fe_{2.15}O_4$ increases with increase of sintering temperature at shown in Fig. 4.10. Calculated average grain size of all samples is listed in Table 4.1. Similar enlargement of grain size varying sintering temperature is observed for other samples. This complies with previously reported works [9].
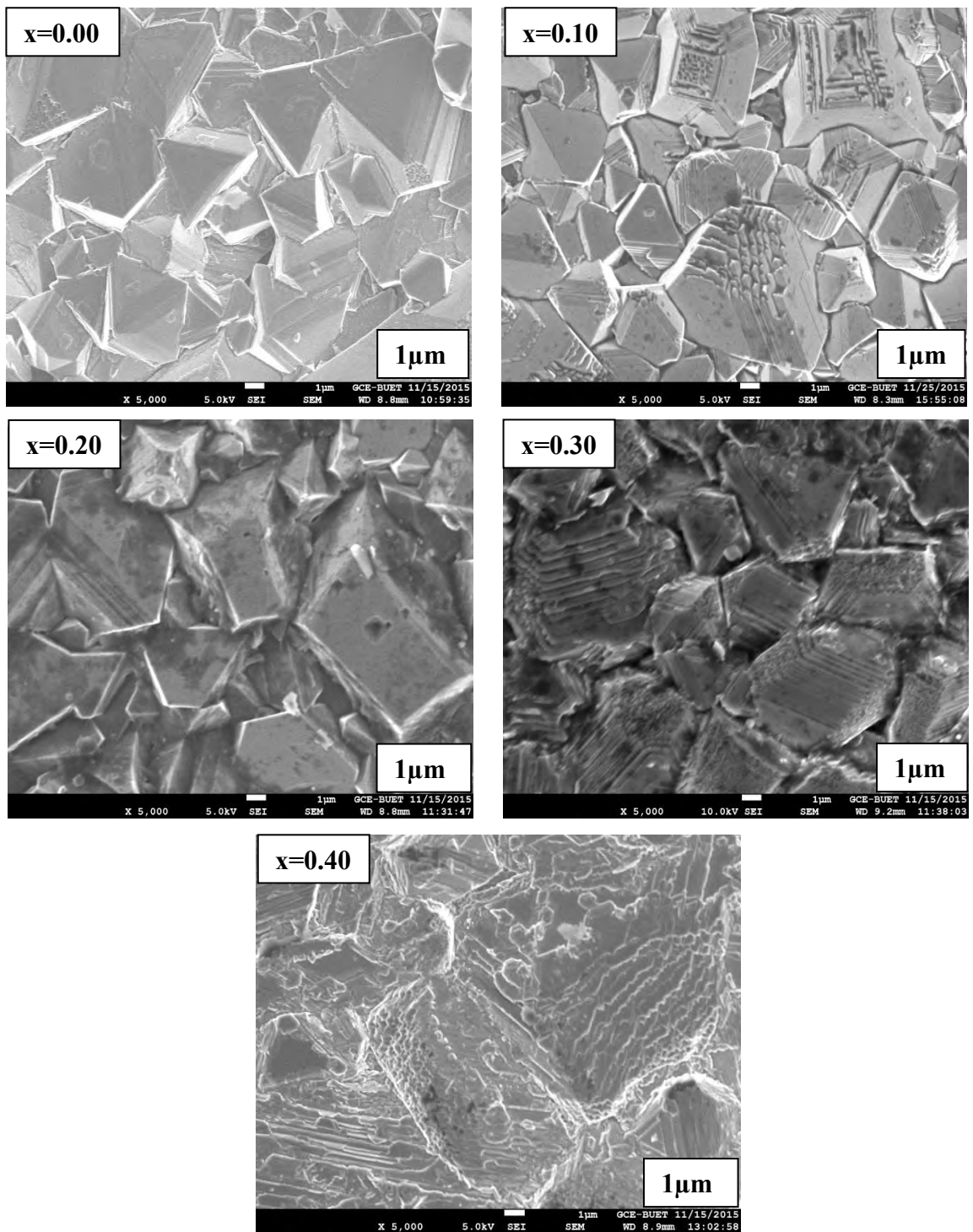
Fig. 4.9 The FESEM micrographs for $Li_{0.35-0.5x}Ni_{0.3}Zn_xFe_{2.35-0.5x}O_4$ sintered at 1250ºC.
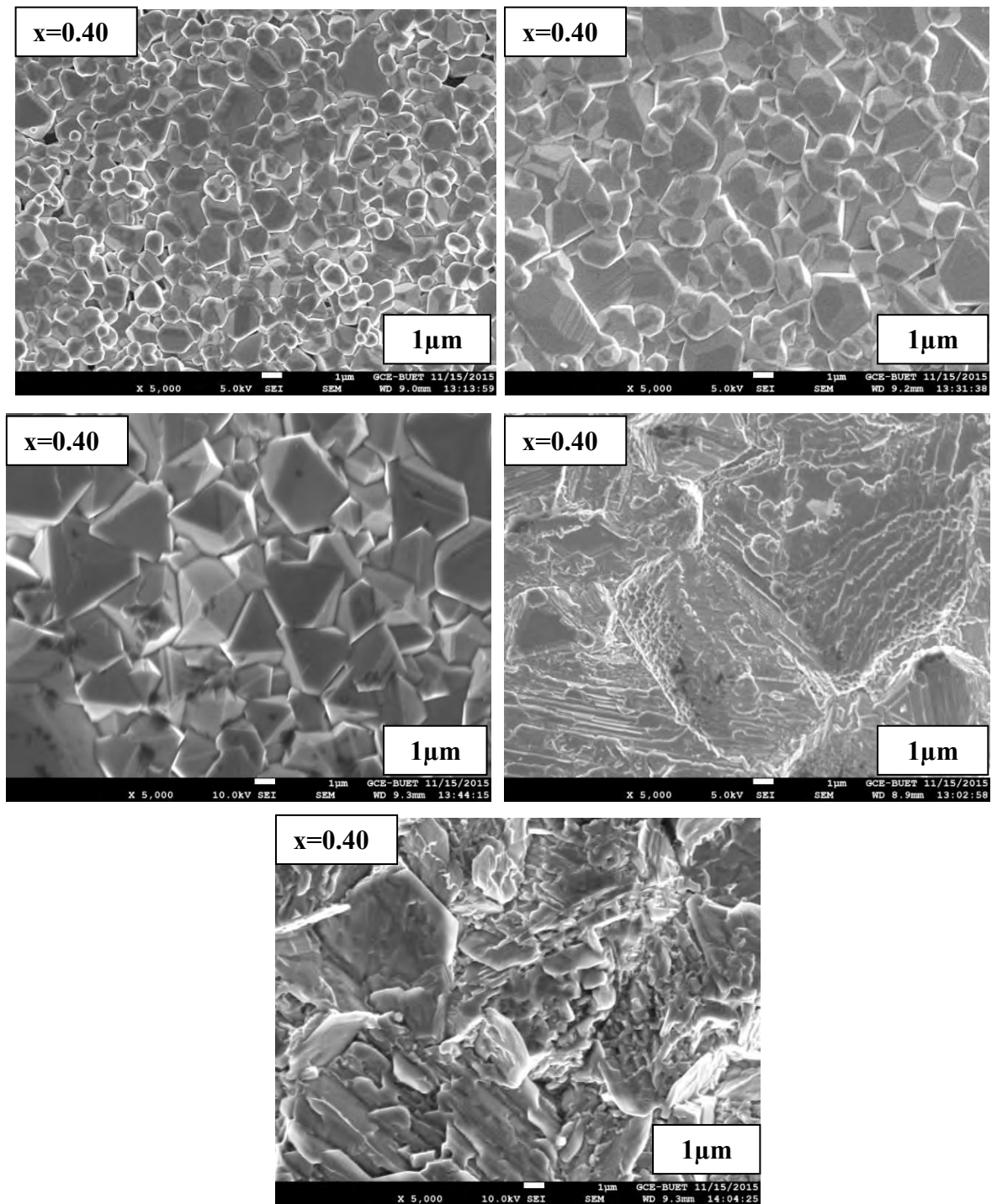
Fig. 4.10 The FESEM micrographs for $Li_{0.15}Ni_{0.3}Zn_{0.4}Fe_{2.15}O_4$ sintered at 1100, 1150, 1200, 1250 and 1300ºC.

4.5 Energy dispersive X-ray (EDX) analysis of various $Li_{0.35-0.5x}Ni_{0.3}Zn_xFe_{2.35-0.5x}O_4$

The energy dispersive X-ray (EDX) analysis of various $Li_{0.35-0.5x}Ni_{0.3}Zn_xFe_{2.35-0.5x}O_4$ are collected from FESEM to calculate and determine the composition at various T_s for 5 hour. Fig. 4.11 shows the obtained peaks correspond to Ni, Zn, Fe and O which forms the $Li_{0.2}Ni_{0.3}Zn_{0.3}Fe_{2.2}O_4$ sintered at 1250ºC. On the other hand Li has no definite peak because Li light elements cannot be routinely analyzed by EDX. Li (Z = 3) K X-rays are of too low energy to be detected by EDX.
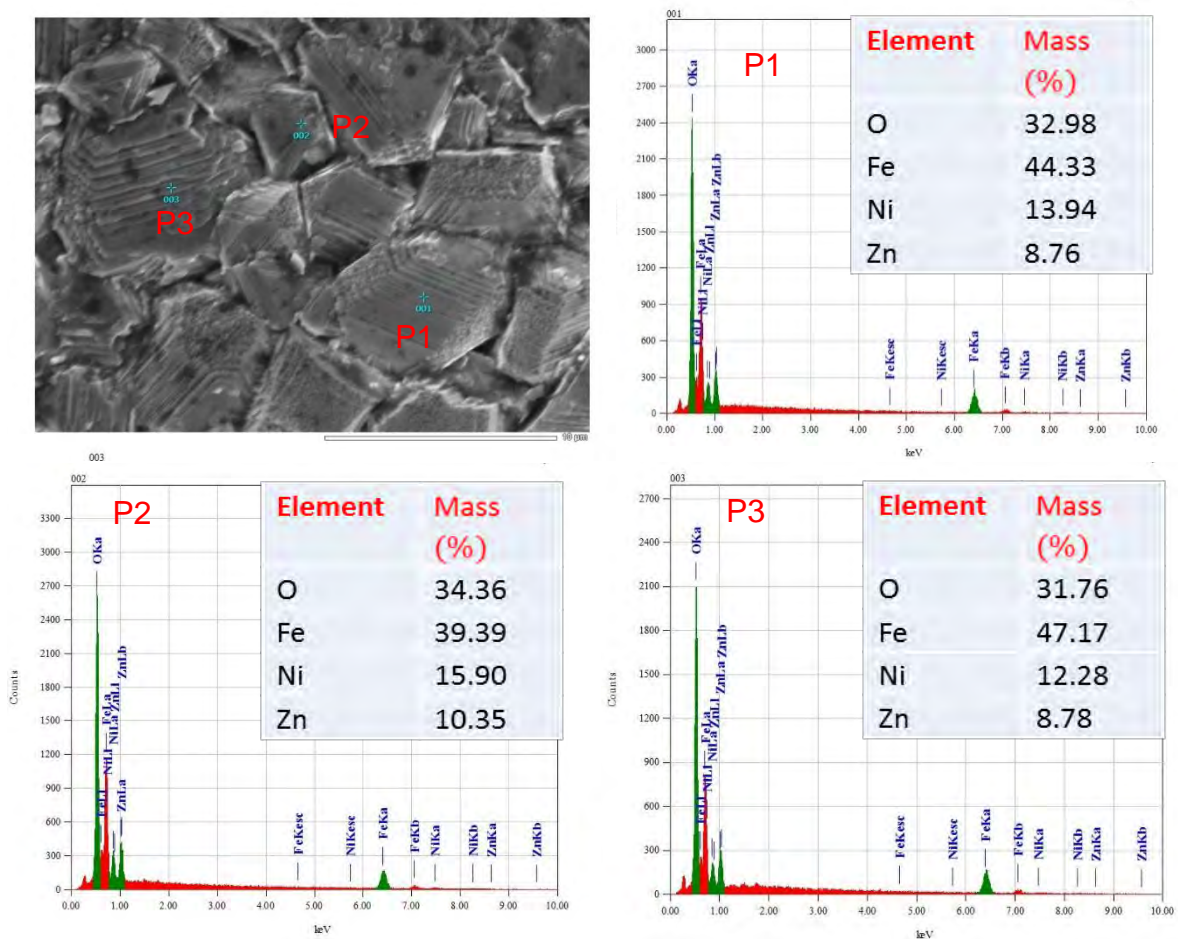
Fig. 4. 11 EDX spectrum taken on the $Li_{0.2}Ni_{0.3}Zn_{0.3}Fe_{2.2}O_4$ sintered at 1250ºC.

The EDX confirms the composition of the constituent elements present in the samples. There is no any impurities index in the compounds. EDX spectroscopy also confirmed the homogeneous distribution of the constituent elements. It is observed from the EDX spectrum that the percentage of the elements in the component phases is well consistent with the nominal composition of the phases in the ferrite materials [10]. Almost similar, percentage of the elements found in other nominal composition at various T_s.

4.5 Complex initial permeability of various $Li_{0.35-0.5x}Ni_{0.3}Zn_xFe_{2.35-0.5x}O_4$

The initial permeability (μ_i) has been measured for all the ferrites in the frequency range of 100 *Hz*-120 *MHz* Fig. 4.12 and Fig. 4.13 shows the complex permeability spectra for $Li_{0.35-0.5x}Ni_{0.3}Zn_xFe_{2.35-0.5x}O_4$ sintered at 1100, 1150, 1200, 1250 and 1300°C respectively. The real (μ_i') and imaginary (μ_i'') permeability increase with *Zn* substitution. The μ_i' values increase with the increase of sintering temperature up to 1250°C and above 1250°C a decreasing trend is observed. In contrast resonance frequency is found to decrease with *Zn* substitution. All samples show independence of frequency in their μ_i' values up to the resonance frequency. Moreover, a sharp decrease in μ_i' and increase in μ_i'' above the resonance frequency is noticed. A variation of μ_i' values the T_s for all compositions is observed. As μ_i' increases, corresponding resonance frequency, f_r decreases. For compositions x = 0.3 and x = 0.4, f_r value [11] shifted to a lower value as sintering temperature increases from 1100 to 1300°C, which is found from Table 4.1. No resonance frequency is observed for $Li_{0.35}Ni_{0.3}Fe_{2.35}O_4$. For compositions x = 0.00 resonance frequency, f_r are above the measured frequency range (120 MHz). Though their permeability is lesser but their usable bandwidth is higher.

They are well suited for application in the high frequency range. It is clearly noticeable that the maximum initial permeability $\mu_i^/$ of $Li_{0.35-0.5x}Ni_{0.3}Zn_xFe_{2.35-0.5x}O_4$ are obtained at 1250ºC which is almost two times larger than the initial value and at higher sintering temperature a decreasing trend is observed.
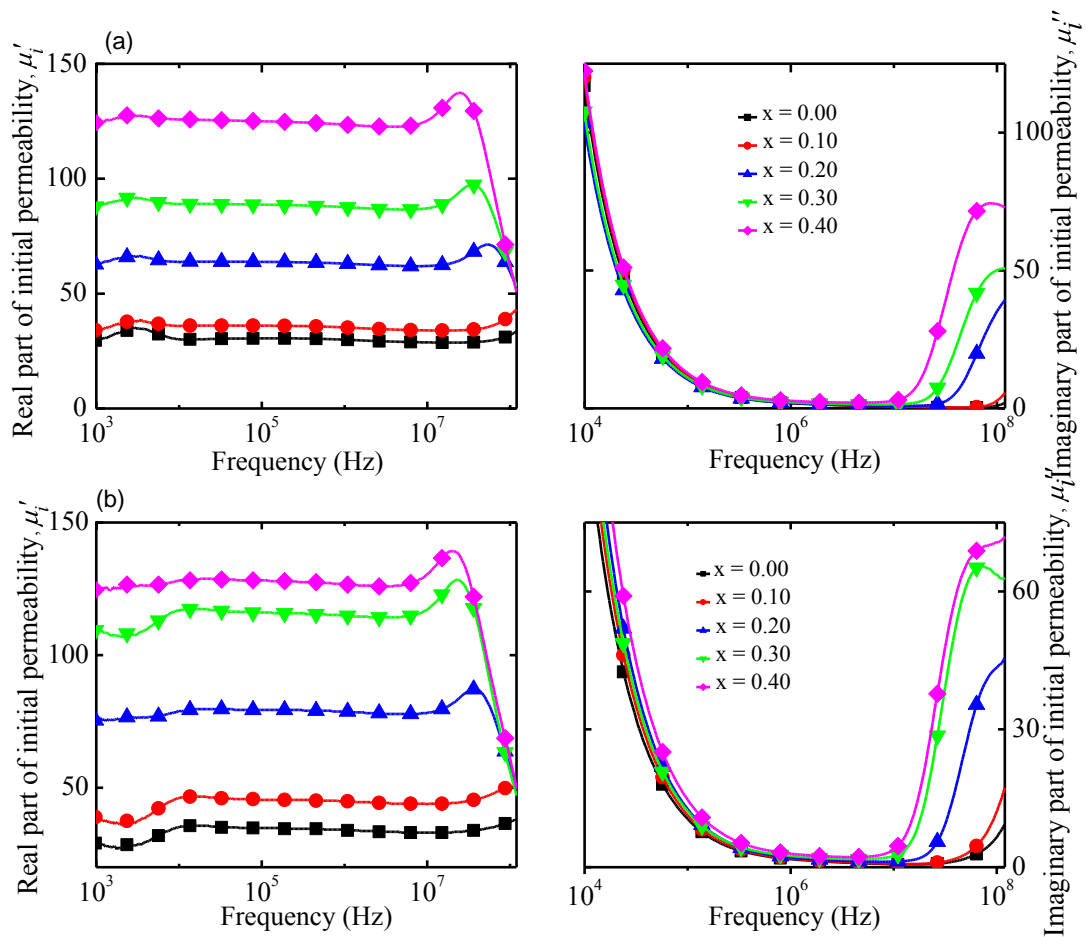

Fig. 4.12 The variation of $\mu_i^/$ and $\mu_i^{//}$ spectra for $Li_{0.35-0.5x}Ni_{0.3}Zn_xFe_{2.35-0.5x}O_4$ sintered at (a) 1100 and (b) 1150ºC respectively.
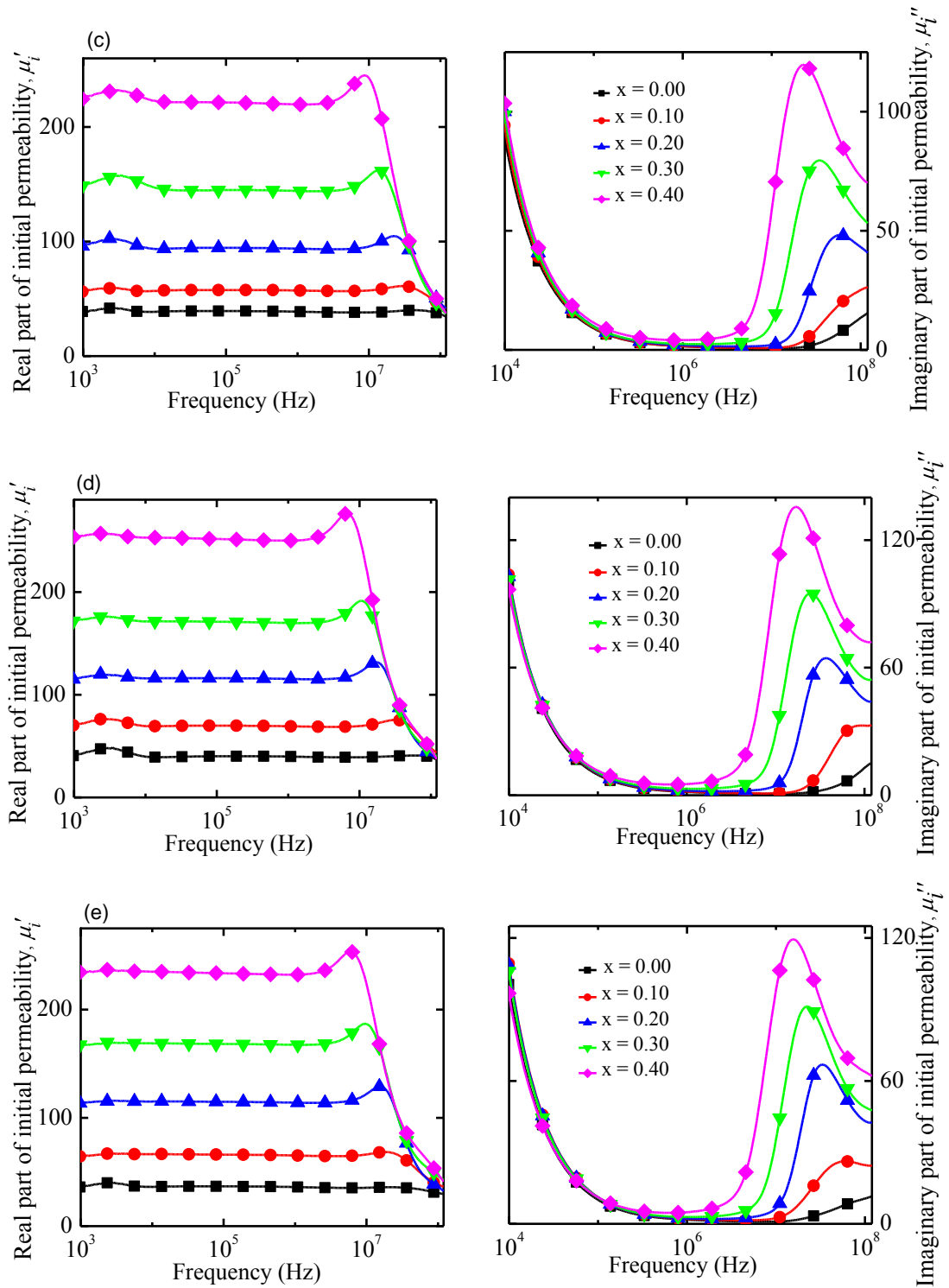
Fig. 4.13 The variation of $\mu_i^{/}$ and $\mu_i^{//}$ spectra for *Li$_{0.35-0.5x}$Ni$_{0.3}$Zn$_x$Fe$_{2.35-0.5x}$O$_4$* sintered at (c) 1200, (d)

1250 and (e) 1300ºC respectively.

The resonance frequency and the room temperature $\mu_i^/$ values measured at 1 MHz are listed in Table 4.1. Highest value of $\mu_i^/$ (254) is observed for $Li_{0.15}Ni_{0.3}Zn_{0.4}Fe_{2.15}O_4$ sintered at 1250ºC. On the other hand, maximum value of f_r (113 MHz) is observed for $Li_{0.2}Ni_{0.3}Zn_{0.3}Fe_{2.2}O_4$ sintered at 1100ºC with the corresponding alue of $\mu_i^/ = 88$. From Table 4.1 it is found that as $\mu_i^/$ increases resonance frequency decreases with the function of sintering temperature. An inversely proportional relation of $\mu_i^/$ and f_r confirms the Snoek's limit [12]. Similar trend is observed for all other T$_s$.

The whole permeability phenomena can be explained as below. The permeability of polycrystalline ferrite is related to two different magnetizing mechanisms: spin rotation and domain wall motion [9, 13-14], which can be described as follows: $\mu_i = 1 + \chi_w + \chi_{spin}$ where χ_w is the domain wall susceptibility; χ_{spin} is intrinsic rotational susceptibility. χ_w and χ_{spin} may be written as : $\chi_w = \dfrac{3\pi M_s^2 D}{4\gamma}$ and $\chi_{spin} = \dfrac{2\pi M_s^2}{K}$ with M_s saturation magnetization, K the total anisotropy, D the average grain diameter, and γ the domain wall energy. Therefore in the present case, variation of the initial permeability is strongly influenced by its grain size and P.

The increasing value of $\mu_i^/$ with the increase of sintering temperature up to the 1250ºC is due to the lower P for samples sintered at higher sintering temperature. The P causes hindrance to the domain wall motion. As sintering temperature increases pores and voids are reduced with increasing sintering temperature. The value of $\mu_i^/$ decreases above 1250ºC because the sample heated at higher T$_s$ (above optimum T_s) contains increasing number of pores within the grains which results a decrease in permeability. Similar trend was observed by Guillaud [15] the variation of initial permeability, $\mu_i^/$,

with frequency, shown in Fig. 4.12 and Fig. 4.13 can be explained on the basis of Globus model. According to this model, the relaxation character is

$$(\mu_i - 1)^2 f_r = \text{constant.} \tag{2}$$

Initial permeability in ferrites is due to domain wall displacement and remains constant with frequency as long as there is no phase lag between the applied field and the applied field and the domain wall displacement. In ferrites, two resonance peaks are normally observed: one at lower frequency (10-100 *MHz*) which is due to the domain wall oscillations [16, 17] and the other at higher frequencies (~1 *GHz*) due to Larmour precession of electron spins [18]. In the present case, the resonance frequency of domain wall oscillations is found in the range of 15 *MHz*~113 *MHz*.
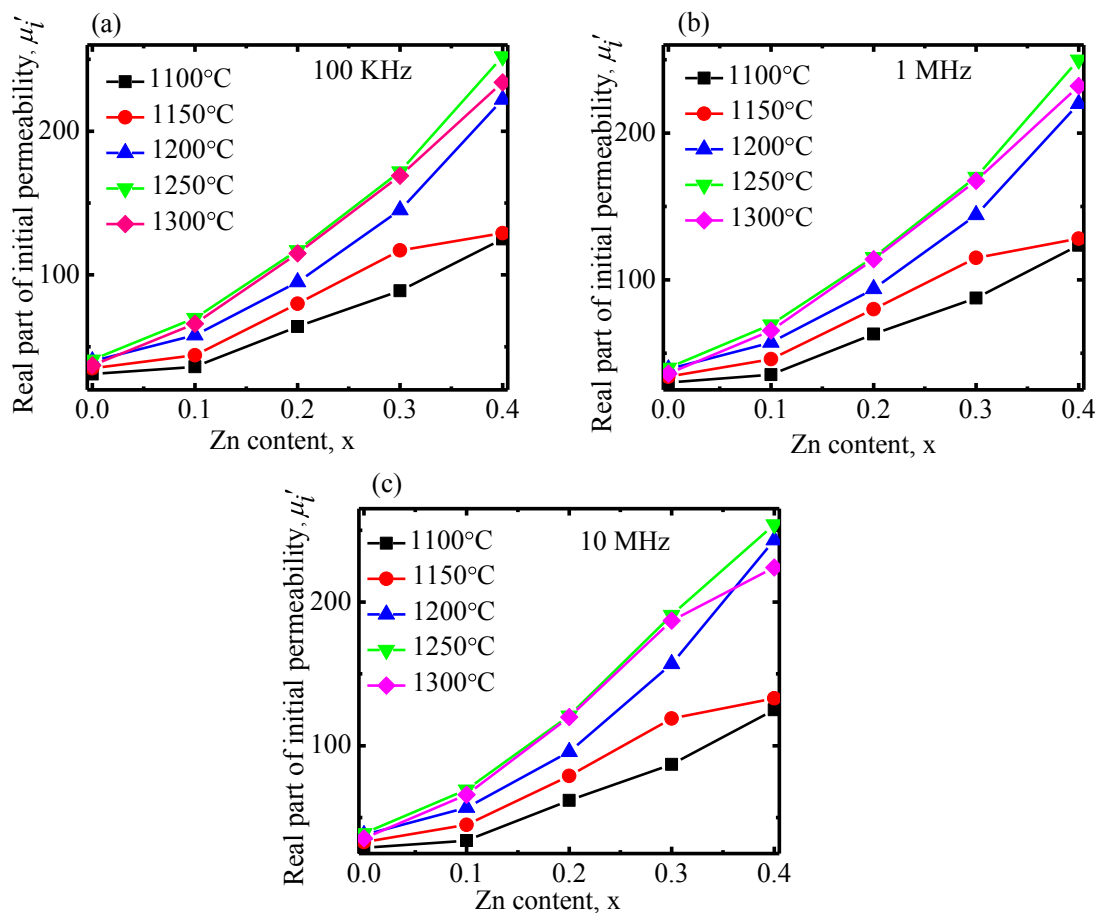
Fig. 4.14 Variation of real part of initial permeability of various $Li_{0.35-0.5x}Ni_{0.3}Zn_xFe_{2.35-0.5x}O_4$ for different temperatures at frequencies (a) 100 kHz (b) 1 MHz and (c) 10 MHz.

Fig. 4.14 shows the variation of $\mu_i^{/}$ (at 100 kHz, 1 MHz and 10 MHz) with Zn content for $Li_{0.35-0.5x}Ni_{0.3}Zn_xFe_{2.35-0.5x}O_4$ sintered at 1100, 1150, 1200, 1250 and 1300ºC. In this figure it is found that $\mu_i^{/}$ remains almost constant up to resonance frequency and then it starts to decreases. The variation of loss factor, $tan\delta$ ($= \dfrac{\mu_i^{//}}{\mu_i^{/}}$) with frequency for all samples has been studied. Fig. 4.15 shows the variations of loss factors with frequency for $Li_{0.35-0.5x}Ni_{0.3}Zn_xFe_{2.35-0.5x}O_4$ sintered at 1100, 1150, 1200, 1250 and 1300ºC.
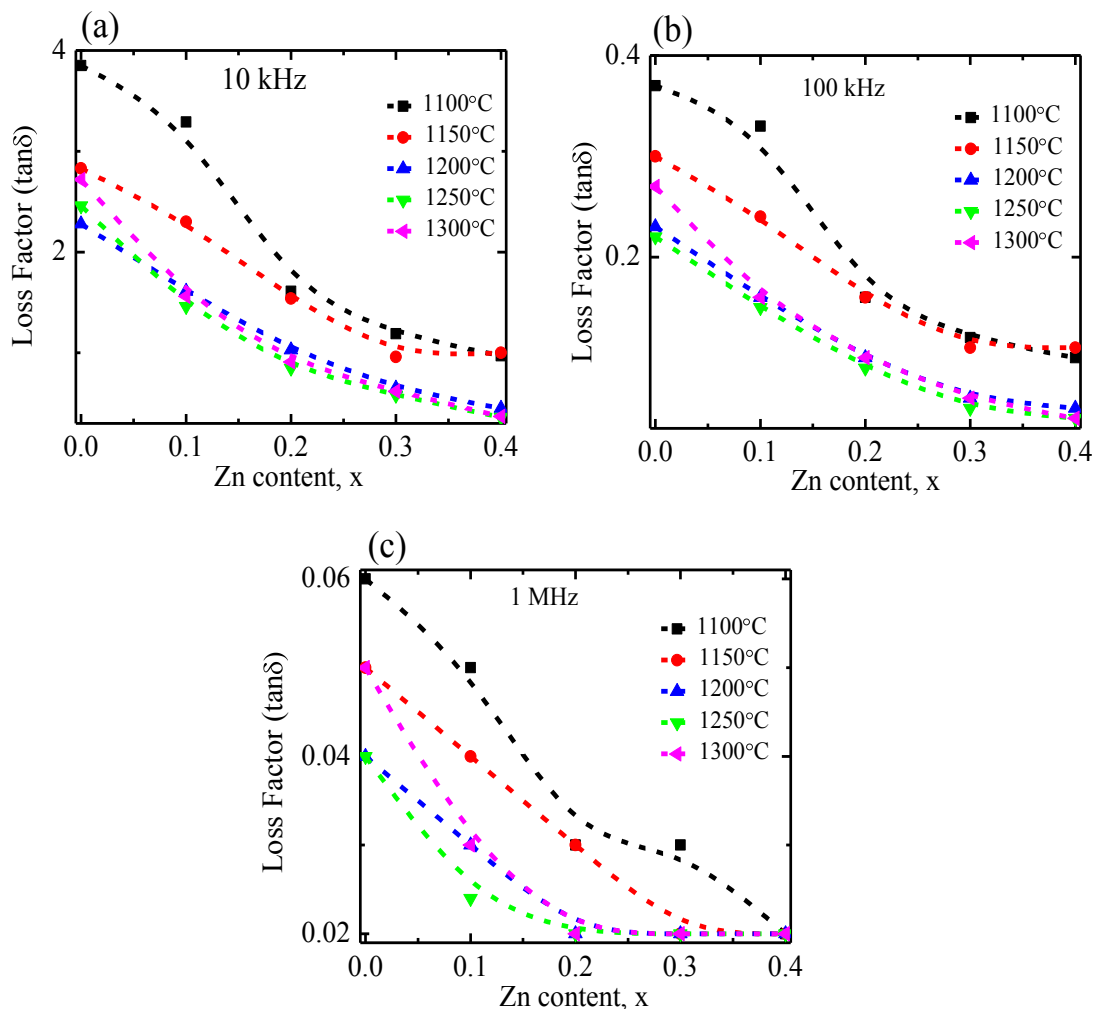

Fig. 4.15 The variation of Loss factor for various $Li_{0.35-0.5x}Ni_{0.3}Zn_xFe_{2.35-0.5x}O_4$ for different temperatures at frequencies (a) 10 kHz (b) 100 kHz and (c) 1 MHz.

At lower frequencies dispersion in magnetic loss is observed and remains constant up to certain a frequency, this frequency limit depends upon the T_s. The lag of domain wall motion with respect to the applied magnetic field is responsible for magnetic loss and this is accredited to lattice imperfections [18].

At higher frequencies, a rapid increase in loss factor is observed. A resonance loss peak is shown in this rapid increase of magnetic loss. At the resonance, maximum energy transfer occurs from the applied field to the lattice which results the rapid increases in loss factor. As it is observed that phase lag between domain rotation and applied field is greater than that between applied field and domain wall displacement, the magnetic losses due to domain rotation overrides those due to domain wall displacement [19].

The loss factor is also observed to increase with the increase of sintering temperature. The variation of initial loss with frequency for the sample x = 0.40, i.e. $Li_{0.15}Ni_{0.3}Zn_{0.4}Fe_{2.15}O_4$ in the sintering temperature range 1100 to 1300ºC is shown in Fig. 4.16. The increase in sintering temperature results in increased loss in the samples, thereby creating defects in the lattice, which gives rise to magnetic loss.

From the loss factor, the relative quality factor (or *Q-factor*) is calculated. The relative quality factor (*Q-factor*) versus frequency plots of all the samples sintered at 1100, 1150, 1200, 1250 and 1300ºC are shown in Fig. 4.17. Calculated *Q-factor*s for various $Li_{0.35-0.5x}Ni_{0.3}Zn_xFe_{2.35-0.5x}O_4$ sintered at various temperatures are listed in Table 4.1. It can be seen that the value of *Q*-factor increases with an increase of frequency and shows a peak around 10 *MHz*. It is also observed from the Fig. 4.17 that the maximum value of *Q-factor*, Q_{max} increases with increasing Zn contents from *x* = 0.00 to *x* = 0.40 in $Li_{0.35-0.5x}Ni_{0.3}Zn_xFe_{2.35-0.5x}O_4$, for the samples sintered at 1250ºC.
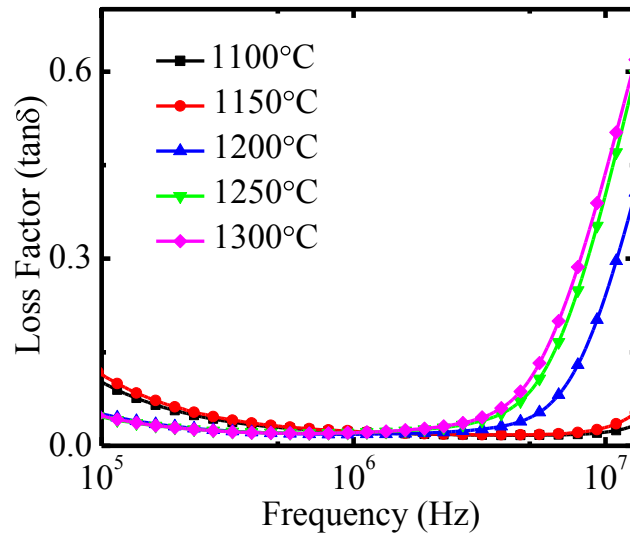
Fig. 4.16 The variations of Loss factor with frequency for $Li_{0.15}Ni_{0.3}Zn_{0.4}Fe_{2.15}O_4$ sintered at 1100, 1150, 1200, 1250 and 1300ºC respectively.

Similar variation is observed for $Li_{0.35-0.5x}Ni_{0.3}Zn_xFe_{2.35-0.5x}O_4$ sintered at other temperatures as well. It shows a similar trend of $\mu_i^/$ of the present system as it is proportional to the *Q*-factor from the relation: $Q = \dfrac{\mu_i^/}{\tan\theta}$, as loss factor also shows an increasing trend with the increase of *Zn* content. Among all the studied samples, highest value of *Q*-factor (12395) is observed for $Li_{0.15}Ni_{0.3}Zn_{0.4}Fe_{2.15}O_4$ sintered at 1250ºC, similar to $\mu_i^/$. Above 1250ºC, *Q-factor* is found to decrease because at higher sintering temperature, abnormal grain growth occurs which creates trapped pores inside the grain. This increasing amount of pores influences the loss factor and turns into higher value which results a lower value of *Q*-factor.

Fig. 4.17 The variations of Relative Quality factors (*Q*-factor) with frequency for $Li_{0.35-0.5x}Ni_{0.3}Zn_xFe_{2.35-0.5x}O_4$ sintered at (a) 1100, (b) 1150, (c) 1200, (d) 1250 and (e) 1300ºC respectively.

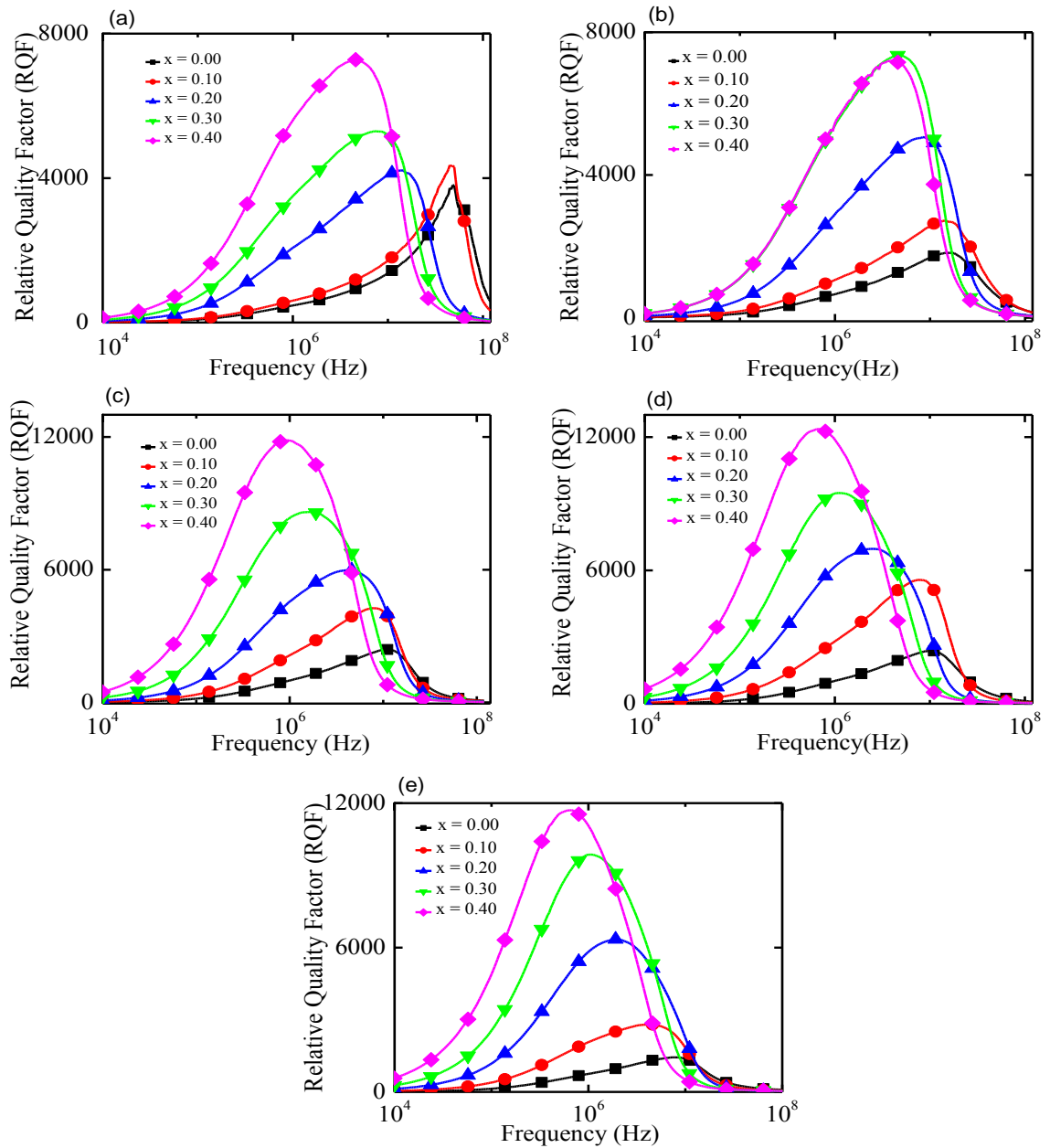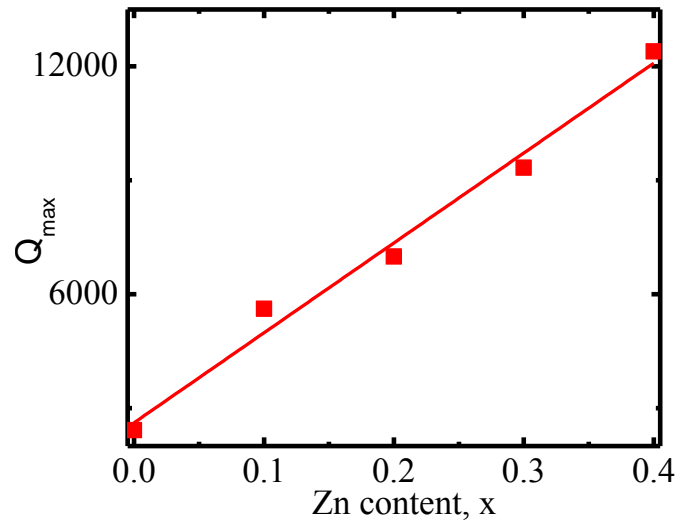**Fig. 4.18** The variations of Q_{max} with Zn content for $Li_{0.15}Ni_{0.3}Zn_{0.4}Fe_{2.15}O_4$ sintered at 1250ºC.

4.6   Temperature   dependence   of   initial   permeability   various $Li_{0.35-0.5x}Ni_{0.3}Zn_xFe_{2.35-0.5x}O_4$

Temperature dependent of initial permeability furnish valuable information about domain nature [20], Néel temperature (T_N) [21] and factor contributing to permeability [22]. The variation of initial permeability ($\mu_i^/$) measured at a constant frequency (10 kHz) of a sinusoidal wave with temperature of the samples. The parameters such as saturation magnetization (M_s) anisotropy constant (K_1) and diameter of grain (D_m) are responsible for the diversity of the temperature spectra of $\mu_i^/$ of the ferrite sample. The $\dfrac{\mu_i^/}{\mu_{i(minimum)}^/}$, as a function of temperature for various $Li_{0.35-0.5x}Ni_{0.3}Zn_xFe_{2.35-0.5x}O_4$ sintered at 1250ºC is shown in Fig. 4.19 for the toroid shaped samples. Since the initial permeability is directly related to the magnetization and to the ionic structure, then the thermal spectra of permeability can be taken as a test of the formation and homogeneity of the ionic structure of the samples. In general, it

was found that the $\mu_i^/$ increases with increase in temperature, while it falls abruptly

close to the Néel temperature. It is seen from Fig. 4.19 that $\mu_i^/$ gradually increases with

temperature reaches a maximum and then drops sharply to minimum value near the T_N.

The sharpness of the permeability drop at the T_N can be used as a measure of the degree

of compositional homogeneity according to Globus. The present ferrites show good

homogeneity as shown in Fig. 4.19, where an abrupt drop in permeability occurs within

the temperature range less than 5°C near T_N. The variation of $\mu_i^/$ with temperature can be

expressed as follows: The K_1 and M_s usually decrease with increase in temperature, due

to thermal agitation, which disturbs the alignment of magnetic moments. But, decrease

of K_1 with temperature is much faster than the decrease of M_s. When the K_1 reaches to

zero, $\mu_i^/$ attains its maximum value and then drops off to minimum value near the T_N.

The permeability of polycrystalline ferrites is given by according to the equation

$$\left[\mu_i' = \frac{M_s^2 D}{\sqrt{K_1}} \right]$$

$\mu_i^/$ must show a maximum at temperature at which K_1 vanishes, where D is the diameter

of the grain. T_N of a ferrite is a temperature at which the ferrimagnetic material becomes

paramagnetic. T_N gives an idea of the amount of energy takes to break up the long-range

ordering in the material. T_N of the studied ferrite system has been determined from the

$\mu_i^/$-T curves where Hopkinson type of effect at the T_N has been observed with the

manifestation of sharp fall of permeability. The decreasing of T_N with an increasing Zn

content can be explained by the Néel molecular field model. According to this model,

the A-B super exchange interactions are dominant compared with those of A-A or B-B

interactions. Thus, the T_N of the ferrites is determined principally by the strength of A-B

interaction. Abeledo et. al. [23] reported that recent Mössbauer spectroscopy investigation of Zn substituted lithium ferrites confirms that Zn^{2+} have a strong A-site preference. According to Rosence waig model canting will occur in the sub lattice not experiencing diamagnetic substitution and the average canting angle should increase with increasing diamagnetic substitution. So A-B interaction decreases with increasing Zn substitution. As A-B interaction decreasing, the decrease in T_N is expected. The value of T_N is found to 665 to 390ºC (as in Table 4.2). Fig. 4.20 shows the variation of lattice constant and Néel temperature as a function of Zn content for various $Li_{0.35-0.5x}Ni_{0.3}Zn_xFe_{2.35-0.5x}O_4$ sintered at 1250ºC. Lattice constant increases with x content whereas Néel temperature decreases. The Néel temperature gives an idea of the amount of energy takes to break up the long-range ordering in the materials. The decreases of the Néel temperature with Zn substitution is due to the strengthening of the *A-B* interaction correspondingly between two sub-lattices.
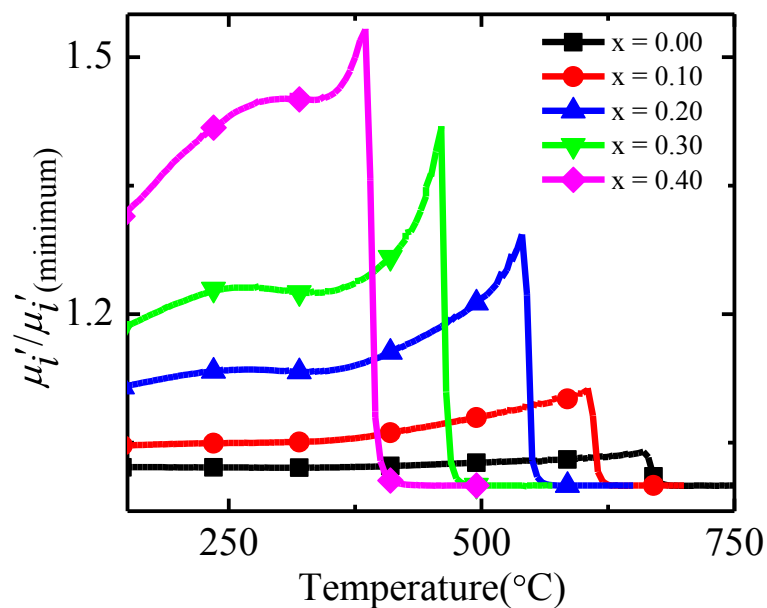

Fig. 4.19 The temperature dependence of $\mu_i^{/}$ for $Li_{0.35-0.5x}Ni_{0.3}Zn_xFe_{2.35-0.5x}O_4$ sintered at 1250ºC.

103
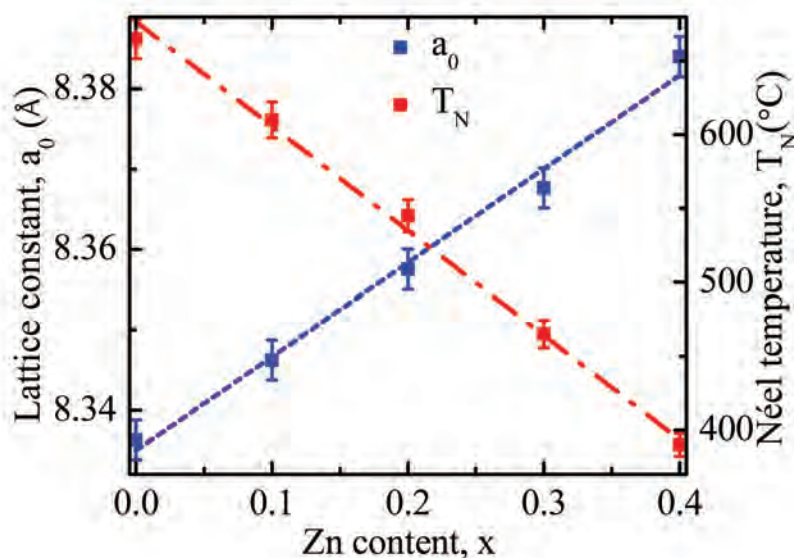
Fig. 4.20 Variation of the lattice constant a_o, and Neel temperature, T_N as a function of Zn content for $Li_{0.35-0.5x}Ni_{0.3}Zn_xFe_{2.35-0.5x}O_4$ sintered at 1250ºC.

This could be attributed to the increases in distance (Hopping length, L between the magnetic ions of tetrahedral A- site (L_A) and the octahedral B-sites (L_B). This is also confirmed by the increases in the lattice parameter with increasing Zn content.

4.7 DC magnetization of various $Li_{0.35-0.5x}Ni_{0.3}Zn_xFe_{2.35-0.5x}O_4$

The magnetic properties of the various $Li_{0.35-0.5x}Ni_{0.3}Zn_xFe_{2.35-0.5x}O_4$ have been determined at room temperature (300K) using a vibrating sample magnetometer. The *M-H* loops are very narrow for the samples and the obtained magnetic parameters are shown in Fig. 4.21 and Table 4.2 separately. As a normal behavior, the magnetization of all samples increases linearly with increasing of the applied magnetic field up to 0.20T and attains its saturation values for fields higher than 0.20T. It is clear that, as Zn concentration increases $\mu_i^/$ and M_s increases up to its maximum value at x = 0.4.
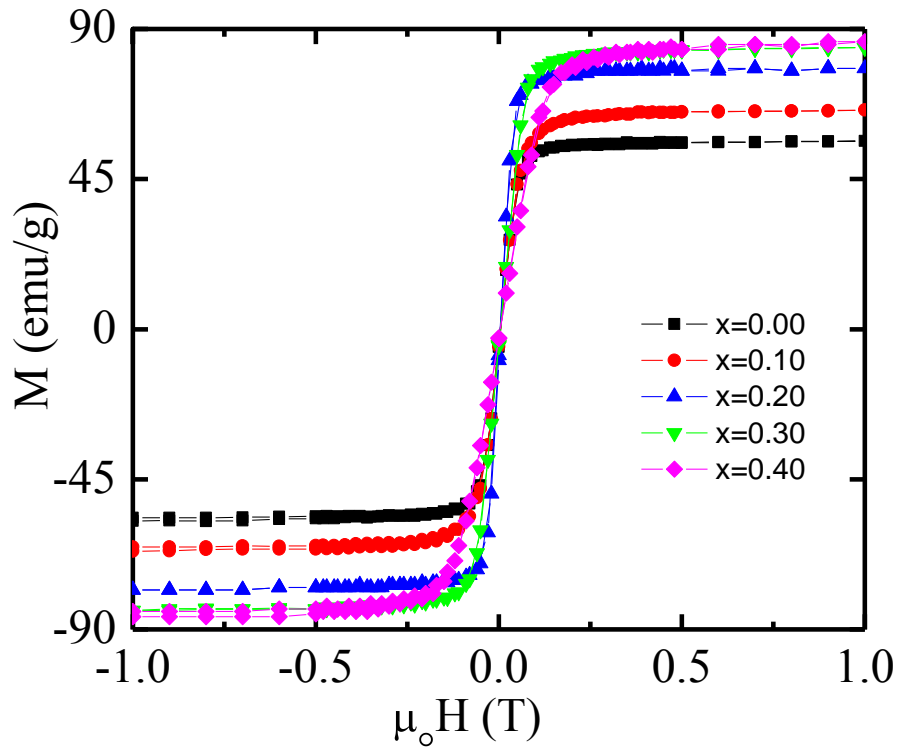
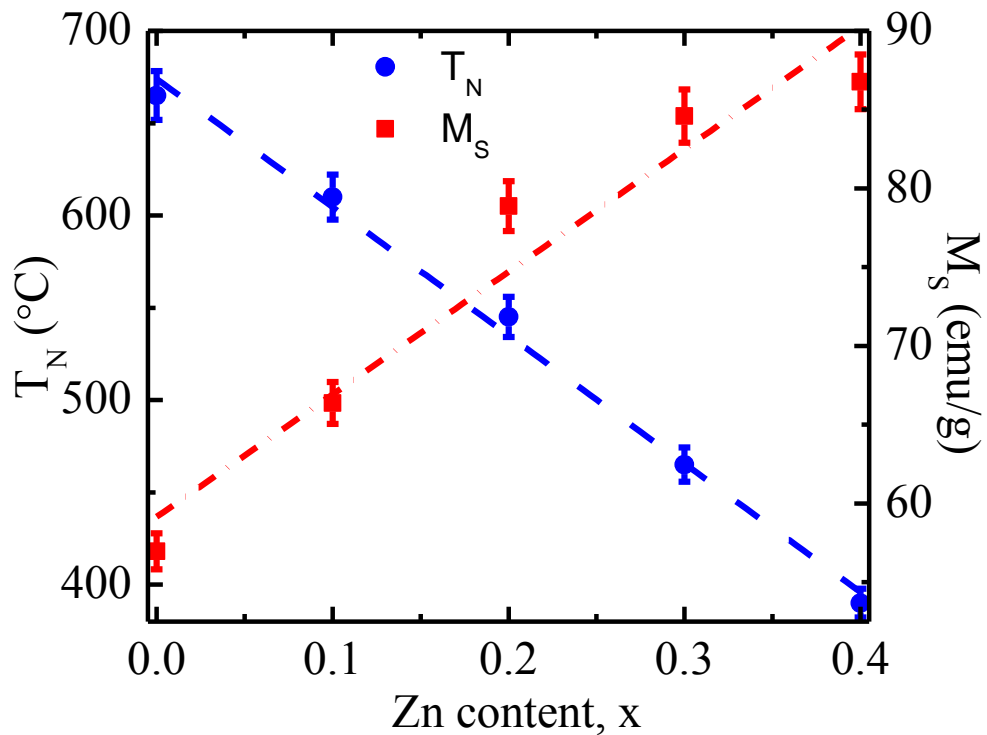**Fig. 4.21** *M-H* loops for $Li_{0.35-0.5x}Ni_{0.3}Zn_xFe_{2.35-0.5x}O_4$ sintered at 1250ºC.

Fig. 4.22 Variation of T_N and M_s with Zn content for $Li_{0.35-0.5x}Ni_{0.3}Zn_xFe_{2.35-0.5x}O_4$ sintered at 1250ºC.

Table 4.2 The saturation magnetizing field, saturation magnetization, number of Bohr magneton, and Néel temperature for various nanocrystalline $Li_{0.35-0.5x}Ni_{0.3}Zn_xFe_{2.35-0.5x}O_4$.

Composition	H_s (T)	M_s (emu/g)	n_B (th) (μ_B)	n_B (expt.) (μ_B)	T_N (°C)
x = 0.00	0.1370	56	2.35	2.18	665
x = 0.10	0.1911	65	3.10	2.57	611
x = 0.20	0.1035	78	3.85	3.11	564
x = 0.30	0.1463	84	4.60	3.41	465
x = 0.40	0.2805	86	5.35	3.53	390

This could be explained by the cation distribution and super-exchange interaction tetrahedral (A) and octahedral (B) sites. In the present study, the considering the cationic formula of these compositions can be written as

$(Zn^{2+}_x Fe^{3+}_{1-x})_A [Li^{1+}_{0.35-0.5x} Ni^{2+}_{0.3} Fe^{3+}_{1.35+0.5x}]_B O_4$
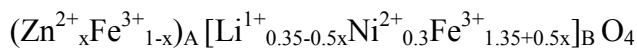
where the parentheses ( ) and square brackets [ ] represent tetrahedral (A) and octahedral (B) sites, respectively. It is known that Li^{1+} (non-magnetic) and Ni^{2+} (magnetic moment $= 2\mu_B$) ions occupy B sites while Zn^{2+} (non-magnetic) ions prefer the A sites. Although Fe^{3+} (magnetic moment $= 5\,\mu_B$) ions exist at both A and B sites [24].

According to Neel's two sub-lattice model AB super-exchange interaction is predominant over intersublattice AA and BB interaction, and the net magnetization is given by the vector sum of the magnetic moments of the individual A and B sub-lattices i.e. $M = M_B - M_A$. As Li^{1+} and Zn^{2+} do not contribute to the magnetization because of being non-magnetic, Ni^{2+} and Fe^{3+} ions having magnetic moment $2\mu_B$ and $5\mu_B$, respectively results the net magnetic moment which can be given by,

$M_B - M_A = [(7.35+2.5x)\,\mu_B - (5-5x)\,\mu_B\,]$

$$= (7.35\ \mu_B + 2.5x\ \mu_B - 5\ \mu_B + 5x\ \mu_B)$$

$$= (2.35 + 7.5x)\ \mu_B.$$

where, $M_B = [(0.3 \times 2) + 5(1.35 + 0.5x)]\ \mu_B$

$$= [0.6 + 6.75 + 2.5x]\ \mu_B$$

$$= (7.35 + 2.5x)\ \mu_B$$

and $M_A = [5(1-x)]\ \mu_B$

$$= (5 - 5x)\ \mu_B$$

It can also be seen that net magnetization increases with x. Increase in Zn concentration causes decrease in M_A and increase in M_B and in this way, the net magnetization increase.

References:

[1]   Hossain, A. K. M. A., Seki, M., Kawai, T. and Tabata, H., "Colossal magnetoresistance in spinel type $Zn_{1-x}Ni_xFe_2O_4$", *J. Appl. Phys.*, Vol. 96, pp. 1273-1275, 2004.

[2]   Scherrer, P., "Bestimmung der Grösse und der Innere Struktur von Kolloidteilchen Mittels Röntgenstrahlen, Nachrichten von der Gesellschaft der Wissenschaften, Göttingen", *Math. Phys.*, Vol. 2, pp. 98-100, 1918.

[3]   Nelson, J. B. and Riley, D. P., "An experimental investigation of extrapolation methods in the derivation of accurate unit-cell dimensions of crystals", *Proc. Phys. Soc. London*, Vol. 57, pp. 160, 1945.

[4]   Whittaker, E. J. W. and Muntus, R., "Ionic radii for use in geochemistry", *Geochimica et Cosmochimica Acta*, Vol. 34, pp. 945-956, 1970.

[5]   Muhammad Ajmal and Asghari Maqsood, "Influence of Zinc substitution on structural and electeical properties of $Ni_{1-x}Zn_xFe_2O_4$ ferrites", *Mater. Sci. Eng. B*, Vol. 139(2), pp. 164-170, 2007.

[6]   Winter, M. J., www.webelements.com, University of Sheffield, UK, 1995-2006.

[7]   Sattar, A. A., El-Sayed, H. M., El-Shokrofy, K. M. and El-Tabey, M. M., "Improvement of the magnetic properties of Mn-Ni-Zn ferrite by the non-magnetic Al^{3+} ion substitution", *J. Appl. Phys.*, Vol. 5(1), pp. 162-168, 2005.

[8]   Scherrer, H. E., Kisker, H., Kronmuller, H. and Wurschum, R., "Magnetic properties of Nanocrystalline nickel", *Nanostruct. Mater.*, Vol. 6, pp. 533-538, 1995.

[9]   Mahmud, S.T., Hossain, A. K. M. A., Hakim, A. K. M. Abdul, Seki, M., Kawai, T. and Tabata, H., "Influence of microstructure on the complex permeability of spinel type Ni –Zn ferrite", *J. Magn. Magn. Mater.*, Vol. 305, pp. 269–274, 2006.

[10]   Abdul, Gaffoor and Ravinder, D., "Characterization of nano-structured Nickel-Cobalt ferrites synthesized by citrate-gel auto combustion method", *Int. J. Eng. Res. and Appl.*, Vol. 4, pp. 73-79, 2014.

[11]   Valenzuela, R., *Magnetic Ceramics*, Cambridge University Press, Cambridge, 1994.

[12]   Snoek, J. L., "Dispersion and absorption in magnetic ferrites at frequencies above one Mc/s", *Physica*, Vol. 14, pp. 207-217, 1948.

[13]   Jun, Hu and Mi, Yan, "Preparation of high permeability Ni-Cu-Zn ferrite", *J. Zhejiang Univ. Sci.,* Vol. 6B (6), pp. 580-583, 2005.

[14]   Tsutaoka, T., Ueshima, M., Tokunaga, T., Nakamura, T. and Hatakeyama, K., "Frequency dispersion and temperature variation of complex permeability of Ni-Zn ferrite composite materials", *J. Appl. Phys.*, Vol. 78(6), pp. 3983-3991, 1995.

[15]   Guillaud, C., "The properties of manganese-zinc ferrites and the physical processes governing them", *Proc. IEEE*, Vol. 104B, pp. 165-173, 1957.

[16]   Kang, S. H. and Yoo, H. I., "The effect of nonstoichiometry (δ) on the magnetic properties of $(Mg_{0.22}Mn_{0.07}Fe_{0.71})_{3-\delta}O_4$ ferrite", *J. Appl. Phys.*, Vol-88, pp. 4754-4757, 2000.

[17]   Caltun, O. F. and Spinu, L., "Magnetic properties of high frequency NiZn ferrites doped with CuO", *IEEE Trans. Magn.*, Vol. 37(4), pp. 2353-2355, 2001.

[18]   Rado, G. T., Wright, R. W., Emerson, W. H. and Terris, A., "Ferromagnetism at Very High Frequencies. IV. Temperature Dependence of the Magnetic Spectrum of a Ferrite", *Phys. Rev.*, Vol. 88, pp. 909-915, 1952.

[19]   Chauhan, B. S., Kumar, R., Jadhav, K. M. and Singh, M., "Magnetic study of substituted Mg-Mn ferrites Synthesized by citrate precursor method", *J. Magn. Magn. Mater.,* Vol. 283, pp. 71-81, 2004.

[20]   Brockman, F. G., Dowling, P. H. and Steneck, W. G., "Dimensional Effects Resulting from a High Dielectric Constant Found in a Ferromagnetic Ferrite", *Phys. Rev.*, Vol. 77, pp. 85-89, 1950.

[21]   Radhakrishnamurty, C., Likhite, S. D., Deutsch, E. R. and Murthy, G. S., "On the complex magnetic behavior of titanomagnetites", *Phys. Earth Planet. Inter.*, Vol. 30, pp. 281-290, 1982.

[22]   Jadhav, S. R., Sawant, S. R., Suryavanshi, S. S. and Patil, S. A., "Temperature and frequency dependence of initial permeability in Zr^{4+} substituted Cu-Zn ferrites", *J. Less-Common Met.*, Vol. 158, pp. 199-205, 1990.

[23]   Abeledo, C. R. and Frankel, R. B., "Mössbauer study of spin alignment in substituted lithium ferrites", *J. Phys.*, Vol.38, pp. 135, 1977.

[24]   J. Smit, H. P. J. Wijin, *Ferrites*, Philips Technical Library, Eindhoven, Netherland, 1959.

CHAPTER 5

CONCLUSIONS

5.1 Conclusions

The present study focused on the microstructure, complex permeability, Néel temperature and DC magnetization of $Li_{0.35-0.5x}Ni_{0.3}Zn_xFe_{2.35-0.5x}O_4$. The significant findings of this study are as follows:

♣ Sol-gel auto combustion technique has been adopted to prepare various $Li_{0.35-0.5x}Ni_{0.3}Zn_xFe_{2.35-0.5x}O_4$ powders.

♣ The XRD analysis of various $Li_{0.35-0.5x}Ni_{0.3}Zn_xFe_{2.35-0.5x}O_4$ confirms that all the samples have single phase cubic spinel structure. No impurity peak is found in XRD pattern.

♣ The lattice constant slightly increases with the increasing of Zn content in $Li_{0.35-0.5x}Ni_{0.3}Zn_xFe_{2.35-0.5x}O_4$ obeying Vegard's law. This phenomenon is explained on the basis of ionic radii. In the present case variant contents are *Li*, *Zn* and *Fe*, while both in Li^{1+} (0.7Å) and Fe^{3+} (0.67Å) are substituted by Zn^{2+} (0.82Å). Since the ionic radius of Zn^{2+} is greater than that of the Li^{1+} and Fe^{3+} the increase in lattice constant with the increasing Zn substitution is expected.

♣ It is observed that the density of various $Li_{0.35-0.5x}Ni_{0.3}Zn_xFe_{2.35-0.5x}O_4$ increased with increasing sintering temperature up to 1250°C, then decreases. On the other hand, porosity (P) of the sample decreased with increasing sintering temperature up to 1250°C. This may be due to the fact that during the sintering process, the thermal energy generates a force that drives the grain boundaries to grow over pores, thereby decreasing the pore volume and increasing the density of the materials. It is also observed that the density of $Li_{0.35-0.5x}Ni_{0.3}Zn_xFe_{2.35-0.5x}O_4$

110

decrease beyond the sintering temperature 1250°C. On the other hand, porosity (*P*) of the samples increases beyond sintering temperature 1250°C due to the fact that at higher sintering temperatures density decreases, because the intragranular porosity increases as a result of discontinuous grain growth that leads to decrease the sintered density.

♣ Enlargement of grain size of all composition has been observed with the increase sintering temperature up to 1250°C, then decreases. The thermal energy generates a force that drives the grain boundaries to grow over pores and reinforces to increase the grain diameter. The average grain size increase with increase in Zn content. It is also known that Zn promotes grain growth, bringing about an increase in grain size.

♣ The real ($\mu_i^{/}$) and imaginary ($\mu_i^{//}$) permeability increase with *Zn* substitution. With the increase of sintering temperature the real part of initial permeability $\mu_i^{/}$ increases up to 1250°C and above 1250°C a decreasing trend is observed. In contrast resonance frequency found to decrease with *Zn* substitution. Larger grains tend to consist of a large number of domain walls. The initial permeability increases with grain size. As $\mu_i^{/}$ increases, corresponding resonance frequency, f_r decreases. For compositions x = 0.3 and x = 0.4, f_r value shifted to a lower value as sintering temperature increases from 1100 to 1300°C. No resonance frequency is observed for $Li_{0.35}Ni_{0.3}Fe_{2.35}O_4$. For compositions x = 0.00 resonance frequency, f_r are above the measured frequency range (120 MHz).

♣ The loss factor, *tanδ,* is observed to increase with the increase of sintering temperature. The increase in sintering temperature results in increased loss in the samples, thereby creating defects in the lattice, which gives rise to magnetic loss.

The Q_{max} increases with increasing Zn contents from x = 0.00 to x=0.40 in $Li_{0.35-0.5x}Ni_{0.3}Zn_xFe_{2.35-0.5x}O_4$, for the samples sintered at 1250°C. The highest value of Q-factor (12395.29) is observed for $Li_{0.15}Ni_{0.3}Zn_{0.4}Fe_{2.15}O_4$ sintered at 1250°C, similar to $\mu_i^{/}$. Above 1250°C, *Q-factor* is found to decrease because at higher sintering temperature, abnormal grain growth occurs which creates trapped pores inside the grain.

♣ The value of T_N is found linearly decrease from 665 to 390°C. The weakening of exchange interaction may be confirmed by increasing lattice parameter and decreasing Néel temperature as increase of Zn content.

♣ The M_s and magnetic moment are found to increase with increasing Zn content in the compositions. Increasing trend of M_s could be explained by decrease in M_A and increase in M_B and in this way, the net magnetization increase.

5.2 Future research plan

Some studies on different aspects are possible for fundamental interest and also for potential application of the studied materials.

❖ Mössbauer spectroscopy can be studied to provide correct information on iron content on both the crystallographic sites.

❖ Neutron diffraction analysis may be performed for these composition to determine the magnetic structure of the composition.

❖ Some ac and dc electrical properties may be studied.

❖ Estimation of anisotropy constants is desirable from squid magnetometry.

❖ For the domain wall motion and degree of ordering present in the samples, MFM study can be carried out.